# Detection and characterisation of pli-de-passages on the cortical surface : from morphology to connectivity

Tianqi Song

# ÉCOLE CENTRALE DE MARSEILLE

ED 184 – MATHÉMATIQUES ET INFORMATIQUE

INT-INSTITUT DE NEUROSCIENCES DE LA TIMONE

## THÈSE DE DOCTORAT

pour obtenir le grade

**DOCTEUR de l'ÉCOLE CENTRALE de MARSEILLE**

Discipline: Informatique

**Tianqi SONG**

# Détection et caractérisation des plis-de-passage sur la surface du cortex cérébral: de la morphologie à la connectivité

*Detection and characterisation of pli-de-passages on the cortical surface: from morphology to connectivity*

Soutenance le 03/12/2021 devant le jury composé de:

| | | |
|---|---|---|
| Gloria MENEGAZ | Professeur, Université de Vérone, Vérone | Rapporteuse |
| Meritxell BACH CUADRA | Maîtresse de conférences, Université de Lausanne, Lausanne | Rapporteuse |
| Jean-Francois MANGIN | Directeur de recherche, Centre Neurospin, CEA, Gif-sur-Yvette | Examinateur |
| Pascal BELIN | Professeur, INT, CNRS & Aix-Marseille Université, Marseille | Examinateur |
| Olivier COULON | Directeur de recherche, INT, CNRS, Marseille | Directeur de thèse |

# Résumé

La surface du cortex cérébral est très convoluée, avec un grand nombre de plis, les sillons corticaux. Ces plis sont extrêmement variables d'un individu à l'autre. Cette grande variabilité constitue un problème pour de nombreuses applications en neurosciences et en imagerie cérébrale. Un problème central est que les sillons cérébraux ne sont pas la bonne unité pour décrire les plis sur la surface corticale. En particulier, leur géométrie (forme) et leur topologie (branches, nombre de pièces) sont très variables. Les "Plis de passages" (PPs) peuvent expliquer une partie de cette variabilité. Le concept de PPs a été introduit pour la première fois par Gratiolet (1854) pour décrire les gyri transversaux qui interconnectent les deux côtés d'un sillon, sont fréquemment enfouis dans la profondeur de ces sillons, et sont parfois apparents sur la surface corticale. En tant que caractéristique intéressante du processus de plissement cortical, la connectivité structurelle sous-jacente des PP a également suscité beaucoup d'intérêt. Cependant, la difficulté d'identifier les PPs et le manque de méthodes systématiques pour les détecter automatiquement ont limité leur utilisation.

Cette thèse vise à détecter et à caractériser les PPs sur la surface corticale tant du point de vue de la morphologie que de la connectivité. Elle s'articule autour de deux axes de recherche principaux : 1. Définition d'un processus de détection des PPs basé sur l'apprentissage automatique et utilisant leurs caractéristiques géométriques (ou morphologiques). 2. Étudier les relations entre les PP et leur connectivité structurelle sous-jacente, et poursuivre le développement de modèles d'apprentissage automatique multimodaux.

Dans la première partie, nous présentons une méthode de détection automatique des PP sur le cortex en fonction des caractéristiques morphologiques locales proposées dans (Bodin et al., 2021), Pour enregistrer les caractéristiques morphologiques locales de chaque sommet de la surface corticale, nous avons utilisé la méthode de profilage de la surface corticale (Li et al., 2010). Ensuite, le problème de reconnaissance tridimensionnelle des PP est converti en un problème de classification d'image bidimensionnelle avec un déséquilibre de classe où plus de points dans le STS sont des non-PP que des PP. Pour résoudre ce cas, nous proposons un modèle "Ensemble SVM" (EnsSVM) avec une stratégie de rééquilibrage. Les résultats expérimentaux et les analyses statistiques quantitatives montrent l'efficacité et la robustesse de notre méthode. Dans la deuxième partie, nous étudions la connectivité structurelle, en particulier les fibres U à courte portée, qui sous-tend la localisation des PPs, et proposons une nouvelle approche pour étudier la densité des terminaisons des fibres U sur la surface corticale. Nous émettons l'hypothèse que les PPs sont situés dans des régions de haute densité de terminaisons de fibres U croisées. En effet, nos analyses statistiques

montrent une corrélation de robustesse entre les PPs et la densité de terminaisons des fibres U. De plus, nous discutons de l'impact de l'hétérogénéité de la connectivité dans le STS sur les résultats de l'apprentissage automatique. Enfin, nous investiguons l'utilisation de cartes de myéline comme un complément à la connectivité structurelle.
**Mots clés :** Cerveau, machine learning, plis de passages, IRM, connectivité structurelle

# Abstract

The surface of the cerebral cortex is very convoluted, with a large number of folds, the cortical sulci. Moreover, these folds are extremely variable from one individual to another. This great variability is a problem for many applications in neuroscience and brain imaging. One central problem is that cerebral sulci are not the good unit to describe folding over the cortical surface. In particular, their geometry (shape) and topology (branches, number of pieces) are very variable. "Plis de passages" (PPs) or "annectant gyri" can explain part of the variability. The concept of PPs was first introduced by Gratiolet (1854) to describe transverse gyri that interconnect both sides of a sulcus, are frequently buried in the depth of these sulci, and are sometimes apparent on the cortical surface. As an interesting feature of the cortical folding process, the underlying structural connectivity of PPs also generated a lot of interest. However, the difficulty of identifying PPs and the lack of systematic methods to automatically detecting them limited their use.

This thesis aims to detect and characterise the PPs on the cortical surface from both morphology and connectivity aspects. It was structured around two main research axes: 1. Definition of a machine learning-based PPs detection process using their geometrical (or morphological) characteristics. 2. Investigate the relationships between PPs and their underlying structural connectivity, and further development of multi-modal machine learning models.

In the first part, we present a method to detect the PPs on the cortex automatically according to the local morphological characteristics proposed in (Bodin et al., 2021), To record the local morphological patterns for each vertex on the cortical surface, we used the cortical surface profiling method (Li et al., 2010). After that, the three-dimensional PP recognition problem is converted to a two-dimensional image classification problem of class-imbalance where more points in the STS are non-PPs than PPs. To solve this case, we propose an ensemble SVM model (EnsSVM) with a rebalancing strategy. Experimental results and quantitative statistics analyses show the effectiveness and robustness of our method. In the second part, we study the structural connectivity, particularly short-range U-fibers, underlying the location of PPs, and propose a new approach to study the density of U-fiber terminations on the cortical surface. We hypothesize that the PPs are located in regions of high density of intercrossing U-fibers termination. Indeed, our statistical analyses show a robustness correlation between PPs and U-fibers termination density. Moreover, we discuss the impact of connectivity heterogeneity in the STS on the machine learning results, and the myelin map is then used as a supplement to the structural connectivity.


**Key words:** Brain, machine learning, annectant gyri, MRI, structural connectivity

# Contents

# Introduction

The surface of the cerebral cortex is very convoluted, with a large number of folds, the cortical sulci. Moreover, these folds are extremely variable from one individual to another. This large variability is a problem for many applications in neuroscience and brain imaging: because it is difficult to define an interval of normal variability; it is difficult to detect abnormal folding that could be associated to a pathology; also, the large inter-subject differences induced by this variability makes neuroscience group studies very difficult when it comes to compare hundreds of individuals; finally, it is difficult, and sometimes impossible, to use folds as landmarks in order to localize information (e.g. functional activity) on the cortical surface.

One central problem is the fact that cerebral sulci might not be the good unit to describe folding over the cortical surface. In particular, their geometry (shape) and topology (branches, number of pieces) are very variable. Nevertheless, some models state that they can be subdivided in sub-units that are more reproducible (Regis et al., 2005; Ochiai et al., 2004) across individuals. The difficulty to implement such models is to find how to subdivide folds properly. Some specific landmarks buried within the folds have been proposed for this subdivision and are called "annectant gyri" or "plis de passages" (PPs) (Ochiai et al., 2004; Cunningham, 1892). These landmarks have been successfully used to describe cortical folding and its variability (Ochiai et al., 2004; Zlatkina and Petrides, 2010). Annectant gyri are difficult to detect and the geometry of the cortical surface alone is not enough to properly locate them. Nevertheless, we know that they can be characterized by a multi-modal set of features, such as the local geometry (Bodin et al., 2021; Song et al., 2021), cortical depth variations (Cykowski et al., 2008; Le Guen et al., 2018), or the structure of the fiber bundles in the underlying white matter(Bodin et al., 2021).

This main objective has been the guiding thread of this thesis, which has been organized around two research lines:

The first one is the definition of a machine learning-based PPs detection process using their geometrical (or morphological) characteristics. The aim is to detect all PPs in the superior temporal sulcus using triangular mesh models of the cortical surface. The second line of research is to investigate the relationships between PPs and their underlying structural connectivity, and further development of multi-modal machine learning models using morphology, connectivity, myelin content, etc.

The writing of this manuscript has been done as follows:

The first chapter will introduce the essential neuroanatomical concepts for better understanding the brain anatomical principles. Then, we describe the main anatomical issue

of our interest, namely the variability of cortical foldings, and some regions of interest or folding patterns proposed in the literature to explain this. After that, we introduced the definition of the brain white matter connectivity, particularly the U-fibers, and a general introduction of the data used in our work.

In the second chapter, we focus on the PPs from a morphological methodology perspective. We will describe in detail the concept of PPs and then discuss the morphological clues used for identifying the PPs, from the observer-dependent definition of "sulcal roots"(Regis et al., 2005), to the variation of sulcal depth profile (Cykowski et al., 2008; Leroy et al., 2015; Le Guen et al., 2018), and finally to the presence of features called "wall pinches" (WPs)(Bodin et al., 2021).

The third chapter will present our method to automatically detect the PPs in the superior temporal sulcus (STS) by using the morphological features "WPs" in (Bodin et al., 2021). For this purpose, we will introduce the cortical surface profiling method (Li et al., 2010), which has been used to generate new feature maps and record the local geometrical information. After that, the three-dimensional PP recognition problem is converted to a two-dimensional image classification problem with class-imbalance where more points in the STS are non-PPs than PPs. To solve this case, we propose an ensemble SVM model (EnsSVM) with a rebalancing strategy. Experimental results and statistical analyses of our method will be discussed.

Finally, the fourth chapter will be dedicated to the PPs and their underlying connectivity of short-range U-fibers. We will first introduce the pipeline of U-fibers extraction (Bodin et al., 2021; Pron et al., 2021). To further investigate the location of PPs and U-fibers, we propose a new density map of U-fibers terminations on the cortical surface. Several experiments and quantitative statistical analyses will be discussed to reveal that the PPs are located in the regions where intercrossing U-fibers terminate. After that, we will study the results of the EnsSVM trained on connectivity maps and connectivity heterogeneity in the STS. Finally, we investigate the use of myelin map as as a marker of connectivity. In order to put in relation the literature and the new results brought by my work, I will conclude this manuscript by a general discussion.

# 1 Context

## 1.1 The human brain

The human brain is the central organ of the human nervous system and it is an immensely complex structure. Even so, there are ways we can divide up its anatomical structure into more discrete parts, e.g. the left and right hemisphere, or the parietal, temporal, occipital, and frontal lobes in each hemisphere. Another common divider is to separate the brain's gray and white matter. In this section, we present some essential concepts of brain anatomy, its variability, as well as the modality we use, i.e. Magnetic Resonance Imaging.

### 1.1.1 Brain anatomy

#### Gyri and Sulci

The telencephalon or brain, the main organ of the central nervous system, is responsible in humans for integration, processing of sensory information, motor control, and cognition. Located in the cranium and bathed in cerebrospinal fluid, the brain is composed of two similar hemispheres, incompletely separated by the longitudinal fissure. In neuroanatomy, a *sulcus* (pl. sulci) is a depression or groove in the cerebral cortex. It surrounds a *gyrus* (pl. gyri), creating the characteristic folded appearance of the brain in humans and other mammals. The larger sulci are usually called fissures. The human brain has a wrinkled, walnut-like external appearance resulting from the complex spatial arrangement of convolutions (gyri) bounded by sulci (Ono et al., 1990). These gyri and sulci form important landmarks that allow us to separate the brain into functional centers.

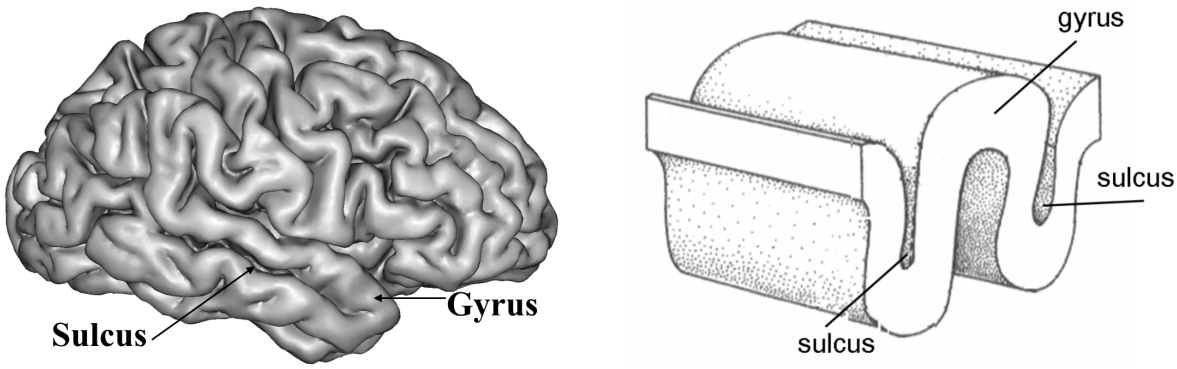


Figure 1: Sulcus and gyrus

The principal sulci and gyri, and the resulting division into lobes (frontal lobe, parietal lobe, temporal lobe, occipital lobe, limbic lobe and insula) are shown in Figure 2.

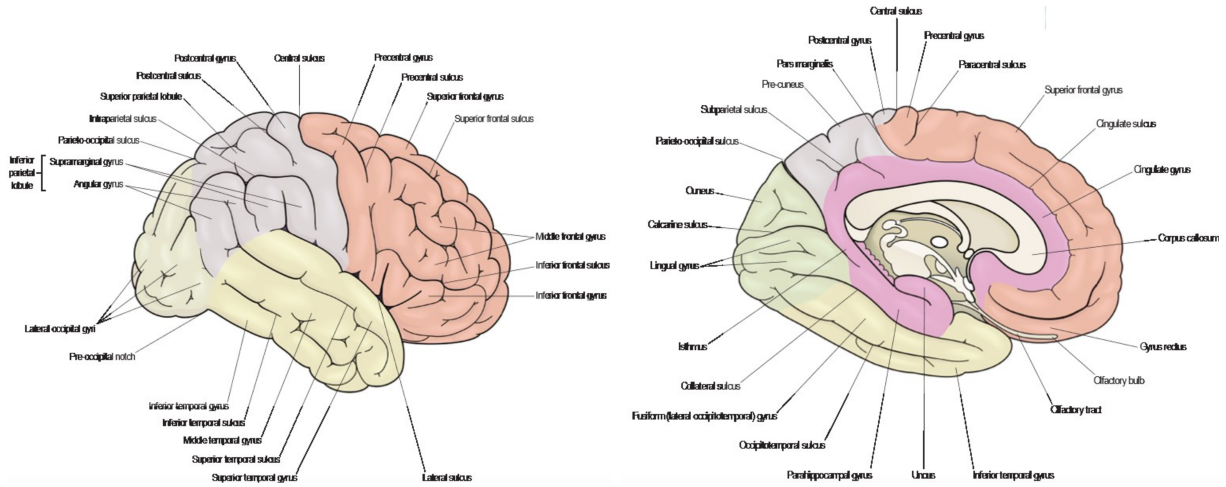


Figure 2: Principal sulci and gyri of the human brain and division into lobes: frontal lobe (red), parietal lobe (grey), temporal lobe (yellow), occipital lobe (green), limbic lobe (pink). Lateral (left) and medial (right) views. Figures adapted from (Jones et al., 2013).

### White matter and Grey matter

The average volume of the adult human brain is about 1170 $cm^3$ (Ritchie et al., 2018), which can vary according to gender (Ritchie et al., 2018) and age (Cox et al., 2016). On a macroscopic scale, the telencephalon appears to be essentially composed of two tissues, named after their visual appearance, *grey matter* and *white matter*. A distinction is made between the cortical grey matter, located in the cerebral cortex, a peripheral layer 1 to $4.5mm$ thick (e.g. (Fischl and Dale, 2000)), and the subcortical grey matter, which is more central and composed of the symmetrical paired structures of the *hippocampus*, *amygdala*, *caudate nucleus*, *putamen*, and *pallidum*. The white matter occupies the space between the cerebral cortex, the subcortical structures and the cerebrospinal fluid of the ventricles (see Figure 3).

### 1.1.2 Cellular components

The human brain is composed of neurons and neuroglial cells. Neurons are considered the structural and functional units of the nervous system. A neuron consists of a cell body and two types of cytoplasmic extensions, the dendrites and the axon, whose role is to integrate and transmit, respectively, the bioelectric potentials known as action potentials. The axon, when present, starts from the cell body at the level of the emergence cone and describes a tortuous trajectory of variable length (from a few micrometers to more than a meter) before branching (terminal arborization). Approximately one-third of the axons in the brain are surrounded by myelin sheaths, a lipidic insulating substance that increases the speed of


Figure 3: White and Grey matter (cerebral cortex and subcortical structures) of the human brain in coronal section. Left: dissection; right: annotated diagram. Figures adapted from (Mai et al., 2015).

propagation of action potentials. The diameter of the cell body of a neuron varies from 5 to 120$\mu m$, while that of the axon is in the order of 0.3 to 10$\mu m$, depending on whether it is myelinated or not. Neuroglial cells are not directly involved in the transmission of action potentials. Neuroglia is divided into macroglia, composed of astrocytes, oligodendrocytes, and microglia, a collection of star cells smaller than the macroglia cells. Glial cells are smaller in size than neurons. The number of neurons in the central nervous system, estimated at one hundred billion, represents about 10% of the number of cells in the central nervous system, the remaining cells being glial cells.

The grey matter is mainly composed of the cell bodies and dendrites of neurons as well as glial cells, notably oligodendrocytes. The white matter contains axons, both myelinated and unmyelinated, as well as neuroglial cells. The white matter owes its color to the myelin sheaths of the axons, an unmyelinated axon being transparent. The white matter is therefore mainly responsible for transporting bioelectrical information, while the grey matter is mainly responsible for integrating and processing this information. The connectivity within the cerebral cortex is called intrinsic connectivity, that via the white matter, extrinsic connectivity.

## 1.2 Cortical folding and variability

Cortical folding, an essential characteristic of the brain cerebral cortex, shows variability across individuals. This variability is very disturbing when trying to project an atlas of the sulci onto a specific brain (Mangin et al., 2015). As an instance of folding pattern variability, Figure 5 shows twelve individual manually labeled sulci. The morphology of folding is the

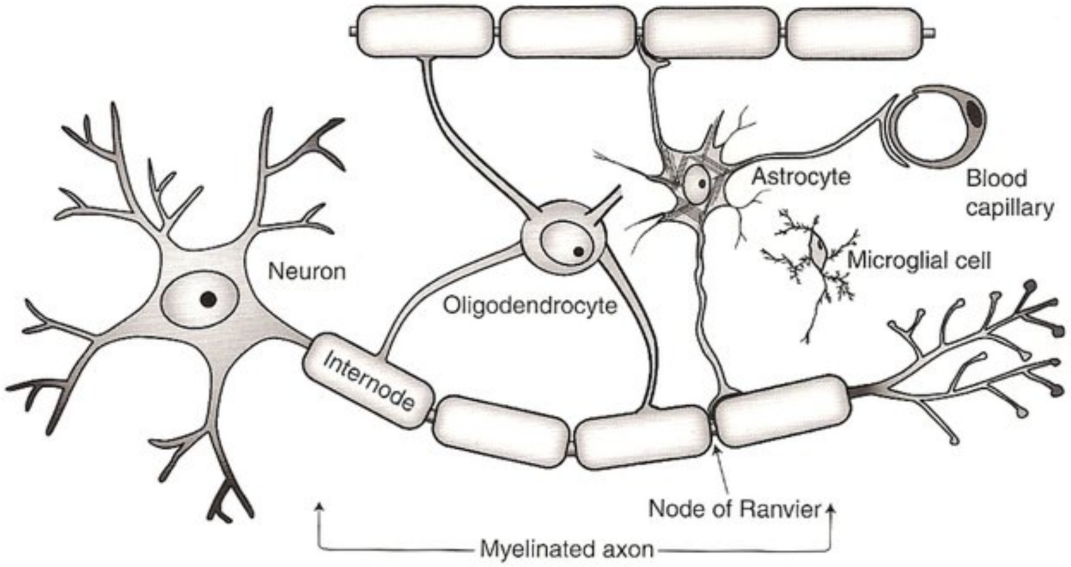


Figure 4: Cellular components of white matter. Image adapted from (Johansen-Berg and Behrens, 2013).

most basic and direct way to describe the geometric information of various folding patterns. In the last decades, the descriptors of cortical folding have been widely studied (Ono et al., 1990; Ochiai et al., 2004; Mangin et al., 2015, 2019). Quantitative descriptions of folding patterns(Zilles et al., 1988; Yu et al., 2007; Toro et al., 2008; Li et al., 2010; Le Guen et al., 2018) and understanding of the underlying mechanisms(Van Essen, 1997; Toro and Burnod, 2005; Geng et al., 2009; Auzias et al., 2015; Chen et al., 2017) progressively become important research topics.

### 1.2.1 Inter-individual variability

There are clear similarities when looking at the cortical anatomy of several individuals. The spatial arrangement of sulci and gyri as well as their temporal development show common patterns (Borrell and Reillo, 2012; Welker, 1990). However, these similarities mainly concern the primary folds, and there is considerable variability left unexplained in the cortical anatomy between individuals (see Figure 5). As this variability is a hindrance to the identification of anatomical-functional relationships, several models have emerged to try to explain it and to extract consistent patterns of folding across individuals.

According to the "radial unit" hypothesis, cortical expansion during evolution would be the result of changes in cell proliferation during development, increasing the number of radial unit columns in the forming cortex (Rakic, 1988, 1995). These radial units would also constitute a "protomap" where the future cytoarchitectonic organization of the cortex would be recorded. Far from explaining the complete organization of the cortex, this hypothesis

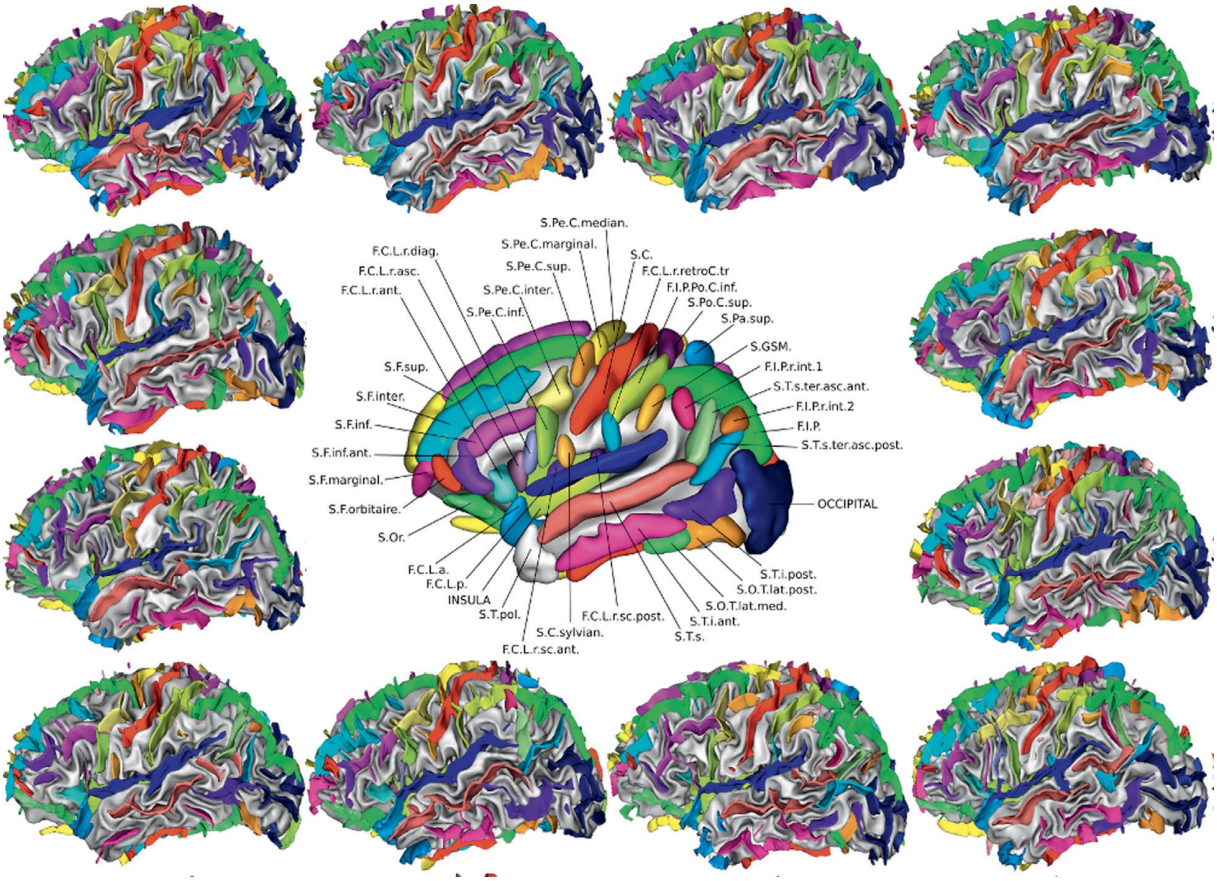


Figure 5: Twelve left lateral cortical surfaces with elementary folds manually labeled according to the sulcus atlas of BrainVISA (http://brainvisa.info). Figure adapted from (Perrot et al., 2011).

suggested above all a common base on which individual variability would be affixed. This idea has given rise to more recent models of cortical variability. For example, the sulcal root model introduced by Regis et al. (2005) advocated a common pattern of sulcus and gyri organization across individuals. As on a geographical map, sulcal roots can be arranged on a flat representation of the cortical surface according to a system of meridians and parallels. Each sulcal root is bordered by two parallel gyri and two gyri orthogonal to it. This organization is visible from the fetal stage but changes with cortical expansion until adulthood. The orthogonal gyri often lay deeper than those parallel to the sulcus. An example is the superior temporal sulcus (STS) framed by the parallel superior and middle temporal gyri and sometimes interrupted orthogonally by annectant gyri, or "plis-de-passage" (Ochiai et al., 2004) (see Figure 6). More recently, the sulcal root model has made it possible to establish a coordinate system that allows better localization of sulci and inter-subject comparison (Clouchoux et al., 2010; Auzias et al., 2013).

The depth of cortical surface appears to be an important feature in characterizing indi-

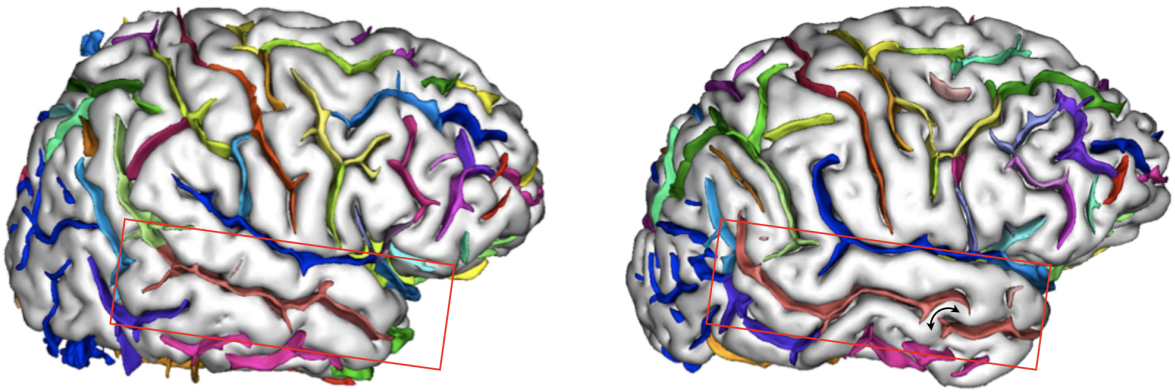

Figure 6: Example of interrupted STS. The black double-headed arrow shows the "plis-de-passage".

vidual variability. In parallel with investigations of superficial landmarks such as "plis-de-passage", others have focused on the deeper points of the cortex. The sulcal basins have thus been described by (Lohmann et al., 1999) as the deep parts of the sulci and can be linked to sulcal roots. In line with this work, algorithms have been developed to extract the deepest points located at the bottom of sulcal basins (Im et al., 2010; Meng et al., 2014; Auzias et al., 2015). Known as "sulcal pits", these points are more stable across individuals compared to more superficial points (Lohmann et al., 2008). Their location has been shown to be robust across MRI sessions, different scans and surface extraction methods (Im et al., 2013). Furthermore, these regions appear to be governed by important genetic constraints as their configuration has been shown to be more consistent in monozygotic twins than in unrelated individuals (Im et al., 2010), with deeper sulci being more similar than shallow sulci (Lohmann et al., 1999). The regions of interest in cortical surface discussed above (plis-de-passage, sulcal pits, sulcal roots) are shown in Figure 7 using the STS as an example. More details about these cortical folding pattern will be discussed in chapter 2.

## 1.3 Brain Connectivity

Brain connectivity refers to a pattern of anatomical links ("anatomical connectivity"), of statistical dependencies ("functional connectivity") or of causal interactions ("effective connectivity") between distinct units within a nervous system (Sporns, 2007). The units correspond to individual neurons, populations of neurons, or anatomically separated brain regions. The pattern of connectivity is formed by structural links such as synapses or fibre pathways, or it represents a statistical or causal relationship, measured in terms of cross-relationships, coherence or information flow. Neural activity, and by extension neural codes, are constrained by connectivity. Brain connectivity is thus crucial to elucidating

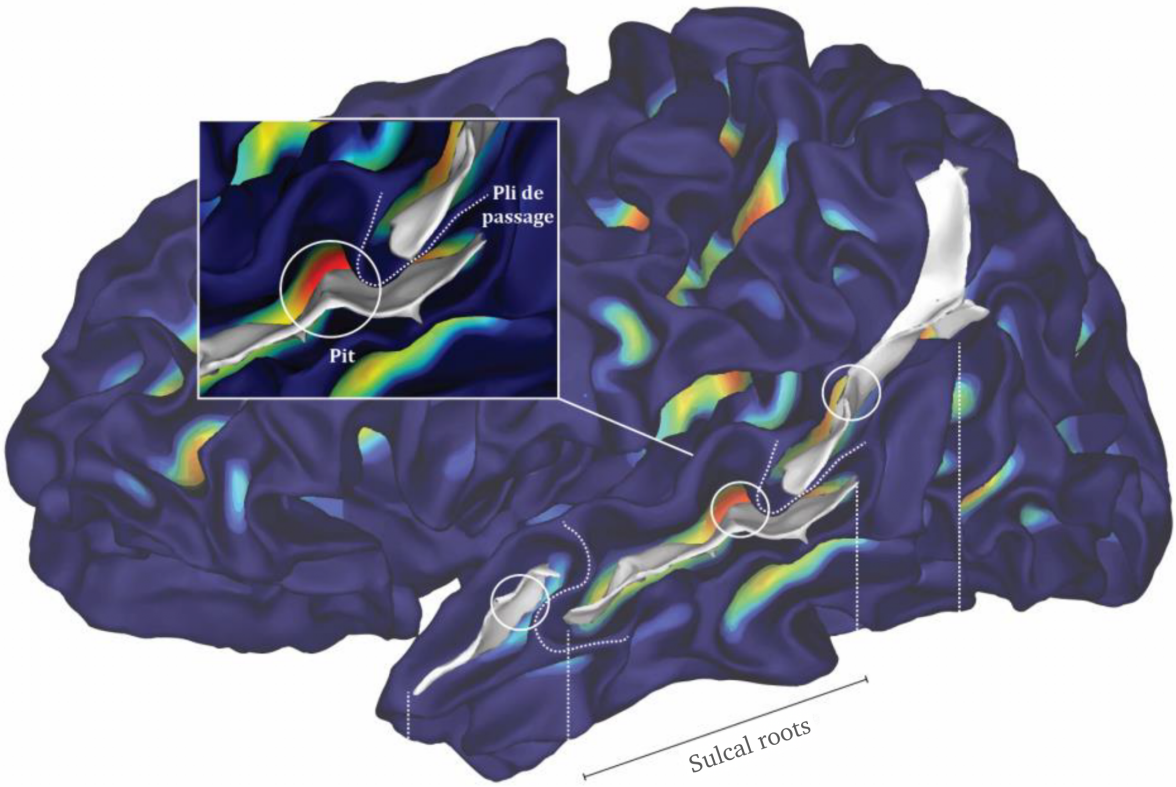


Figure 7: Regions of interest in the cortical surface illustrated on the Superior Temporal Sulcus (STS, shown in 3D in white) of a subject. The sulcal pits (in circles) are the deepest points of the sulcal roots (different parts of the STS delimited by the dotted lines), themselves delimited by the passage folds (dotted lines). The surface represents the grey/white material interface reconstructed with BrainVisa software, on which the depth map has been projected (in red the deepest regions).

how neurons and neural networks process information. The structural connectivity, which can be defined as the existence of white matter tracts physically interconnecting brain regions (Sporns et al., 2005; Uddin, 2013), arouses great interest in but not limited to the neurodevelopmental process (Dubois et al., 2014), functional organization (Saygin et al., 2012; Wendelken et al., 2017) and brain diseases (Griffa et al., 2013). The remainder of this work will focus on the anatomical connectivity or structural connectivity, in particular the short-range U-fibers, because, as it will be discussed after, they have a specific link with cortical morphology.

### 1.3.1 Definition: short association fibers and U-shaped fibers

The distinction between short and long association bundles was originally proposed by Meynert (1885):

*'The cortex exhibits on the convexity of each convolution the shape of an inverted U,*

*which is changed in the next adjoining fissure to an upright U (top and bottom of the cortical wave). The depressed surface of a cortical wave can be easily dissected out as from a smooth medullary groove, which on closer inspection is seen to consist of U-shaped medullary fibers. The U-shaped bundles of the cortex do not necessarily extend simply from one convolution to the one next adjoining, but they may skip one, two, three, or an entire series of convolutions. The shortest fibrae propriae lie nearest to the cortex.'*

Meynert adopted a macroscopic definition of short association bundles based on the U-shaped geometry of these fibers, in relation to the folding of the cerebral cortex, rather than on a criterion of proximity of connected cortical territories. Meynert also reported a link between cortical proximity and length for U-shaped fibers but does not make explicit the distribution and terminations of these fibers (e.g. symmetry of these fibers with respect to the bottom of the sulcus, terminations on the walls or near the crests of the gyri). In addition, the distinction between some long, arcuate association bundles, e.g. bundle 4 (blue, bottom of Figure 8) and short association bundles (red, top of Figure 8) appears ambiguous. In this sagittal cross-sectional representation, it is also noticeable that the U-shaped fibers are shown connecting the outer walls of adjacent convolutions, as the two walls of the same groove are not connected.

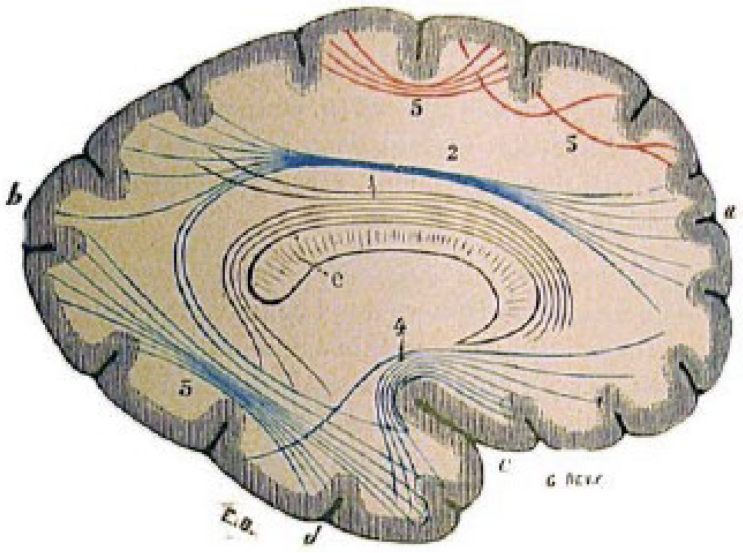


Figure 8: Distinction of association fibers proposed by Meynert into short association fibers (red) and long association fibers (blue). Figure adapted from (Jones and Cercignani, 2010).

Meynert's original definition was taken up and refined by Dejerine (Dejerine et al., 1895):

*'Les courtes fibers d'association relient deux circonvolutions ou deux lobes voisins [...] elles forment quelquefois, presque à elles seules, la masse blanche de certaines circonvolutions [...] et en général de tous ces plis plus ou moins complexes, irréguliers et variables*

*d'un individu à l'autre, d'un hémisphère à l'autre, qui compliquent l'étude des circonvolutions du manteau cérébral. Les fibers les plus courtes et les plus superficielles de ces plis tapissent le fond des sillons, les plus longues naissent du sommet du pli anastomotique pour se rendre à une circonvolution plus éloignée.[...] La direction des fibers en U est toujours perpendiculaire au grand axe du sillon qu'elles tapissent.'*

Dejerine reported a main trajectory of U-shaped fibers approximately orthogonal to the main axis of the sulcus, implying that these fibers connect cortical territories that are quasi-symmetrical with respect to this same axis. Dejerine refined the relationship between length and depth noted by Meynert, with the longest fibers explicitly associated with the peaks of the gyri while the shortest fibers are concentrated in the bottom of the sulci. This affirmed the predominant role of the sulcus and suggested a laminar organisation of the U-shaped fibers, intrinsically linked to the geometry of the cortex. This observation would preclude having U-shaped fibers connecting two cortical territories located on the same wall of a sulcus. However, it also raised the question of an objective criterion for distinguishing between short and long association fibers. Schmahmann et al. (2009) proposed a more restrictive definition of U-shaped fibers in their monograph on the study of anatomical connectivity in the macaque:

*'Local association fibers, or U-fibers, leave a given area of cortex and travel to an adjacent gyrus, running in a thin, identifiable band immediately beneath the sixth layer. Neighborhood association fibers arise from a given cortical area and are directed to nearby regions but are distinguishable from the local U-fibers that run immediately beneath the cortex.'*

As summarised in Figure 9, and visible at the microstructural level in Figure 10, the U-shaped fibers of the rhesus macaque are located immediately below the cerebral cortex, in a band estimated to be 0.5mm thick according to the scale of the sample in Figure 10. This proximity to the cortex, rather than the length of these fibers, would allow them to be distinguished from so-called neighbourhood association fibers, although as noted by Dejerine and Meynert length and depth are related. Thus Meynert and Dejerine's definition of U-shaped fibers potentially includes long and neighbouring fibers in the sense of Schmahmann et al. (2009). Furthermore, the representation in Figure 9 suggests that these fibers connect the two walls of a groove but does not specify the maximum spatial extension of these fibers.

Schüz and Braitenberg (2002) defined a U-shaped fiber as a short fiber of less than $30mm$ in length that connects two nearby cortical territories and remains in a band of superficial white matter located at a distance of $1.5mm$ from the cortex. And they estimated approximately the U-shaped fibers would represent more than ninety percent of the association fibers of the percent of the association fibers in the human brain.

The lack of consensus on an objective definition of a short association fiber in humans

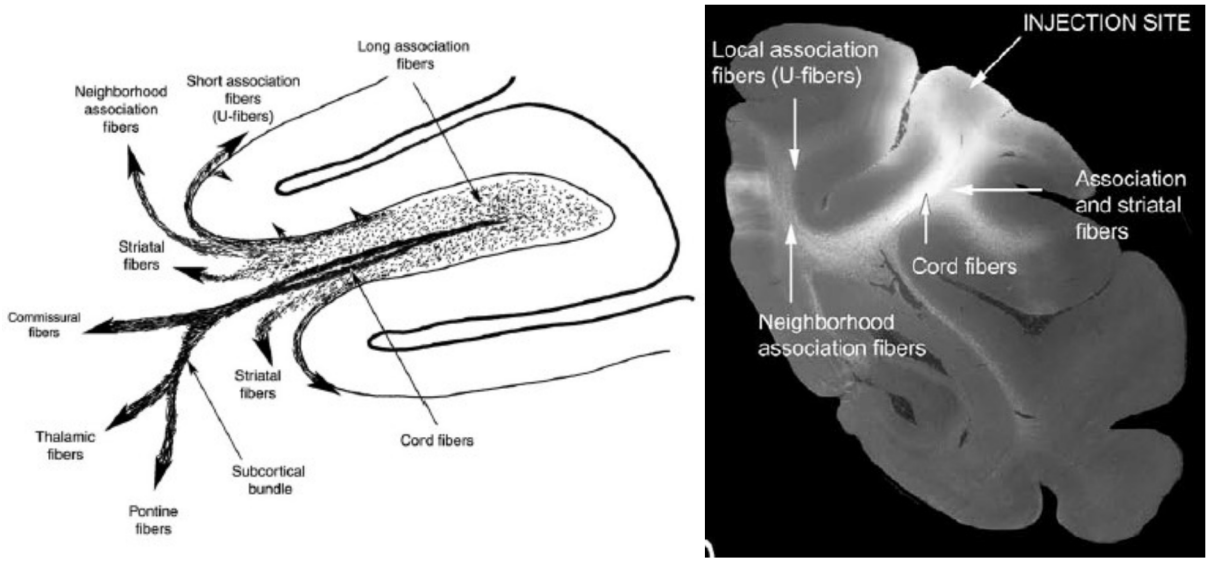


Figure 9: LEFT: Classification and simplified representation of fiber bundles in the macaque suggesting that U-shaped fibers connect the two walls on either side of a sulcus with a high-angle turn at the entrance (exit) of the cortex. RIGHT: Dark-field photomicrograph of a coronal section of the rhesus macaque brain after injection of a radioactive isotope into the caudate region of the inferior parietal lobule. Figures adapted from (Schmahmann et al., 2009).

is probably indicative of the high variability of these fibers (Dejerine et al., 1895), but also of the limitations of the different techniques used to study them, such as post-mortem dissection.

### 1.3.2 U-shaped fibers in human brain

Since their first description by Meynert (1885) at the end of the 20th century, few studies have been devoted to the short association fibers of the human white matter (Catani et al., 2012). A detailed atlas of the main association fibers of the occipital lobe was compiled by Heinrich Sachs on the basis of dissections (Sachs, 1893; Forkel et al., 2015). A longitudinal U-shaped fiber system connecting the frontal lobe gyri and short association bundles connecting the precentral and postcentral gyrus were described by Christfried Jakob (Jakob, 1906; Theodoridou and Triarhou, 2012). Joshua Rosett established an atlas of most of the short association fibers of the human brain in 1933 (Rosett, 1933), but using a dissection technique that did not allow the isolation of the entire trajectory of these fibers and their terminations. Following the development of diffusion-weighted MRI (Le Bihan and Breton, 1985), several preliminary estimates of U-shaped fiber trajectories have been made (e.g. (Conturo et al., 1999; Catani et al., 2002; Oishi et al., 2008). A mapping of short association fibers in the frontal and parietal lobes has been proposed (Catani et al., 2012; Catani,

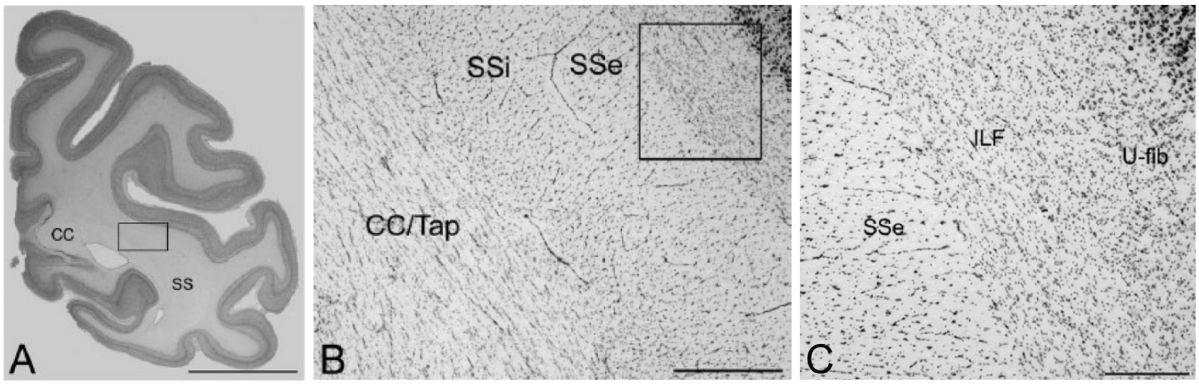


Figure 10: Light field photomicrographs prepared with Nissl stain. (A) is a coronal section of the parietal lobe (Magnification = $0.5\times$, bar = $0.5cm$); (B) is a high power photomicrograph of the rectangular area outlined in (A) (Magnification = $2\times$, scale = $1mm$); (C) is a higher power magnification of the area outlined in (B) showing the differential arrangement of glia in the inferior longitudinal fascicle (ILF) and U-fibers (U-fib) (Magnification = $4\times$, scale = $0.5mm$). The latter scale is to be related to the spatial resolution of diffusion MRI e.g. $1.25mm$ for the Human Connectome Project (HCP) and the integration step used in tractography (the order of $0.125mm$). Figure adapted from (Schmahmann et al., 2009).

2017). These bundles, reconstructed from diffusion-weighted magnetic resonance imaging (dMRI) data were confirmed by Klingler postmortem dissection. Other U-fiber delineations and association bundle atlases containing U-fibers have been constructed from dMRI data, including (Guevara et al., 2017; Román et al., 2017; Yeh et al., 2018; Avila et al., 2019), however the existence of the fibers in these atlases has not been extensively confirmed by dissection.

**U-shaped fibers and neurodevelopment**

Diffusion MRI has been used to assess the evolution of U-shaped fibers during development (Lebel et al., 2019) and particularly during gestation (Dubois et al., 2014). The presence of short association fibers along the anteroposterior axis in the dorsal regions of the brain as well as in the inferior frontal lobe was demonstrated during the 24th gestational week, prior to cortical folding (Takahashi et al., 2012). At 31 weeks, U-shaped fibers were observed in the bottom of the first furrows formed, such as the central and parieto-occipital furrows, and these U-shaped fibers continue to be established until 40 weeks of gestation. Myelination of these fibers is later and can extend up to two years of age for fibers in the anterior part of the frontal lobe and up to forty years of age for those with the longest myelination time (e.g. (Dubois et al., 2014; Lebel et al., 2019)). Changes in the diffusion properties of the superficial white matter structure (and thus possibly of the U-fibers) or directly of the U-fiber structure have been reported in neurodevelopmental disorders such as autism spectrum disorder (e.g. (Thompson et al., 2017; Hau et al., 2019)).

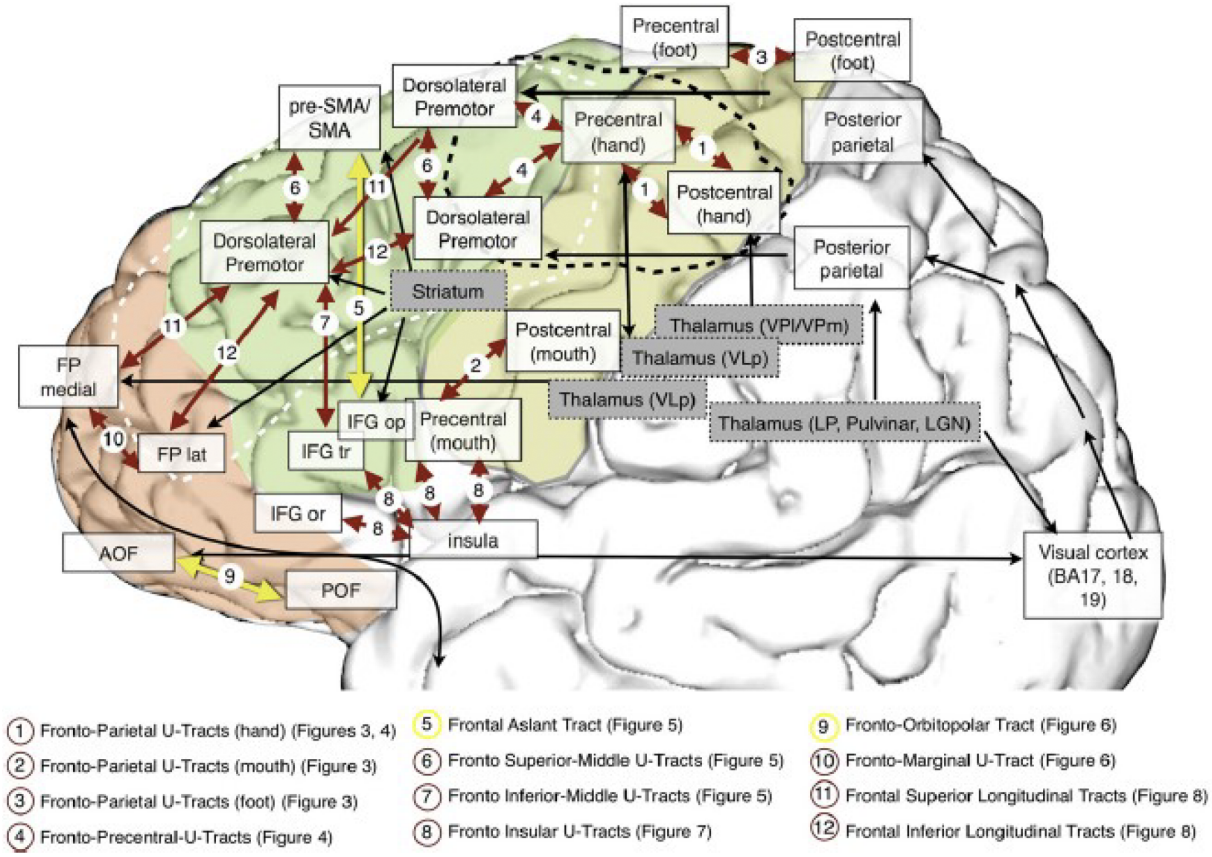


Figure 11: Mapping of short association fibers (red) in the frontal lobe obtained by tractography tractography and confirmed by Klingler dissection. Figure adapted from (Catani et al., 2012).

**U-shaped fibers and white matter pathologies**

Pathologies affecting white matter can be divided into three categories: pathologies affecting fiber myelin structure, those affecting myelin metabolism and vascular pathologies (Riley et al., 2018). Due to their late myelination, U-shaped fibers are generally unaffected by pathologies affecting fiber myelin metabolism. Riley et al. (2018) have shown that the structure of these fibers is an indicator for differential diagnosis of white matter pathologies. O'Halloran et al. (2017) reported in non-lesional epilepsy a decrease in the number of streamlines of U-shaped bundles located in the ipsilateral hemisphere at the origin of the crisis.

## 1.4 Magnetic resonance imaging

The phenomenon of nuclear magnetic resonance (NMR) was first observed in 1945 (Bloch, 1946; Purcell et al., 1946). It was the injection of radio frequency engineering expertise and the availability of stable new frequency sources, both byproducts of the wartime development

of radar, which may have made the demonstration of NMR possible. In 1973, Mansfield and Grannell (1973); Lauterbur (1973) first reported the MR imaging (MRI), and by the end of that decade, the first human in vivo MR images were produced. MR images of the head provided excellent anatomical detail and strong grey/white matter contrast when compared to the images from other modalities. Flow-sensitive techniques, developed in the mid-1980s, measured blood flow velocity: these were the first MR images that were not considered to be purely structural in nature (Moran, 1982). The spectacular advent of functional MR imaging (fMRI) two decades ago revolutionised MRI to such an extent that in current MRI practice (Matthews and Jezzard, 2004), the definition of structural MRI seems to have shifted to mean "not functional" MRI (Symms et al., 2004). In our work, we will focus on structural MRI, although there is controversy over whether diffusion MRI is structural MRI (Symms et al., 2004).

MRI uses magnetic fields and radio waves to produce high quality two- or three-dimensional images of brain structures without the use of ionizing radiation (X-rays) or radioactive tracers. MRI is one of the most commonly used tests in neurology and neurosurgery. For example, the contrast provided between grey and white matter makes MRI the best choice for many conditions of the central nervous system, including demyelinating diseases, dementia, cerebrovascular disease, Alzheimer's disease and epilepsy (Love, 2006; Mosconi et al., 2007; Sadek, 2012). MRI provides exquisite detail of brain, spinal cord and vascular anatomy, and has the advantage of being able to visualize anatomy in all three planes: axial, sagittal and coronal (see Figure 12). By using different software or algorithms for different MRI images, we can obtain various brain anatomical structures, such as the cortical surface, fibres, myelin maps, etc.

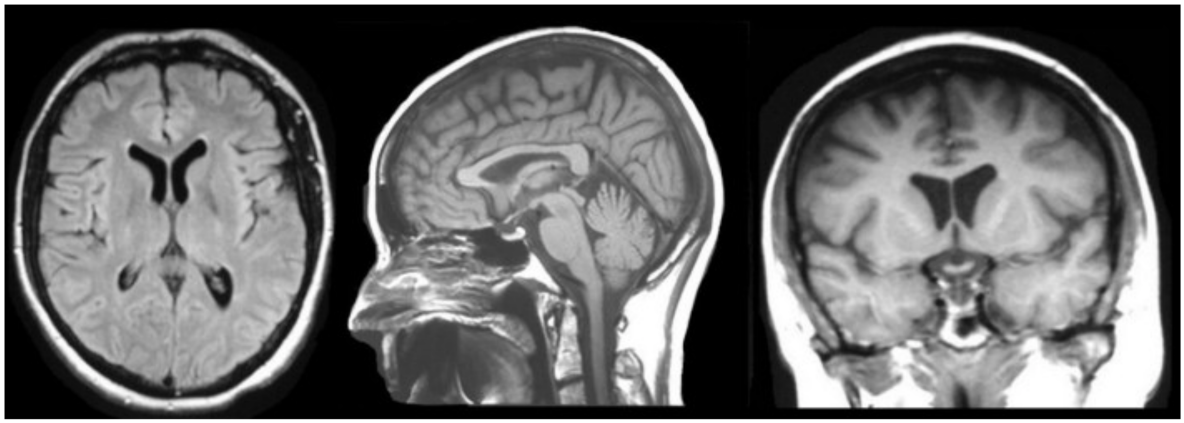

Figure 12: Example of brain MRI images. Three plane from left to right: axial, sagittal and coronal.

### 1.4.1 Construction and physics

MRI is based on the magnetization properties of atomic nuclei (Vlaardingerbroek and Boer, 2013). A powerful, uniform, external magnetic field is employed to align the protons that are normally randomly oriented within the water nuclei of the tissue being examined. This alignment (or magnetization) is next perturbed or disrupted by introduction of an external Radio Frequency (RF) energy, which is measured by a receiving coil. The nuclei return to their resting alignment through various relaxation processes and in so doing emit RF energy. After a certain period following the initial RF, the emitted signals are measured. Fourier transformation is used to convert the frequency information contained in the signal from each location in the imaged plane to corresponding intensity levels, which are then displayed as shades of gray in a matrix arrangement of pixels. By varying the sequence of RF pulses applied and collected, different types of images are created. *Repetition Time (TR)* is the amount of time between successive pulse sequences applied to the same slice. *Time to Echo (TE)* is the time between the delivery of the RF pulse and the receipt of the echo signal.

Tissue can be characterized by two different relaxation times – T1 and T2. T1 (longitudinal relaxation time) is the time constant which determines the rate at which excited protons return to equilibrium. It is a measure of the time taken for spinning protons to realign with the external magnetic field. T2 (transverse relaxation time) is the time constant which determines the rate at which excited protons reach equilibrium or go out of phase with each other. It is a measure of the time taken for spinning protons to lose phase coherence among the nuclei spinning perpendicular to the main field.

### 1.4.2 MRI imaging sequences

#### T1 and T2 images

The most common MRI sequences are T1-weighted and T2-weighted scans (see Figure 13). To create a T1-weighted image, magnetization is allowed to recover before measuring the MR signal by changing the TR. This image weighting is useful for assessing the cerebral cortex, identifying fatty tissue, characterizing focal liver lesions, and in general, obtaining morphological information, as well as for post-contrast imaging. To create a T2-weighted image, magnetization is allowed to decay before measuring the MR signal by changing the TE. This image weighting is useful for detecting edema and inflammation, revealing white matter lesions, and assessing zonal anatomy in the prostate and uterus.

In our work, the T1-weighted images are imported into the BrainVisa (BV) software (`http://brainvisa.info`) (Mangin et al., 2004a) to generate individual triangular mesh representations of the grey/white matter interface.

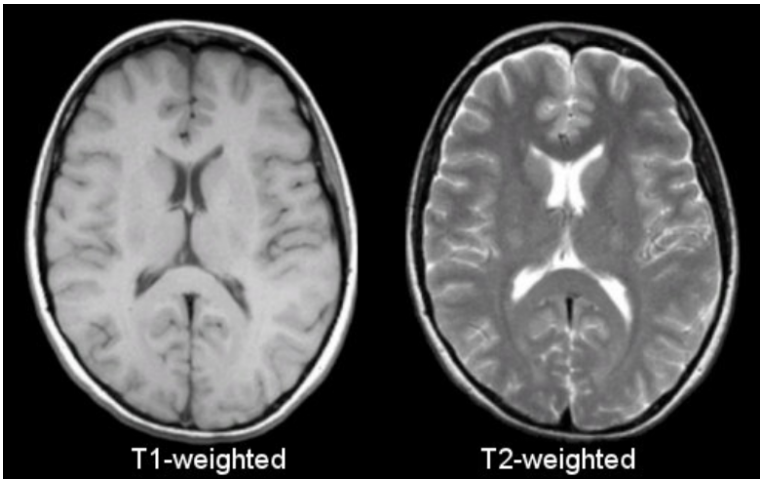


Figure 13: Examples of T1-weighted, T2-weighted images

### Diffusion-weighted MRI

The development of diffusion-weighted magnetic resonance imaging (dMRI) (Le Bihan and Breton, 1985), a non-invasive imaging modality, has led to a new boom in the exploration of the white matter structure of the human brain (Assaf et al., 2019). dMRI is the use of specific MRI sequences as well as software that generates images from the resulting data that uses the diffusion of water molecules to generate contrast in MR images (Le Bihan and Breton, 1985; Merboldt et al., 1985; Taylor and Bushell, 1985). It allows the mapping of the diffusion process of molecules, mainly water, in biological tissues, in vivo and non-invasively (Posse et al., 1993). Direct microscopic and macroscopic models of diffusion in complex media have been proposed including partial reflection Brownian motion (Grebenkov, 2006). Molecular diffusion in tissues is not random, but reflects interactions with many obstacles, such as macromolecules, fibers, and membranes. Water molecule diffusion patterns can therefore reveal microscopic details about tissue architecture, either normal or in a diseased state. The trajectories of water molecules diffusing in human brain white matter indirectly reflect the structure of the white matter and its constituents, e.g., diameter of cell bodies, axons, arrangement of oligodendrocytes (see (Novikov et al., 2019)). In particular, dMRI has led to a deeper understanding of the main white matter bundles and opened the way to characterise their inter-individual (e.g. (De Schotten et al., 2011)) and temporal (e.g. (Steele and Zatorre, 2018; Lebel et al., 2019)) variability. This imaging modality also plays a prominent role in the understanding of pathologies affecting the white matter such as cardiac arrest (e.g. (Velly et al., 2018)) or the so-called disconnection syndromes (Assaf et al., 2019).

In our work, we use dMRI images for tractography, a technique to extract fibers of

interest. Tractography is a 3D modeling technique used to represent nerve tracts using data collected by dMRI (Basser et al., 2000). Results are presented in two- and three-dimensional images called tractograms (see Figure 14).

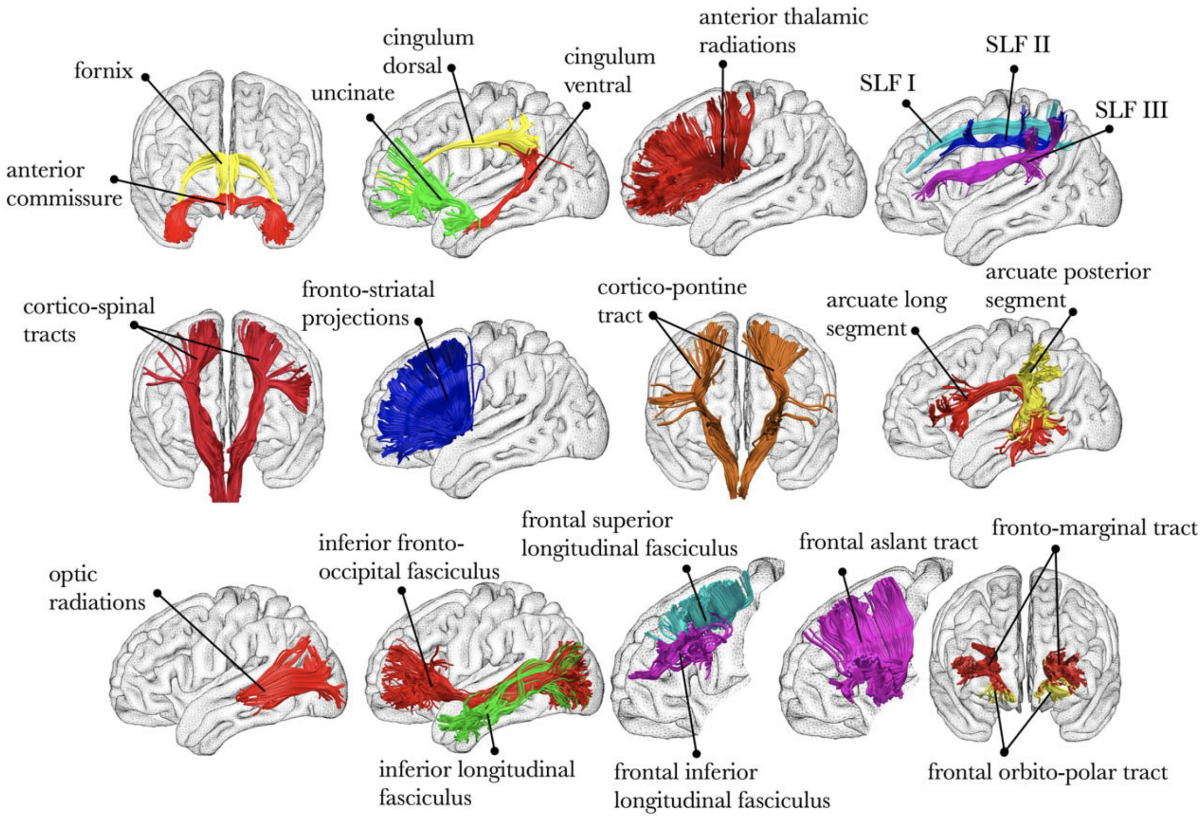


Figure 14: Principal white matter fiber bundles estimated by tractography from diffusion-weighted MRI data. SLF: superior lateral fasciculus. Figure adapted from (Assaf et al., 2019).

## 1.5 Conclusion

In the beginning of this chapter, we introduced the essential neuroanatomical concepts for better understanding the brain anatomical principles. Then, we described the main anatomical issue of our interest, namely the variability of cortical foldings, and some regions of interest or folding patterns proposed in the literature to explain this. In particular, our work focuses on one of these patterns called "Plis-de-passage" and we will study it from both a morphological and a connectivity points of view, using MRI data (anatomical and diffusion MRI). The next chapter presents in details the concept of Plis-de-passage.

# 2 Plis de Passage: a morphological view

## 2.1 Introduction

The cerebral cortex is a very convoluted surface that folds itself into gyri and sulci, which vary a lot across individuals. As early as the 19th century, anatomist were interested in its organisation and features. They observed that many long primary sulci could be subdivided into several pieces but sometimes appeared as a whole. Thses variabilities lead to many unusual folding patterns while creating difficulties for the systematic study of gyri and sulci across different brains (Ono et al., 1990; Regis et al., 2005).

The concept of "Pli de passage" (PPs) was introduced by Gratiolet (1854) to describe transverse gyri that interconnect both sides of a sulcus, are frequently buried in the depth of these sulci, and are sometimes apparent on the cortical surface. These buried gyri were supposed to be related to the U-fibers that bridge the wall of the sulci (Regis et al., 2005). Later on, this term was used by Broca (1888) to depict three transverse gyri that connect the pre- and post-central gyri along the central sulcus(CS): PPs frontal superior, middle and inferior. After that, Cunningham's work of cortical developemnt more clearly showed such sulcal segmentation (Cunningham, 1890a,b, 1897). He described how the central sulcus appeared from two separated folding seeds and then merged with cortical expansion at later stages (Figure 15).

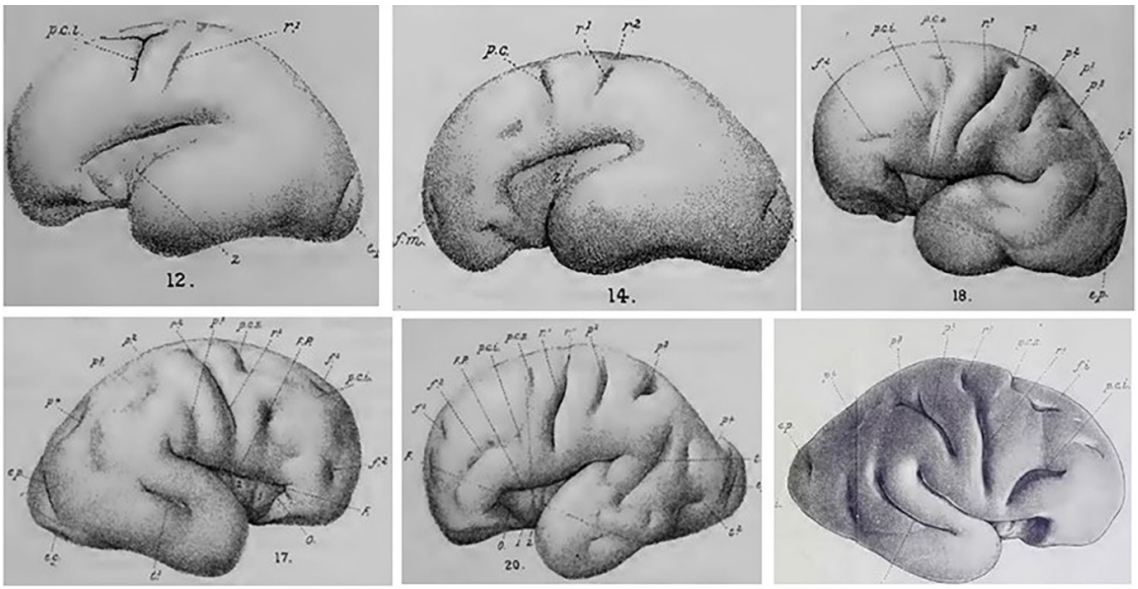


Figure 15: Six hemispheres between the 5th and 7th months of development by D. J. Cunningham. These figures illustrate the apparition of the central sulcus from two separated folding seeds $r^1$, $r^2$. Figures adapted from Mangin et al. (2019)

The PPs, called as "deep annectant gyri" (Cunningham, 1890a,b, 1897), early appeared

as bridges over two isolated parts of sulci eventually buried deep into the bottom of sulci, presented as elevations of fundus or interlocking gyri (Figure 16 (a)). In some cases, this gyrus corresponds to "PPs fronto-parietal moyen"(PPFM) that a type of gyrus exists along the brain development and separate the central sulcus (Cunningham, 1897; Regis et al., 2005; Cykowski et al., 2008)(see Figure 16 (b)). Furthermore, the PPFM or interrupted central sulcus provides a link to the hand motor areas (Boling et al., 1999; Cykowski et al., 2008).

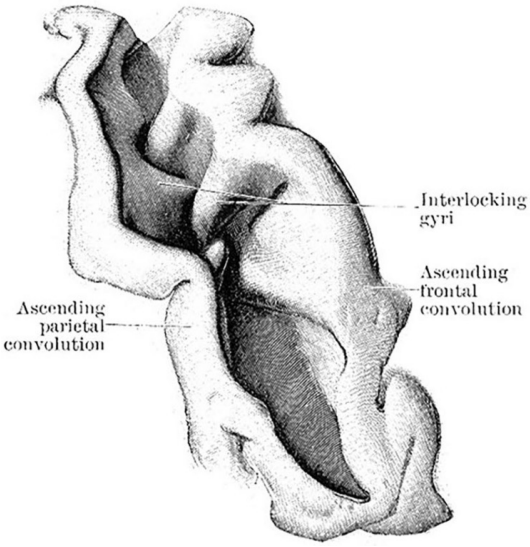


(a)

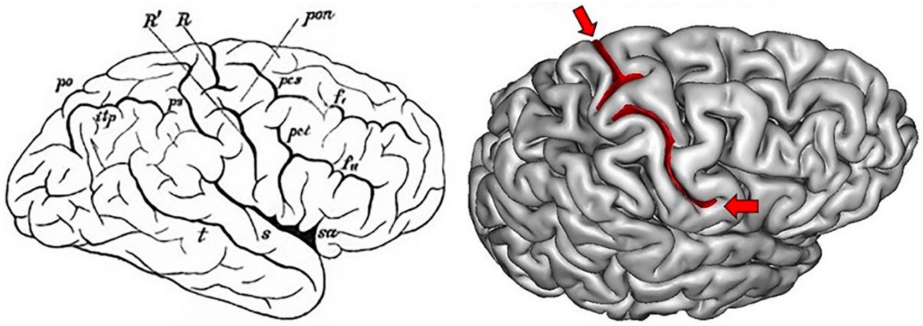


(b)

Figure 16: Different central sulcus morpholgies. In most cases, the PPs were buried in the bottom of sulci as deep annectant gyri in (a), but in less than 1%, the PPs were appeared on the cortical surface as the brain development (Waterston, 1907). (b) Left shows a illustration of interrupted central sulcus Cachia et al. (2003), two parts of central sulcus $R, R'$ are separated. Right shows an hemisphere of the HCP dataset with an interrupted central sulcus viewed in BrainVISA software (Le Troter et al., 2011), the figure adapted from Mangin et al. (2019).

Jean Régis drew the first distribution map of PPs over the entire brain in his MD thesis (Regis, 1994). This map gives the approximate locations of PPs (in Figure 17), which

were deduced from the frequent interruptions of folding patterns within specified brain localization and generally consistent with the initial folding patterns during development (Mangin et al., 2019). As the sulcal variabilities across individuals, the map cannot exactly contain all the PPs, however, it still can be taken as a guideline when we try to explain the individual differences. Jean Régis developed the generic model "Sulcal Root" inferred from the map of the PPs in a hypothetical configuration where each pli de passage reaches the cortical surface, forming a partially interrupted folding pattern (Regis et al., 2005; Régis et al., 1995). Based on the "Sulcal Root" model, Taku Ochiai provided a roughly model to classify the PPs in superior temporal sulcus (STS) according to their location and relative depth of the sulcus (Ochiai et al., 2004). In many recent works of literature, the PPs were gradually studied with name as annectant gyrus, gyral bridge, submerged gyrus (Germann et al., 2005), submerged gyral passage (Zlatkina and Petrides, 2010; Sprung-Much and Petrides, 2018) or transition (Huntgeburth and Petrides, 2012). Several authors have pointed out that the PPs provided an understanding of the variable interruptions in sulci across individuals, and it was recently demonstrated that they can be a useful morphological landmark for models of cortical foldings (Regis et al., 2005; Zlatkina and Petrides, 2010; Mangin et al., 2019; Bodin et al., 2021).

In this section, we study the morphological clues used for identifying the PPs, from the observer-dependent definition "sulcal roots"(Regis et al., 2005), to the variation of sulcal depth profile (Cykowski et al., 2008; Leroy et al., 2015; Le Guen et al., 2018), and finally to the latest characteristics "wall pinches"(Bodin et al., 2021). After that, we will discuss the latest reasearch on the relationship between PPs and U-shaped fibers connnectivity.

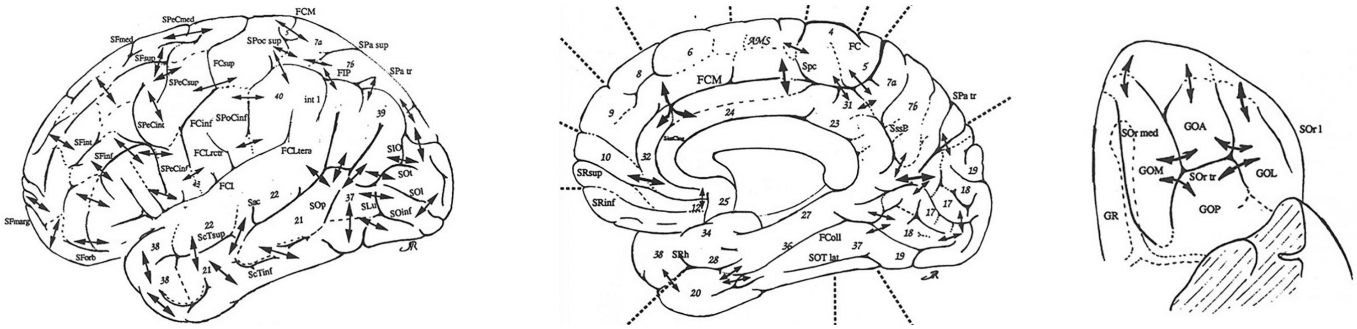


(a) (b) (c)

Figure 17: Map of the plis de passage denoted by double arrows. Figures adapted from Mangin et al. (2019)

## 2.2 Variation of sulcal depth and PPFM

Cortical folding, an essential characteristic of the brain cortex, shows variability across individuals. The morphology of folding is the most basic and direct way to describe the geometric information of various folding patterns. In last decades, the descriptors of cortical folding have been widely studied. Quantitative descriptions of folding patterns(Zilles et al., 1988; Yu et al., 2007; Toro et al., 2008; Li et al., 2010) and understanding of the underlying mechanisms(Van Essen, 1997; Toro and Burnod, 2005; Geng et al., 2009; Auzias et al., 2015; Chen et al., 2017) progressively become important research topics. Among the available folding pattern studies, due to the lack of explicit geometrical definition of the PPs, the PPs have been little studied, mostly in the central sulcus (CS) and superior temporal sulcus (STS). This section introduce the key works related to the morphology of the PPs and their utilization to identify the PPs in CS and STS.

### 2.2.1 PPs and sulcal root

The concept of PPs was introduced to describe transverse gyri that interconnect both sides of a sulcus, are frequently buried in the depth of these sulci, and are sometimes apparent on the cortical surface (Gratiolet, 1854). In general, the cortical gyri are continous with each other and lack of elementary building blocks, so it's difficult to have an explicit definition even the major gyri (Mangin et al., 2019), let alone the various small gyri like the PPs. Consequently the research of anatomy initially more concentrated on the main cortical sulci. Through the summary of 10 years work on various data from literatures and experiments, a putative model "Sulcal Root" map was proposed by Jean Régis (Regis, 1994; Régis et al., 1995; Regis et al., 2005) (see Figure 18). It is important to note that the sulcal root map takes into account the PPs, i.e. the sucal roots are separated by the PPs that reach the cortical surface and cause a local interruption of the folding patterns. Based on this hypothesis, the sulcal root can be represented by the connected parts of the folding pattern this virtual map given the maximum number of interruptions (Mangin et al., 2019).

According to the sulcal root map, Ochiai et al. (2004) analysed the sulcal pattern and morphology of the STS ,and proposed that the 3D architecture of the STS was consistent with their generic model in four sulcal roots and four PPs (see Figure 19 (a)). In their opinion, these gyri were revealed by two kinds of clues: local minima of the geodesic depth along the bottom of the fold and points with negative Gaussian curvature on the gray/white boundary. Herein, the nomenclature of the PPs was derived from its relative height to the sulcal depth and location on the STS respectively. In more detailed, the PPs were separated as follow.

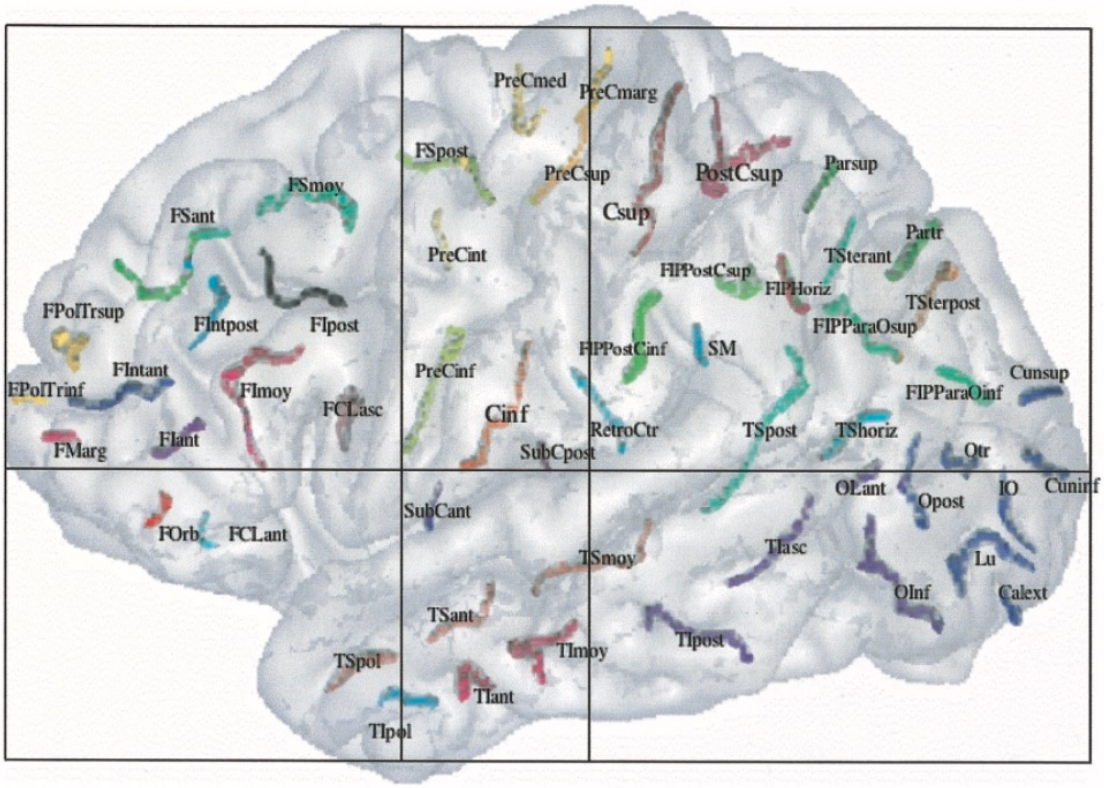


Figure 18: Generic description of cerebral cortex anatomy. The Talairach grid system represents precursors of the sulcal roots in the right hemisphere. The 57 sulcal roots of the lateral aspect are displayed schematically. Figures adapted from Regis et al. (2005)

The height,

- The PPs"superficial": reach 76–100% of the depth of the sulcus
- The PPs "intermediate": reach 26–75% of the depth of the sulcus
- The PPs "deep": reach 1–25% of the depth of the sulcus
- The PPs "invisible": no clear distortion of the bottom of the sulcal shape was visible.

and the location,

- Pli de passage "antero-polar": before anterior sulcal root of the STS
- Pli de passage "anterior": between anterior and middle sulcal root of the STS
- Pli de passage "intermediate": between middle and posterior sulcal root of the STS
- Pli de passage "posterior": between posterior and horizontal sulcal root of the STS

- Pli de passage “ascending anterior”: between horizontal and anterior ascending terminal branch sulcal roots of the STS
- Pli de passage “ascending posterior”: between horizontal and posterior ascending terminal branch sulcal roots of the STS.

In this model, the initial unitary landmarks are the sulcal roots appearing distinctly at the beginning of the gyration (see Figure 19 (b)). Depending on the relative development of adjacent cortical areas, some less-developed gyri can be enfolded by the more developed ones (see Figure 20). As we can see from that, this mechanism leads to the fusion of several sulcal roots into the same furrows in some individuals, while interruption in some others. Furthermore, in fact, the fusion or interruption is caused by the PPs’ variability across individual.

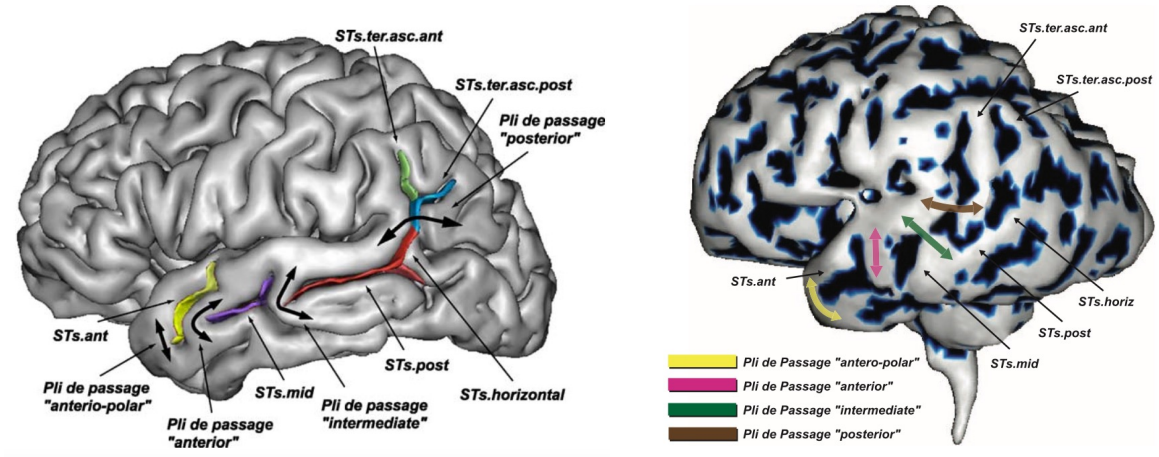


(a) Sulcal roots and the PPs of the STS. (b) Aspect of the 36-week fetus cortex.

Figure 19: (a) The superficial aspects of the sulcal roots and the topography of the PPs are displayed on the surface rendering of the left hemisphere of a normal subject. The first three PPs here are superficial, giving an aspect of interruption. Only the posterior PP is buried (annectant gyrus) requiring the analysis of the 3D shape of the sulcus to be visualized. (b) The first cortical folds that appear on the fetus cortex, called sulcal roots, seem to be especially stable (in number position and orientation) across individuals. During the following gyral expansion, these sulcal roots become buried into the depth of the cortex after having merged with each other to build larger folds. At this early age, the surface rendering allows to visualize very clearly the still superficial sulcal roots of the STS complex. Later, depending on a variety of merging events occurring, a great number of pattern should be observed. (Ochiai et al., 2004)

As an observation-based empirical model, to a large extent, the quality and quantity of data determine the generalizability of the sulcal root map. While more data provides stability, it also inevitably brings more variability. Without accurate standards of measurement,

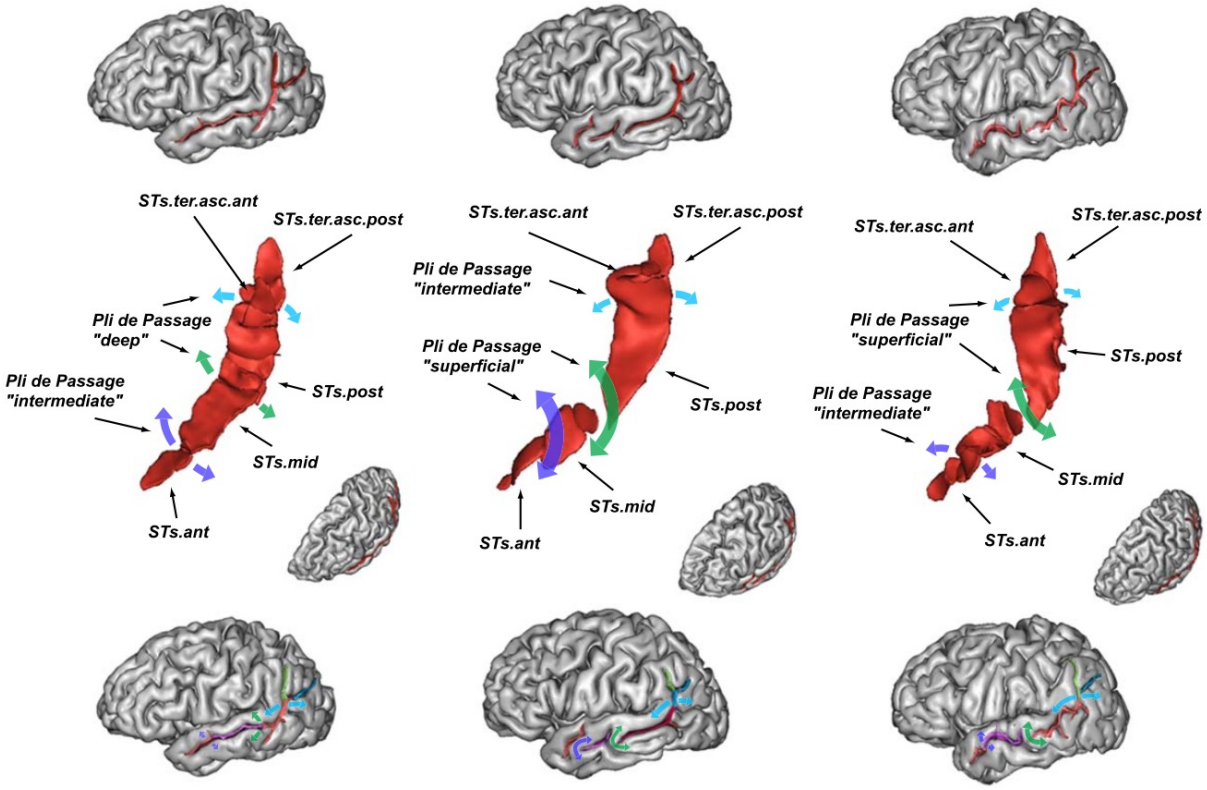


Figure 20: Several different patterns of surfacic drawing of the STS complex. The variability of the superficial aspect of the lateral aspect of the STS complex is presented through the left hemisphere of five normal subjects. This figure attempt to demonstrate that in fact beyond this aspect is hidden in the same generical structure of sulcal roots and PPs. The variability of the depth of the PP and the variability in size of the adjacent gyrus (operculation) are accounting for the difference in the superficial aspect. Figures adapted from Ochiai et al. (2004)

it's difficult to test and extend the sulcal root map. Nevertheless, the concept of sulcal roots still provides a convincing way to understand the folding patterns variability.

### 2.2.2 PPs and sulcal pits

In line with the assumptions of one-to-one correspondence of sulcal roots across individuals, recently, Auzias et al. (2015) proposed a optimization framework to enhance the algorithem of sulcal pits extraction. Sulcal pits are generally known as an explicit aspect of the sulcal roots model (see Figure 21). They are defined as the points of maximum depth within folds, also corresponding to the locally deepest points of cortical surface (Im et al., 2010; Auzias et al., 2015; Im and Grant, 2019), while the interruptions between them are corresponding to the local minimum depth. Hence, back to the definition of the PPs, it is clearly to see that the presence of the PPs can lead to a variation of local sulcal depth. Intuitively,

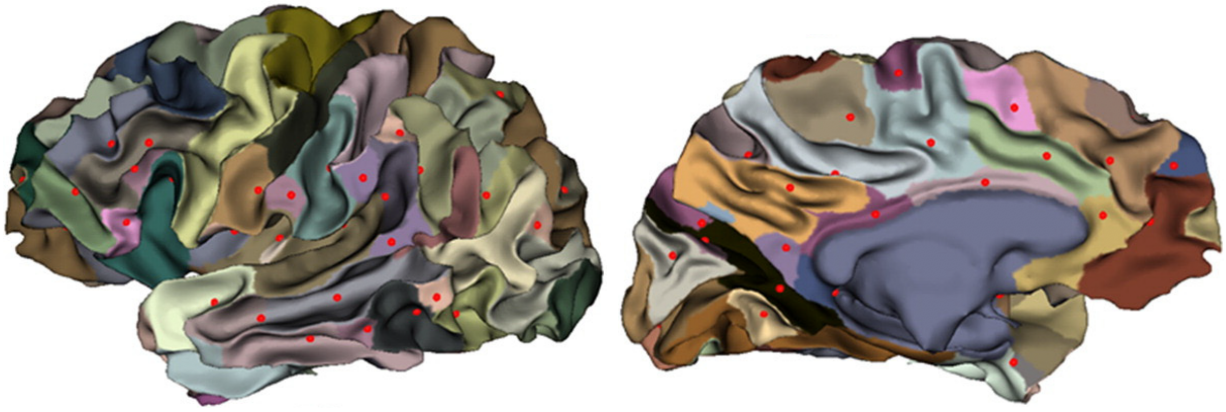

Figure 21: Illustration of sulcal pits in red and corresponding basins for an individual surface (slightly smoothed for visualization purpose). Figures adapted from Auzias et al. (2015)

the sulcal depth is not only related to the sulcal pits/roots but also can be selected as a measurement to identify the PPs. Although very few PPs have been widely studied as the lack of explicit definition, the "Plis de passage frontal moyen" (PPFM), which shows a impressive relationship to the hand sensorimotor areas, raised a lot of interest (Yousry et al., 1997; Boling et al., 1999; Boling and Olivier, 2004).

Most early studies of CS or PPFM are obersever-dependent (Amunts et al., 1996, 2000; Davatzikos and Bryan, 2002). As far as we known, Cykowski et al. (2008) proposed the first obersver-independent quantitive study of CS using automated depth profile tool. They applied a novel method combining automated sulcus reconstruction, surface parameterization, and an observer-independent depth measurement to study the CS. This facilitated the quantitative assessment of the spatial position and intersubject variability of several sulcal landmarks. Furthermore, they developed an algorithm to clearly identification the sulcal landmarks, including the PPFM.

The main processes were demonstrated in Figure 22. The central sulci surface meshes were generated by the BrainVISA sulcal extraction and identification pipeline, and reconstructed as the medial surfaces of 2 opposing gyral banks (Mangin et al., 2004b). The edges and end points of the reconstructed sulcus were determined using topological criteria without manual specificaiton (Malandain et al., 1993; Mangin et al., 1995, 2004b). The top ridge of a sulcus corresponded to a series of points at the junction of the reconstructed sulcus and the brain envelope. Similarly, the bottom ridge of the sulcus was formed from the points at the sulcal fundus. Finally, the intersection of these top and bottom ridges formed the end points of the sulcus (Cykowski et al., 2008).

The reconstructed CS meshes are parameterized into a normalized $x - y$ coordinate

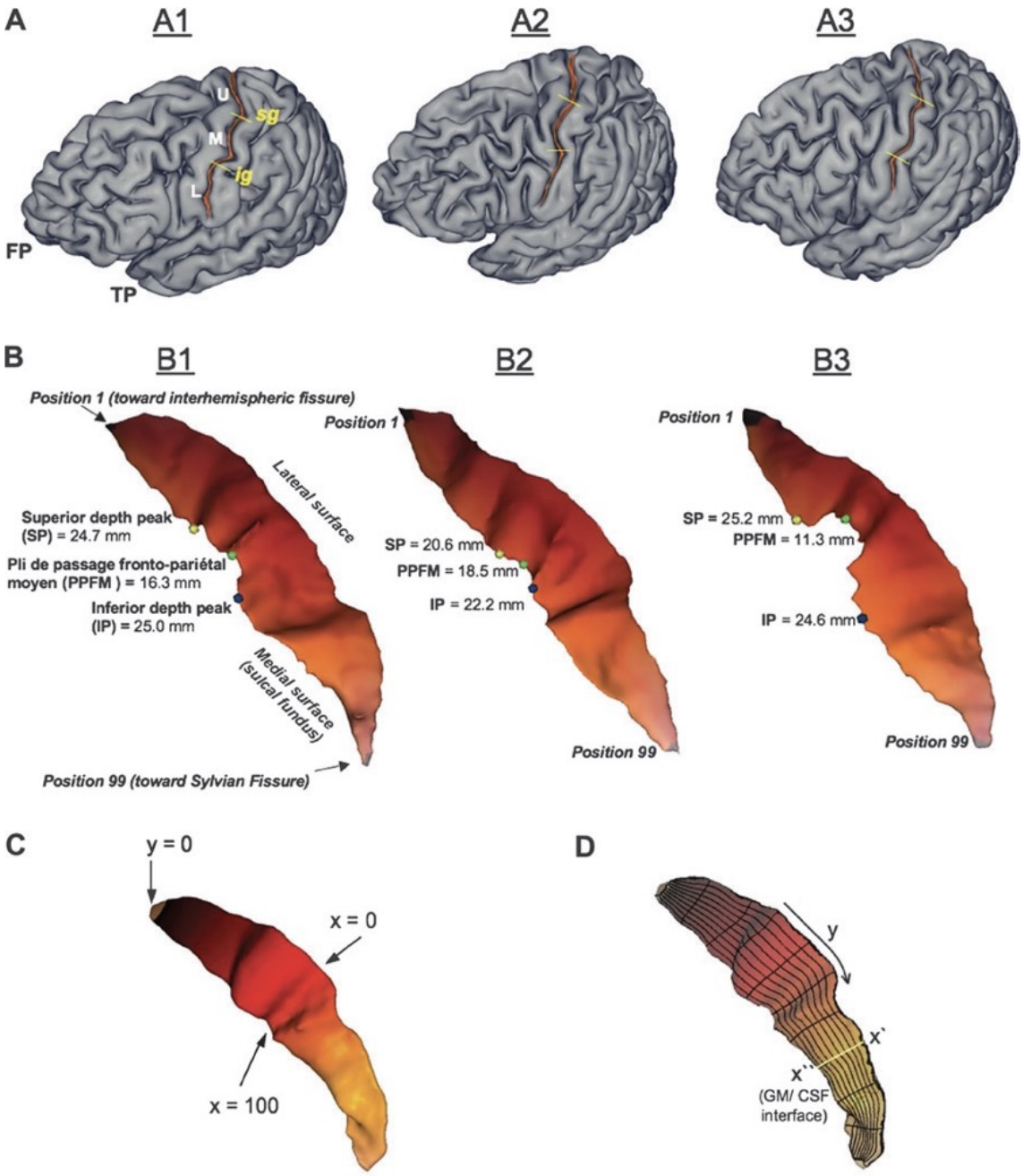


Figure 22: (A) Superficial appearance of the CS. (B) Landmarks of the CS. (C) Sulcal surface parameterization. (D) Depth measure. Figures adapted from Cykowski et al. (2008)

system on their surface (Coulon et al., 2006) (see Figure 22 (C)). The coordinate system extended along the length of the CS from the superior ($y = 0$) to the inferior end of the sulcus ($y = 100$), and from the lateral surface ($x = 0$) to the sulcal fundus (medial edge of the sulcus). The depth was measured at 99 sulcal length positions (hereafter, "positions") in a superior-to-inferior progression along the parameterized sulcal mesh surface. Position 1 was adjacent to the interhemispheric fissure and position 99 was adjacent to the Sylvian fissure (Figure 22 (B)). As shown in Figure 22 (D), sulcal depth at each position is defined as the distance between paired points at the sulcal fundus ($x''$) and brain envelope ($x'$) with the same y coordinate.

The Figure 23 shows the analysis results of the landmarks, including *Superior Peak* (SP), *Inferior Peak* (IP) and PPFM, in CS depth profiles. Herein, the SP was determined to be the maximum depth value in the superior 50% of positions in the depth profile. The IP was recognized as the maximum depth value in the inferior 50% of the depth profile. Bounding the search with these markers, the PPFM was recognized as the minimum depth value between the SP and IP (see Figure 22 (B), 23 (A)). The main limitation of this work is the interruption cases of CS (Figure 16 (b)) since the CS was extracted as a continuous entire surface mesh. Consider the CS that were split into two parts, we cannot paramterize it. Hence, this kind of method cannot be applied to the sulcus with several interruption cases such as STS. Similar works of the PPFM detection using profiles of sulcal depth along the CS have been published later (Hopkins et al., 2010, 2014; McKay et al., 2013; Coulon et al., 2011).

With the development of sucal landmarks extraction algorithms (Im et al., 2010; Auzias et al., 2015; Im and Grant, 2019) and the definition of sulcal fundi proposed by Shattuck et al. (2009), Le Guen et al. (2018) developed an automatic method to extract PPs across the cortex based on a highly reproducible grid of sulcal pits across individuals. Instead of sulci reconstruction, they directly extracted the sulcal depth profiles. First, they identified the sulcal pits from the brain white matter meshes for each individual by the algorithm in Auzias et al. (2015) using the BrainVISA toolbox, and then extracted the sulcal fundus between each pair of sulcal pits. Herein, the sulcal fundus is defined as the shortest path on the white matter mesh following the extremal values of DPF between two extremity points (Shattuck et al., 2009). After the above steps, the PPs were identified as local minima on the two-dimensional depth profile of the sulcus and then binarized and sorted into "true" and "false" PPs depending on their absolute depth value. Some examples are shown in Figure 24.

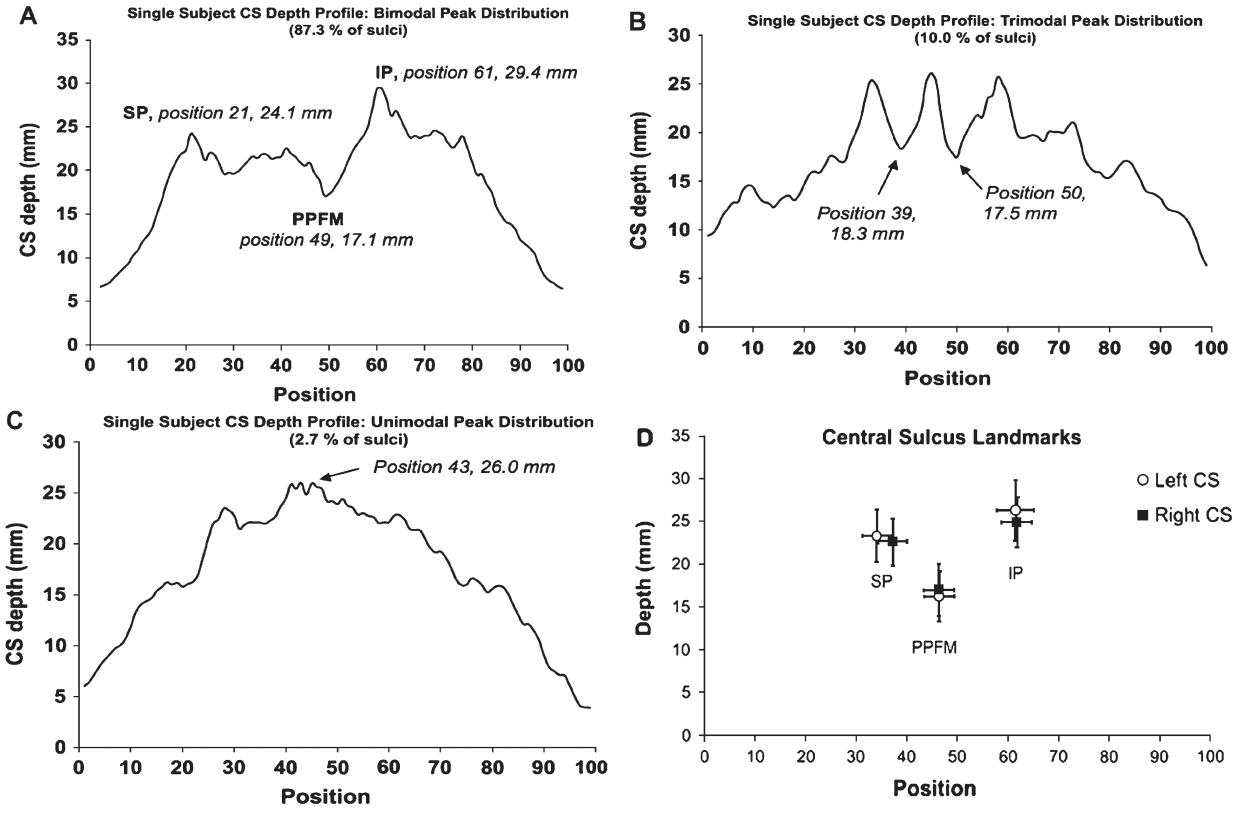


Figure 23: Patterns seen in individual sulcal depth profiles. Sulcal depth profiles of single sulci are shown that are representative of (A) *bimodal*, (B) *trimodal*, and (C)*unimodal* peak distributions. On the profile of a sulcus with a bimodal peak distribution, the superior peak (SP), PPFM, and inferior peak (IP) are labeled. (B) The trimodal profile exemplifies a sulcus for which no PPFM was identified (2 shallow points of nearly equal depth between 3 surrounding peaks). (C) The unimodal profile was seen in only a few subjects. As our algorithm searched the 2 halves of the depth profile for distinct depth peaks, these cases were recognized as a single peak at the middle of the profile with no clear SP, IP or PPFM. (D) The position and depth of the SP, IP and PPFM are shown for the left and right CS. Figures adapted from Cykowski et al. (2008)

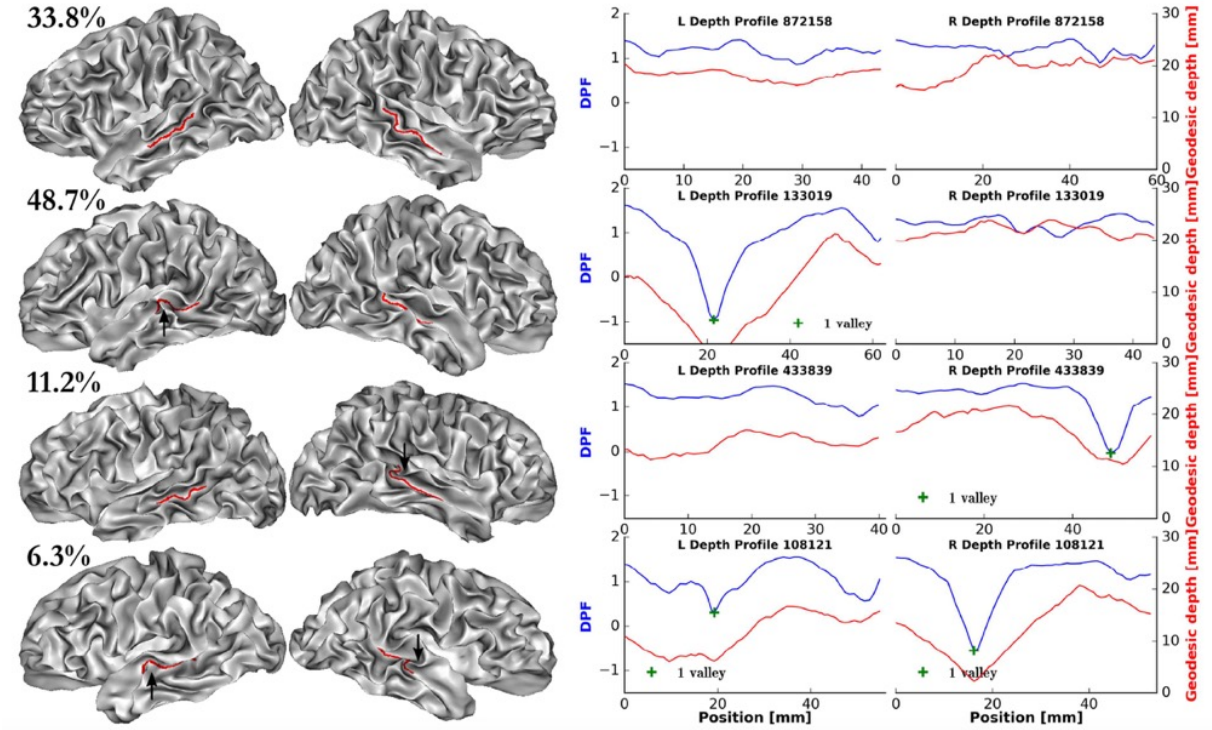


Figure 24: Some examples from Le Guen et al. (2018). Black arrows indicate the pli de passage position on the mesh. Valleys were detected as local minima along sulcal depth profiles with a constraint on both the minimum gap between two valleys and minimum DPF height of the valley floor.

## 2.3 New characteristics: "wall pinches"

As we can see from the above work, the distinct variation of sulcal depth along the sulcal fundus can help us to detect the "superficial" or "intermediate" PPs (according to the definition of PPs in Ochiai et al. (2004)). However, for the points in the deep of sulcal fundus, the specified thresholds of depth are not enough to distinguish the PPs and small fluctuations of fundus, especially the very deep PPs, i.e. "deep" or "invisible" PPs in Ochiai et al. (2004) (see Figure 25). The neglect of these deep buried PPs potentially lose information of sulcus. Furthermore, the binary classification of PPs to as "present" or "absent" from STS depth variations (as in (Leroy et al., 2015; Le Guen et al., 2018)) is insufficient to characterize their topography, namely the spatial arrangement of the different PPs and their respective depth levels (Ono et al., 1990; Ochiai et al., 2004).

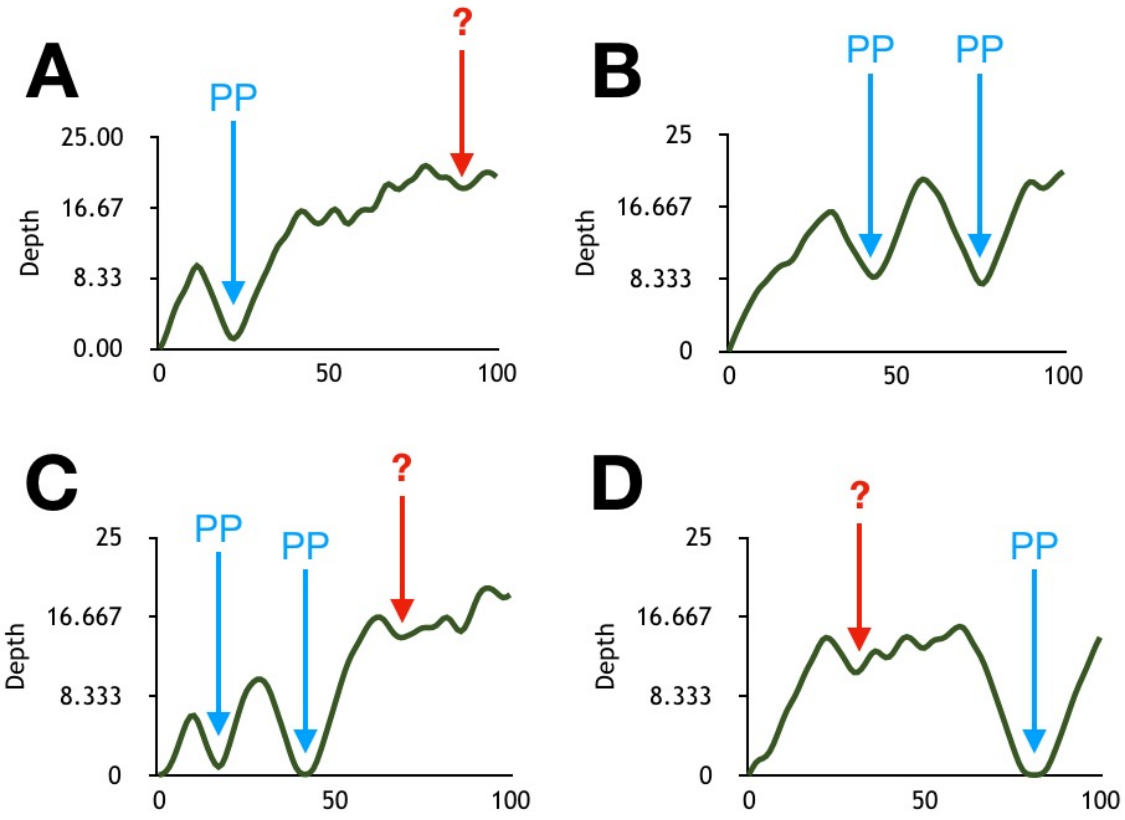


Figure 25: Some depth profiles of STS. The blue arrows indicate the PPs position on the sulcal fundus. The red arrows indicate the points of local minima where it is uncertain whether is PPs. Also, it is common to have many small fluctuation along the depth profile of sulcal fundus. This increase the difficulty to detect the PPs in these regions. Most study based on the depth profile usually discard these points.

Indeed, the PPs are a three-dimensional structures, the identification based on a two-dimensional depth profile is certainly deficient to capture all the PPs (Bodin et al., 2021).

Back to the definition of the PPs (as shown in Figure 16 (a)), the deep buried PPs presented as elevations of fundus or interlocking gyri (Cunningham, 1890a,b, 1897). The elevations of fundus have already been widely studied and successfully used in some kinds of PPs extraction, while the PPs with interlocking gyri has been little studied until recently (Zlatkina et al., 2016; Bodin et al., 2021). Zlatkina et al. (2016) identified deeper PPs which were only 1 mm in depth variation by observing an unusual curved sulcus, and the newly founded deep PPs improved the corresponding with motor funcutions in the post-central sulcus. Inspired by the interlocking gyri, Bodin et al. (2021) mentioned that the PPs were three-dimensional structure whose cortical deformations can be located on the walls of the STS and thus "missed" by the depth profile trajectory. They named the new characteristics of the PPs as "wall piniches" (WPs), moreover, they found the correlation between the PPs and their underlying U-shape fibers connectivity. Figure 26 illustrates the WPs, and all the PPs can be characterized by this local deformation. The "pinching" of the STS walls can be clearly oberved for the superficial PPs but also true for the deep PPs with a lesser degree, and they are exactly the interlocking gyri.

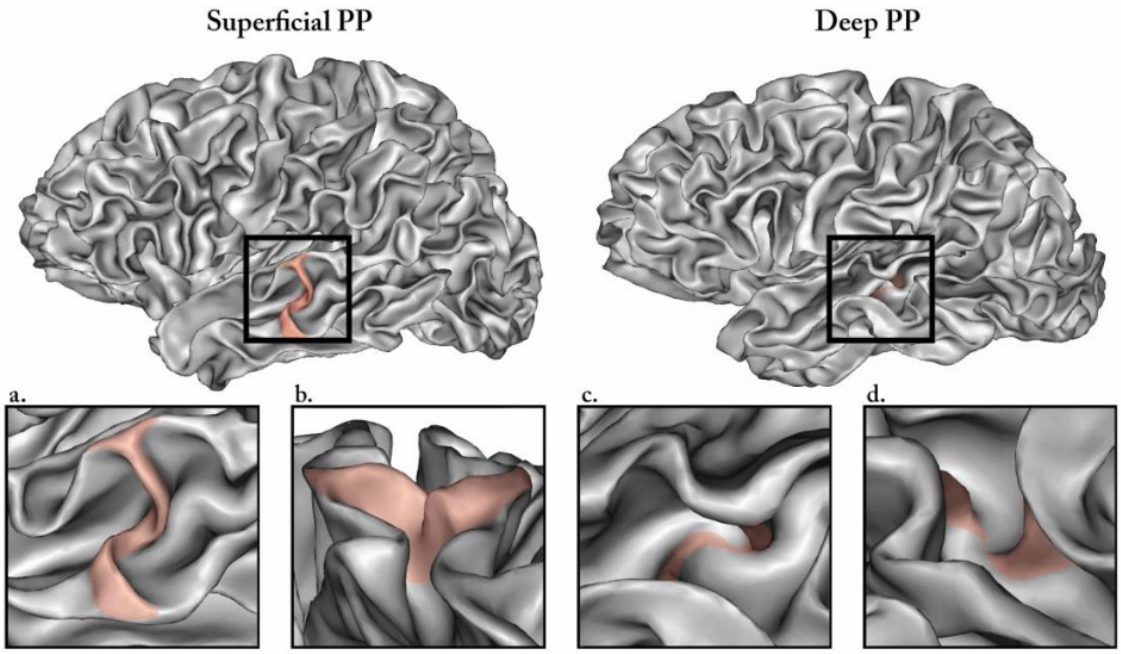


Figure 26: Local cortical morphology observed for superficial and deep PPs (colored areas) illustrated in two example subjects. Only the superficial PP causes a clear separation of the main STS furrow. However, a thorough observation (from above: a,c or lateral: b,d) reveals a pinching of the adjacent walls in both cases, whose visibility is a matter of degree. Figures adapted from Bodin et al. (2021).

Since the PPs were characterized by two corresponding WPs on the adjacent gyri walls, several criteria were used in Bodin et al. (2021) to facilitate the identification of the WPs

(see Figure 27). For a good visualization of the distortion of the cortical sheet, the DPF and curvature thresholds were carefully selected for each individual surface maps. As shown in Figure 27 (B), the superficial PPs, clear sulcal interruptions, showed a strong decrease of the DPF within the sulcus and a high curvature forming a thick and continuous line on the map. However, the deep PPs were less visible and needed more observations based on variable thresholds of the DPF and curvature maps. A typical morphlogical characteristic of the deep PPs is that the WPs are "facing each other" and form a superfical crest and a convex angle respectively. This can be easily observed on the DPF and curvature maps (Figure 27 (B) Deep PPs). Based on the observation above, Bodin et al. (2021) hypothesized that WPs of deep PPs were of the same nature than those observed for superficial PPs and that the former constitute a less connected variant of the latter. If the two WPs are well connected each other they constitute a superficial Pli-de-passage (PP), whereas if they are not (or too deeply) connected they constitute a deep PP.

Bodin et al. (2021) identified from 2 to 8 ($Mean = 4.5$) PPs in the left STS against 1 to 7 ($Mean = 4.3$) in the right STS, and there is no significant difference across individuals ($p = 0.1$, Wilcoxon). In order to differentiate the superficial and deep PPs, they used the similar standard of DPF in Le Guen et al. (2018) but with slight differences. The PPs were classified into a "superficial" (DPF$\leq$ 0.42) and a "deep"(DPF$>$ 0.42) category instead of "true" or "false" PPs. Based on this classification, the individual proportions of deep and superficial PPs differed significantly ($p < 0.05$, Wilcoxon) between left and right hemispheres. Thus, while the absolute number of PPs does not seem to vary much from one hemisphere to another, their depth is asymmetrical with a greater proportion of superficial PPs in the left STS. It should be noted that this asymmetry of PPs also reinforce the well-known landmarks "superior temporal asymmetrical pit"(STAP) (Leroy et al., 2015), that is the PPs in the right STS are located in deeper regions than the left and is in agreement with the fact that the right STS is notoriously deeper than the left STS (Bodin et al., 2021; Song et al., 2021).

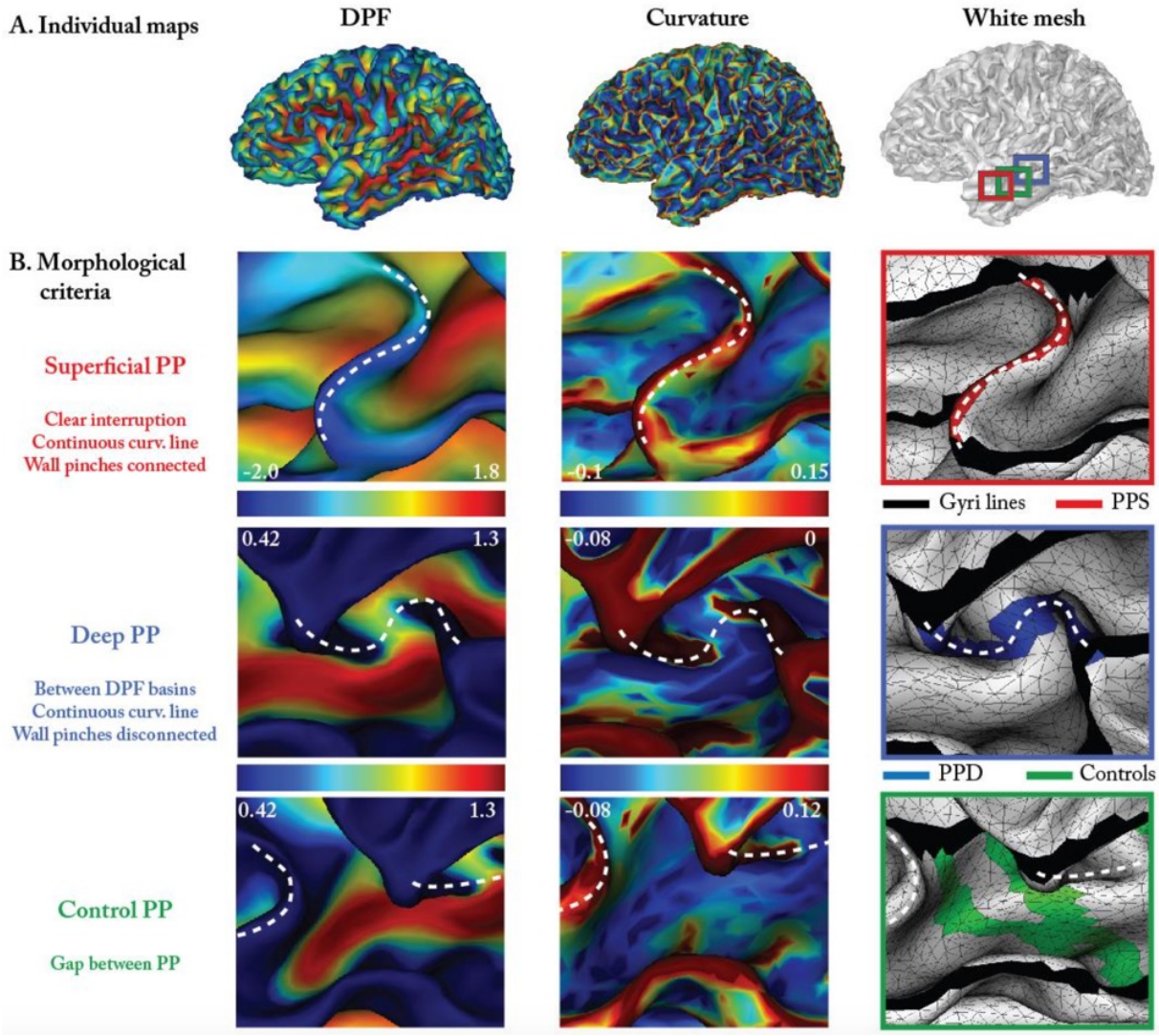


Figure 27: Methods for PPs identification, illustrated for one subject in the left hemisphere. (A) Surface maps generated in BrainVisa and projected on the white matter surface. DPF (depth potential function) map shows an increasing depth from blue to red color. Curvature (finite element method) map shows an increasing curvature from blue to red color. (B) Morphological criteria used to characterize PPs (white dotted lines). Zoom windows of the surface maps illustrate the manual drawing of one superficial (in red) and deep PPs (in blue) as well as controls generated automatically. Once detected from depth and curvature criteria, PPs were drawn by selecting the two intersections (two vertices) between the PPs crest and gyri crests. A line is then automatically generated between this pair of vertices passing by the shortest past and constrained by minimal DPF values (line crest). Controls (in green) are generated using a similar procedure except that their position is generated automatically into the gaps separating PPs locations. If there is enough space, several controls are generated with different orientations. White numbers below color bars indicate the DPF and curvature thresholds employed for each representation. Figures adapted from Bodin et al. (2021).

## 2.4 Conclusion

The PPs, a classical anatomical phenomenon well described during the 19th century, was little studied for a long time afterwards due to the lack of a clear and specific definition until the end of 20th century. With the developments of image processing, computer graphics and visualizations, more and more tools were created to help us understand more about the brain morphology patterns including the PPs.

The PPFM has become a subject of interest with the advent of functional imaging, because several studies have shown striking relationships with the hand sensorimotor areas (Yousry et al., 1997; Boling et al., 1999; Boling and Olivier, 2004; Cykowski et al., 2008; Coulon et al., 2011; Mangin et al., 2019). The STAP, a human-specific asymmetry in the STS at the heart of the communication regions, is deeper in the right hemisphere than in the left. It was explained in part by the larger number of sulcal interruptions, namely the PPs, in the left than in the right hemisphere (Leroy et al., 2015; Bodin et al., 2018; Le Guen et al., 2018; Bodin et al., 2021; Song et al., 2021).

Furthermore, the clear relationship between these PPs and the local regional cortical functional organization lead to more exploration of the potential meaning of the PPs both in human and non-human species. Hopkins et al. (2010) studied the PPFM in the CS of the chimpanzee brain. Sprung-Much and Petrides (2018) found a submerged gyral passage were always appeared in the Broca's area, which is known as the motor speech area. Cachia et al. (2018) has shown that a superficial PPs in the visual word form area has a positive impact on reading skills. Mangin et al. (2019) mentioned a quasi-interrupted central sulcus after browsing the chimpanzee brain collection of W. Hopkins.

Containing the studies mentioned in this chapter, there is a growing body of research showing that the PPs not only can constitute landmarks for a better understanding of the inter-individual variability, but also relate to some brain functional areas. To reveal the nature of the PPs, much more work is needed. Including but not limited to the tension-based morphogenesis (TBM) based on physical forces (Van Essen, 1997; Llinares-Benadero and Borrell, 2019; Van Essen, 2020; Garcia et al., 2020), and the U-shape fibers connectivity structures underlying the PPs or cortical foldings (Mangin et al., 1998; Bodin et al., 2021; Pron et al., 2021; Zhang et al., 2014, 2020a).

In particular, readers interested in a detailed discussion can refer to (Regis et al., 2005; Ochiai et al., 2004; Cykowski et al., 2008; Le Guen et al., 2018; Bodin et al., 2021). Also, several very interesting studies based on local folding patterns to depict the specific configuration of regional PPs have been proposed (Germann et al., 2005; Zlatkina and Petrides, 2010; Zlatkina et al., 2016; Huntgeburth and Petrides, 2012; Sprung-Much and Petrides,

2018).

In this chapter, we mainly discussed the PPs from a morphological methodology perspective. Some of these morphological clues have been implemented in automated algorithms or pipelines (Cykowski et al., 2008; Le Guen et al., 2018) but limited to depth based definitions, most have not. As the development of machine learning methods, most computer graphics, computer visualization and vision problems have been well solved, and even outperformed than experts. In the next chapter, we will proposed the machine learning method to automatic detect the PPs based on the newest characteristic WPs in (Bodin et al., 2021).

# 3 Automatic detection of Plis de passage from morphology

## 3.1 Introduction

Plis de passages (PPs), namely annectant gyri buried inside the fold, can explain part of the sulcal variability. To our best knowledge, the only existing automated detection methods of PPs are based on the depth profiles of sulcal funudi. The PPs have been described as protrusions in the fundus of sulci between the two walls, and were therefore generally extracted as local minima of the sulcal depth along the fundus, with a threshold on the depth value (Cykowski et al., 2008; Le Guen et al., 2018). Unfortunately, these algorithms are also affected by the drawback of the two-dimensional depth profile, i.e. it is not enough to identify all the PPs by only using the variation of depth in sulcal fundus (Bodin et al., 2021). In particular, they missed a significant number of deep buried PPs that are without clear depth variations or not within the specified thresholds. This led to controversial results such as an asymmetry of the number of PPs in the superior temporal sulcus (STS) between the left and right hemispheres (Bodin et al., 2021; Leroy et al., 2015; Le Guen et al., 2018; Song et al., 2021).

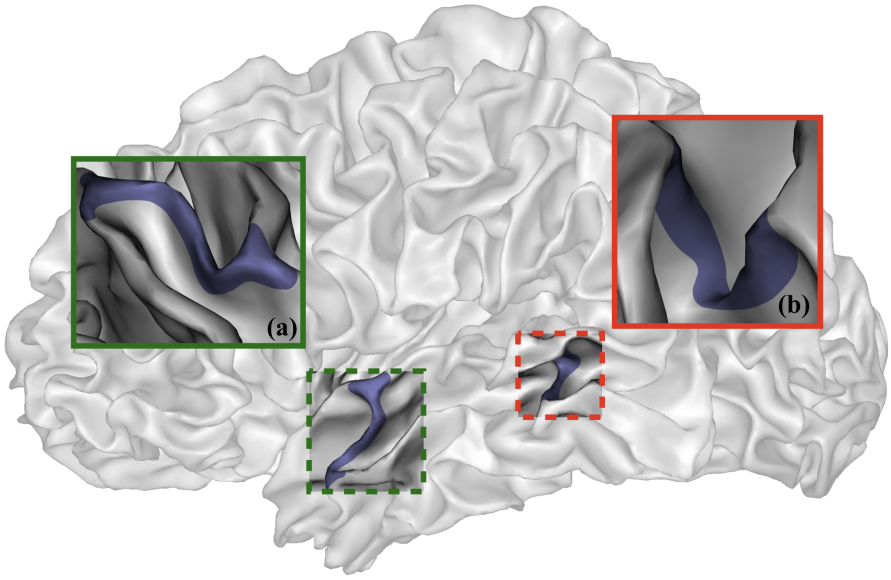


Figure 28: Local morphology to identify the superficial and deep PPs. (a) Superficial PPs; (b) Deep PPs. The wall pinches can be observed clearly for superficial PPs but also exist for the deepest buried PPs.

To overcome this drawback, Bodin et al. (2021) proposed a new three-dimension morphological characterization of PPs in the STS using the surrounding surface geometry, named

"wall pinches" (WPs) (see Figure 28). The concept of WPs is similar to the "interlocking gyri" (Cunningham, 1890a,b, 1897), and establishes a continuum from a superficial apparent transverse gyrus to a completely buried PP with only wall deformations left. In our work, we propose to automate the detection of PPs in the STS using machine learning and this new morphological characterization.

In this chapter, we first present the data and the preprocessing steps. Particularly, we use the same manually labelled PPs in (Bodin et al., 2021) and the detection of PPs will be a classification of the STS fundus points and we want to decide if they are on a PP or not. Then we will introduce the morphological tools we used to capture the characteristics mentioned in (Bodin et al., 2021), named "Cortical surface profiling"(Li et al., 2010). By using this tool, for each point of STS fundus, we generate the feature vector (2-dimensional image). Hence, the detection of PPs is converted to a supervised image classification problem. After that, we propose the machine learning models in our study to solve this problem. At last, we will present the experimental results and discussions.

## 3.2 Subjects and image acquisition

In this work, we used two completely independent datasets, where one is used for training and testing the machine learning models and the other for empirically evaluating the performance of our methods.

### Human Connectome Project dataset

The first dataset is composed of structural T1 MR images of 100 subjects from the Human Connectome Project (HCP) database, for which detailed information is available: 900 Subjects Data Release Reference. Subjects were randomly having completed the full diffusion and structural acquisitions, being non-twins, right-handed, between 22 and 40 years old.

Data taken from the HCP database were acquired as follows: structural images were acquired using a modified version of Siemens Skyra 3T scanner (Siemens, Erlangen, Germany) with a maximum gradient strength of $100mT/m$, slew rate of $200T/m/s$ (reduced to $91T/m/s$ for diffusion due to peripheral nerve stimulation limits) and a 32-channel head coil. T1-weighted images were acquired using 3D MPRAGE sequence (TR/TE = $2400/2.14ms$, flip angle = 8, FOV = $224 \times 224mm^2$, resolution = $0.7mm$ isotropic). Note that this dataset have been already used in (Bodin et al., 2021).

#### Temporal Voice Areas dataset

The second dataset is composed of structural T1 MR images of 92 subjects, aged between 17 and 44 years old, from the Temporal voice areas (TVA) dataset previously used in Bodin et al. (2018). The origin dataset contains one-hundred and sixteen healthy subjects that were scanned (n = 116; 53 males, 63 females; mean age $23.7 \pm 5.8$) as part of published and unpublished experiments of the Voice Neurocognition Laboratory (http://vnl.psy.gla.ac.uk/) of the Institute of Neuroscience and Psychology at University of Glasgow. Participants, drawn mostly from the Glasgow student population, were of various ethnic backgrounds, education and manual lateralization and all provided written informed consent prior to participation. The experiments were approved by the local ethics committee at University of Glasgow. Exclusion of subjects was due to the failure for the depth profile extraction.

All scans were acquired on a 3T Siemens (Erlangen, Germany) Tim Trio scanner at the Centre for Cognitive Neuroimaging (http://www.ccni.gla.ac.uk/), University of Glasgow. High-resolution 3D T1-weighted sagittal scans were acquired for each subject (voxel size 1 $mm^3$ isotropic; acquisition matrix $256 \times 256 \times 192$).

## 3.3 Image preprocessing and identification of PPs

### 3.3.1 Anatomical images and related maps

All individual T1-images were first segmented using Freesurfer (https://fsl.fmrib.ox.ac.uk/fsl/fslwiki), and then imported into the *Morphologist* pipeline of the BrainVisa (BV) software (http://brainvisa.info) (Mangin et al., 2004a) to generate triangular meshes of the grey/white matter interface for both hemispheres of all subjects (see Figure 29 (a)). These surfaces will be further referred to as "cortical surface".

Then, we generated several morphological surface maps used for anatomical analysis including sulcal depth, depth potential function (DPF) and curvature map. The depth map for each individual surface was computed as the geodesic distance from the sulcal fundus to the outer cortex (see Figure (Rettmann et al., 2002) 29 (b)).

The DPF map is used the depth potential function (Boucher et al., 2009), as already done in (Auzias et al., 2015). It is known to provide a regularized estimation of the sulcal depth that considers the information from both convexity and curvature. Importantly, it was also shown independent of brain size and therefore does not require a normalization procedure (Auzias et al., 2015). DPF measure can be either negative or positive depending on whether the vertex is superficial or located in the depth of a sulcus (see Figure 29 (c)).

The curvature used in this study is the mean curvature. For all cortical surfaces, we generated their curvature maps using a finite element method as implemented in BrainVisa. In general, the vertices in the sulcal fundus have low curvature value while gyri crowns show high curvature (see Figure 29 (d)).

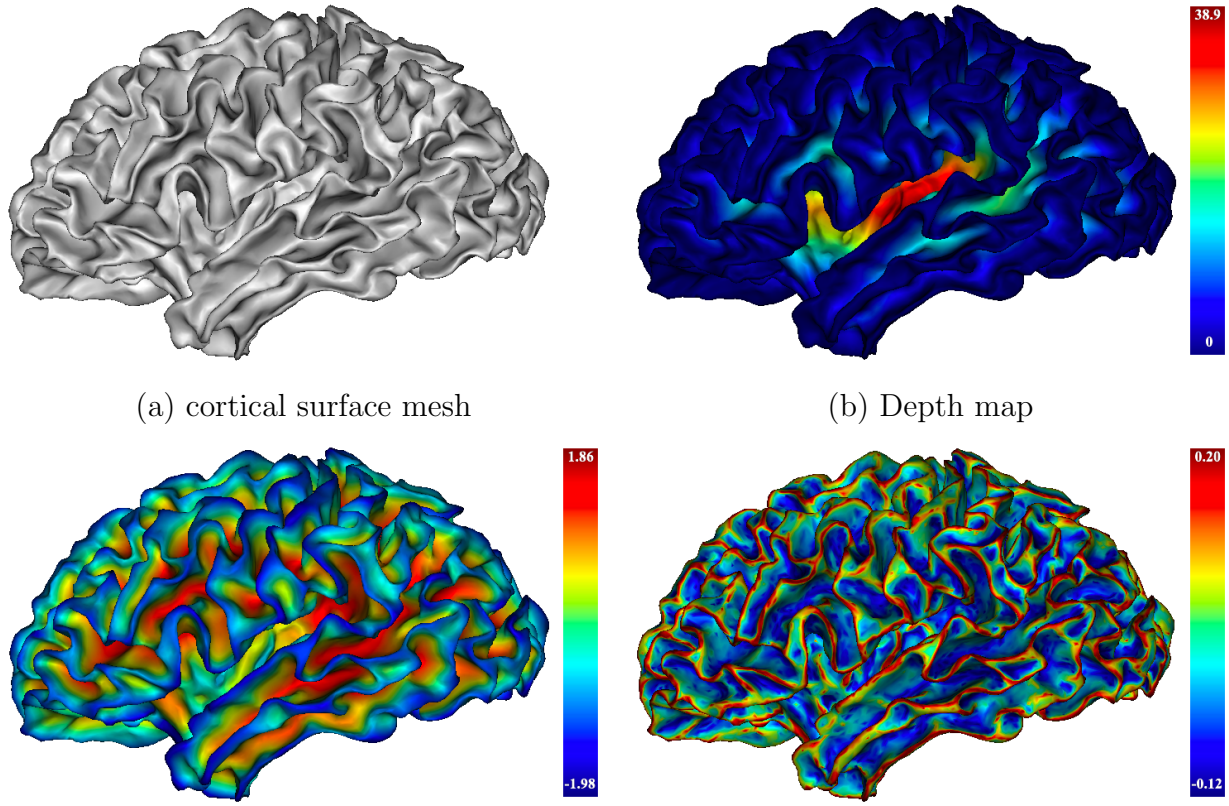


(a) cortical surface mesh (b) Depth map

(c) DPF map (d) curvature map

Figure 29: Examples of anatomical images and maps.

### 3.3.2 STS identification and drawing

The STS is a highly distinguishable fold separating the superior temporal gyrus (STG) from the middle temporal gyrus (MTG) in the temporal lobe (see Figure 30 (a)). The STS fundi were drawn semi-automatically on the cortical surface for both hemispheres and all subjects of both datasets using the SurfPaint module of the Anatomist visualization software (Le Troter et al., 2011). This was performed by C. Bodin in the context of Bodin et al. (2018, 2021). We manually selected the anterior and posterior extremities based on anatomical landmarks identifiable in each subject as described in Bodin et al. (2018). The anterior extremity was chosen as the tip of the temporal pole, posterior to polar temporal sulcus. In most cases, this sulcus was perpendicular to the STS and a clearly visible PP

separates these two folds (Ochiai et al., 2004). The posterior extremity was chosen at the intersection between the STS horizontal main branch and its posterior ascending branches (Segal and Petrides, 2012). The fundus of the STS was drawn automatically between the two extremities as the shortest path that minimizes the DPF between the extremities(Le Troter et al., 2011).

### 3.3.3 PPs identification

Herein, the PPs were manually labeled on the HCP dataset by C. Bodin in the context of Bodin et al. (2021) according to the morphological criteria described in (Bodin et al., 2021). In order to identify the PPs, we need to find the WPs first. Hence, the WPs were first highlighted by carefully varying the DPF and curvature thresholds on the cortical surface maps. Once detected from depth and curvature criteria, PPs were drawn by selecting the two intersections (two vertices) between the extremities of WPs and gyri crests. A line is then automatically generated between this pair of vertices passing by the shortest past and constrained by minimal DPF values (see Figure 27). For both hemispheres of the 100 subjects of HCP data, Bodin et al. (2021) identified individually all PPs in the STS that connect the two adjacent gyri crest (STG, MTG) and traverse the STS fundus (some examples in Figure 30 (c)). For all points of the STS fundus, those at the intersection with PPs lines were labelled "PP" and the rest were labelled "non-PP" (see Figure 30 (d)).

## 3.4 Feature extraction and feature images

Compared to the previous work using the 2D information of sulcal depth or DPF(Cykowski et al., 2008; Le Guen et al., 2018), the advent of WPs led to a more reliable way to identify the PPs, but automating it is also challenging. In order to automatically detect the PPs for all the brain, it is important to make the PPs comparable first. Meanwhile, the drawbacks of the DPF and curvature maps, i.e. the need for various thresholds to identify different WPs, motivated us to find better representation of WPs. In this section, we introduced the method used to generate new feature maps of cortical surface, called cortical surface profiling (Li et al., 2010). Furthermore, by using this method, we generated the feature images recording the local geometric informations as the data used in automatic detection of PPs.

### 3.4.1 Cortical surface profiling

If we consider the vertex at the intersection of a PP and the sucal fundus, the WPs are always located between this vertex and the two surrounding gyri. Hence, we need to define

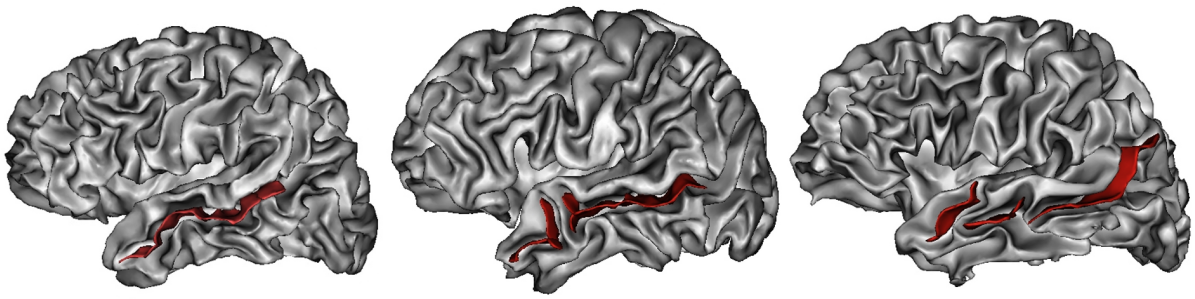

(a) STS

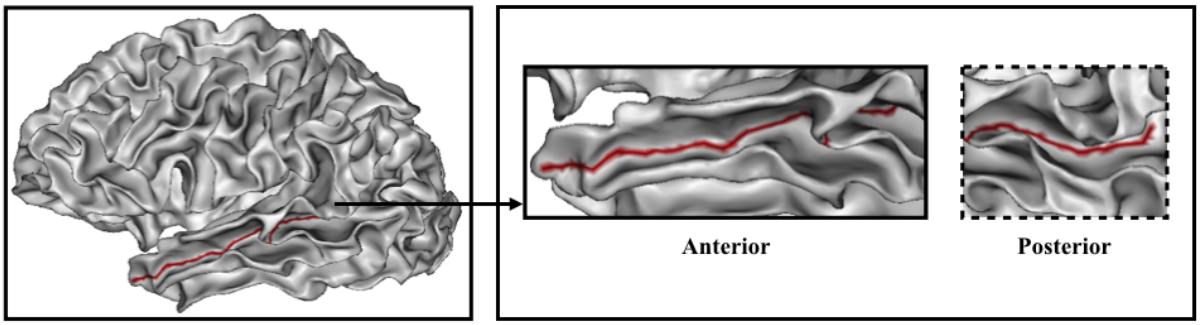


(b) STS fundus

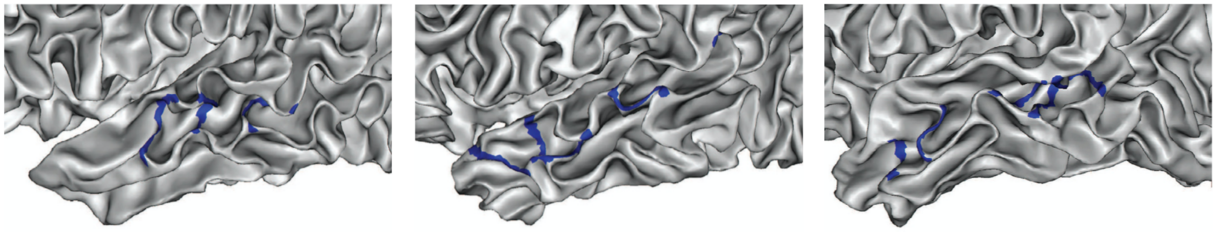

(c) Labeled PPs in STS

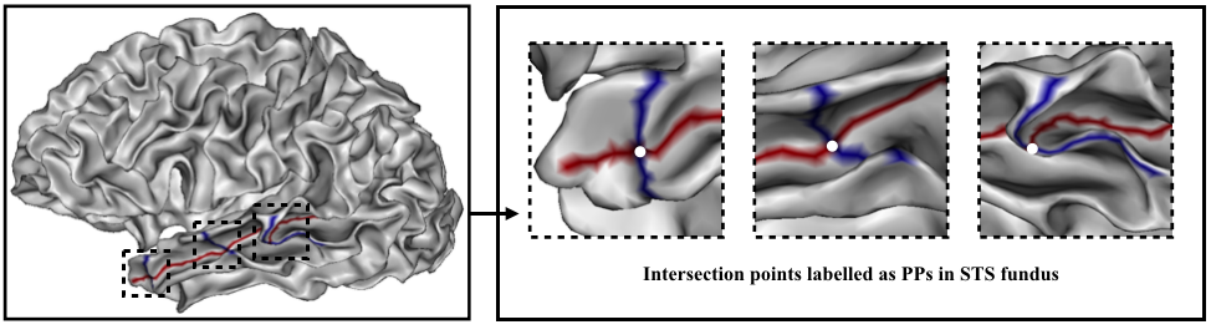


(d) Vertices labelled as PPs in STS fundus

Figure 30: (a) Examples of three different STS. The model in red is the STS. Figures adapted from Lefèvre and Mangin (2010) (b) Example of STS fundus (in red) generated by the semi-automatic methods. (c) Examples of labeled PPs in STS. Figures adapted from Bodin et al. (2021) (d) Examples of labelled PPs vertices (in white) in STS fundus.

local morphological features that can capture the presence of WPs around a STS fundus vertex. As the cortical surfaces were generated as triangle meshes, the simplest method is to get sub-meshes that define regions of interest within a specified geodesic distance or n-ring neighborhood of each sulcal fundus vertex. However, it is difficult to ensure all sub-meshes containing the same number of vertices because of the complexity of gyral folding leading to imperfect reconstruction of the cortical surface. This prevents comparison between different sub-regions. Although many reparameterization methods of triangle mesh can project different meshes onto a unit shape (a circle or square) to make them comparable, the deformation and ambiguity brought by the parameterization still needs to be treated according to the practical issues. Instead of defining a sub-mesh, we used a sampling method on the cortical surface called "cortical surface profiling" (Li et al., 2010), which was inspired by the methodology on folding pattern analysis of rocks in geology .

The basic idea of cortical surface profiling is, for each point of the cortical surface, to represent the 3D shape information of a cortical surface patch around the point, with modeling parameters of a series of 2D profiles. For each vertex on a cortical surface, Li et al. (2010) combines a 3D Cartesian coordinate system (Tao et al., 2002) and a 2D polar coordinate system to built a new local 3D coordinate system (see Figure 31). For a vertex $O$ on the cortical surface $S$, we can get its normal direction $N$ and tangent plane $P$. Consider the normal direction $N$ as the Z-axis in a 3D Cartesian coordinate system and the tangent plane $P$ as the space of a polar coordinate system, with an arbitrary orientation origin $R_0$. Note that there is no specific given X-axis or Y-axis in this 3D coordinate system in comparison with the 3D Cartesian coordinate system.

Based on this 3D coordinate system, for a given vertex and its local cortical surface patch, the profiling process is as follow. First we randomly select the starting direction $R_0$ and set the rotation angle as $\alpha$. $R_\alpha$ is the radial direction after rotating to an angle $\alpha$ from $R_0$. The profile of the local surface patch in the direction $R_\alpha$ is recorded as $C(\alpha, x, y)$, where $x$ is the radial distance of a point on profile to the normal direction $N$, and $y$ is the normal distance of the point to the plane $P$ The profiling process is conducted every $\theta$ degrees around the circle direction, which will generate $360/\theta$ profiles for the local cortical surface patch. Each profile is sampled with a radial step $s$, and the sampling stops when reached the maximum number of sampling points $M$. Figure 32 shows an example of sampling result and one profile. The essence of cortical surface profiling is using a collection of 2D profiles to sampling the 3D local surface patch. By specifying the sampling parameters, we generate comparable profiles of same size.

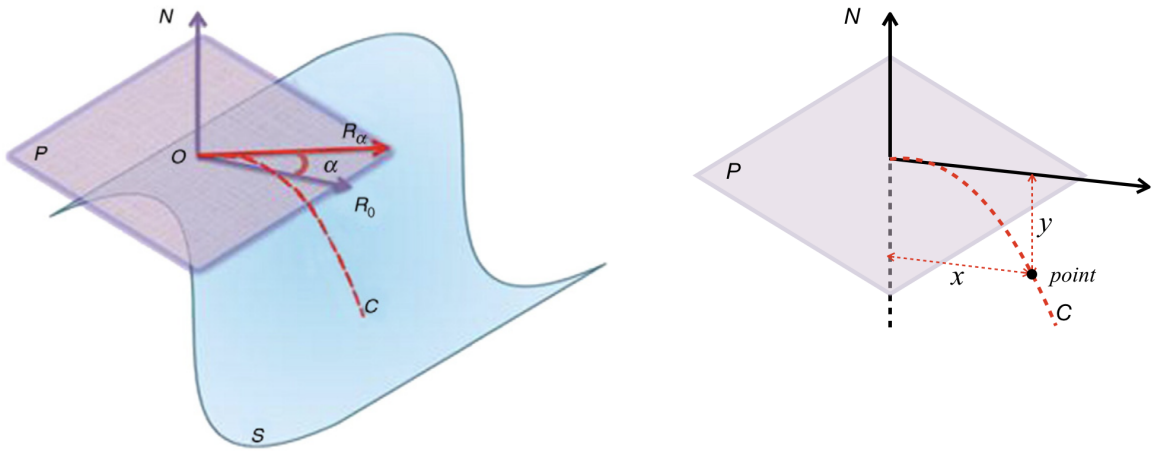


Figure 31: An illustrative figure to show the coordinate system. $O$ is any vertex on the cortical surface $S$; $P$ is the tangent plane; $N$ is the normal direction of vertex $O$; $R_0$ is the starting direction of sampling; $R_\alpha$ is the sampling direction with $\alpha$ degree away from $R_0$; $C$ is the sampling profile at direction $R_\alpha$. Figures adapted from Li et al. (2010)

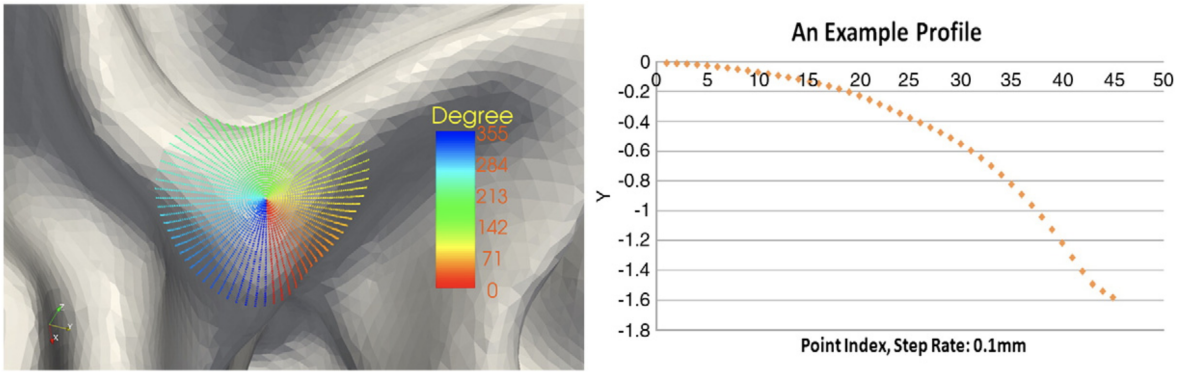


Figure 32: An example of profiles. Sampling parameters: $\theta = 5°$, $s = 0.1$, and $M = 45$ Figures adapted from Li et al. (2010)

### 3.4.2 Morphological feature maps of cortical surface

After we get the local cortical surface patches by surface profiling method, the next step is to select or create a cortical surface feature map that clearly identifies the WPs on the gyri walls. In (Bodin et al., 2021), the DPF and curvature maps were used to facilitate the identification of PPs. For a visual impression, Figure 33 illustrates the same anatomical maps with various selected thresholds. As we can see, the thresholds of both two maps need to be carefully selected in order to distinguish the WPs from the surrounding flat areas for each individual. In details, the variation of DPF values (from blue to white) is more responsive to the depth variation from gyral crest to the sulcal bottom than the distortion of gyral wall. In comparison to the DPF, the curvature maps show a better distinguishment between the WPs and surrounding flat regions, but it is still difficult to find the WPs of deep PPs without a proper threshold. Herein, the regions with positive curvature value correspond to the gyri crests or wall pinches. As shown in Figure 33 (b) the initial curvature map without varying thresholds, only few scattered positive curvature areas can be seen on the STG walls. Besides, the irregular gyral walls with small sags and crests also increase the difficulties. Notably these uncertainties make it ambiguous to detect all the PPs only by setting thresholds for all the individuals.

To solve these uncertainty of DPF and curvature maps, we select two geometrical maps computed from the cortical surface profiling, namely the *AverSampleDis* (ASD) and *SulciOrGyri* (SOG) (see Figure 34). The ASD map is generated by computing the average of the first order moment of all profiles about tangent plane for each vertex. Herein, the first order moment of profile is computed as follow,

$$F_{profile} = \frac{1}{M} \sum_{i=1}^{M} y_i \tag{1}$$

where $M$ is the maximum number of points, $y_i$ is the distance of each profile sampling point to the tangent plane. For the SOG map, that was originally proposed to distinguish sulci from gyri Li et al. (2010), a vertex with more profile points above its tangent plane will be considered as a sulcus vertex, and otherwise as a gyrus vertex. Therefore the SOG map is a binary maps with "sulci" points (0) and "gyri" points (1). As we can see from the Figure 34, these two geometrical maps, ASD and SOG, capture the properties we are interested in and clearly display the presence of wall pinches.

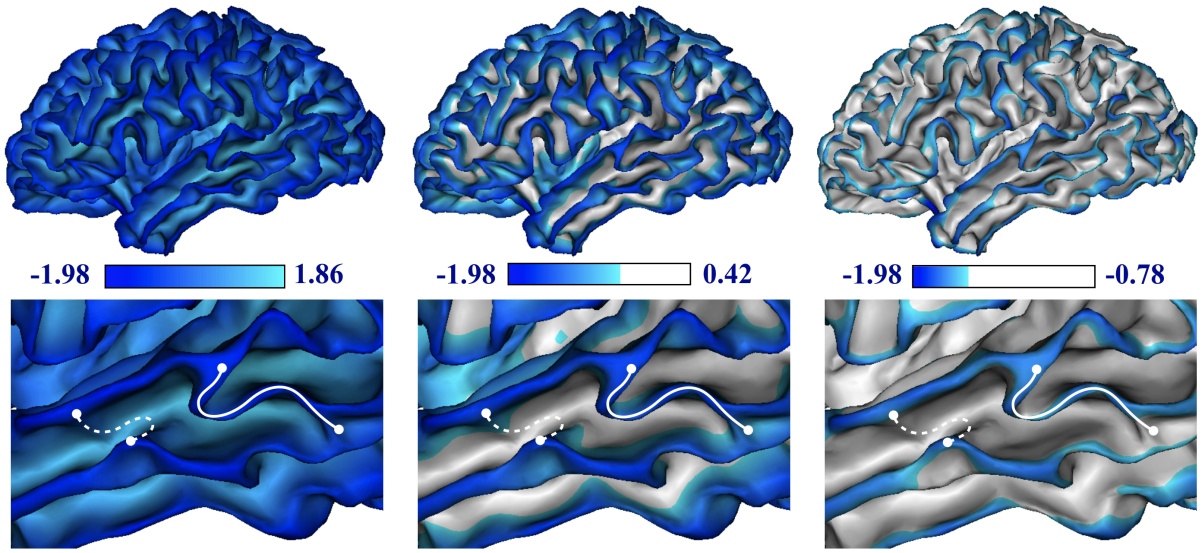


(a) The DPF maps with three different thresholds

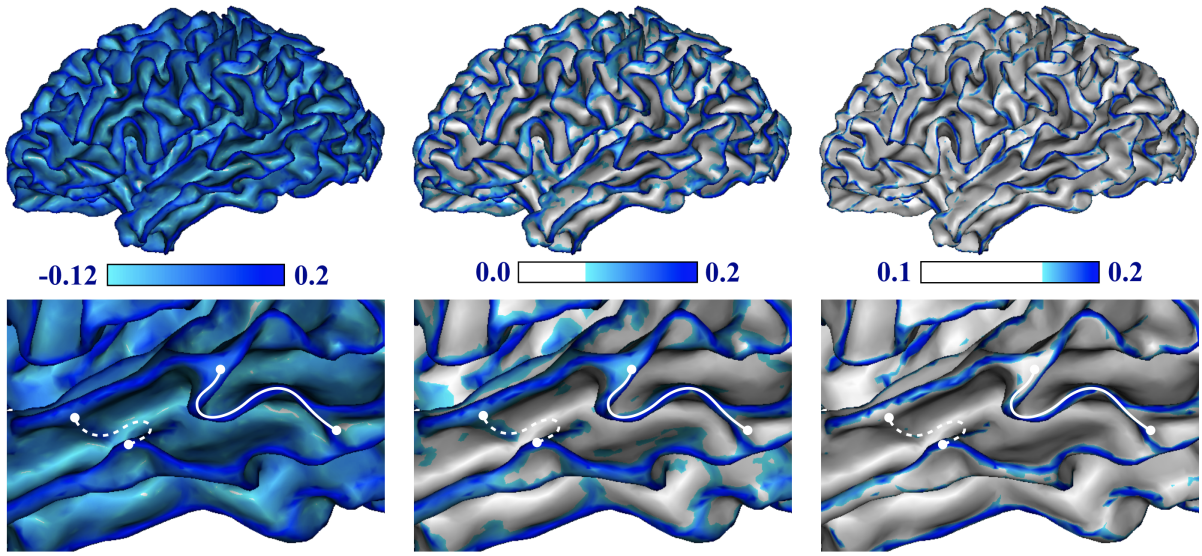


(b) The curvature maps with three different thresholds

Figure 33: The anatomical maps with various thresholds. For a better visualization, we used the "Green-Blue Fusion" palette in Anatomist visualization software (Le Troter et al., 2011). For both (a) and (b), the top figures give the anatomical maps of the whole hemisphere, while the bottom show a local area of STS with a superficial PP (represented by white solid line) and a deep PP (white dotted line). (a) Results of DPF maps. Herein, the DPF minima (in blue) corresponds to the gyri, while the maxima corresponds to sulci. In this example, the left shows the map with initial DPF while the middle shows the suggested DPF threshold (0.42) in (Le Guen et al., 2018; Bodin et al., 2021) and the right DPF is set to the mean of DPF minma and 0.42. The lower the maxima, the less gyri crests are covered in blue. (b) Results of curvature maps. The regions with positive curvature value correspond to the gyri crests or wall pinches. From left to right, the curvature values of lower bounds are selected as the initial minima, 0.0 and 0.1. The higher the lower bound, the less regions are covered in blue.

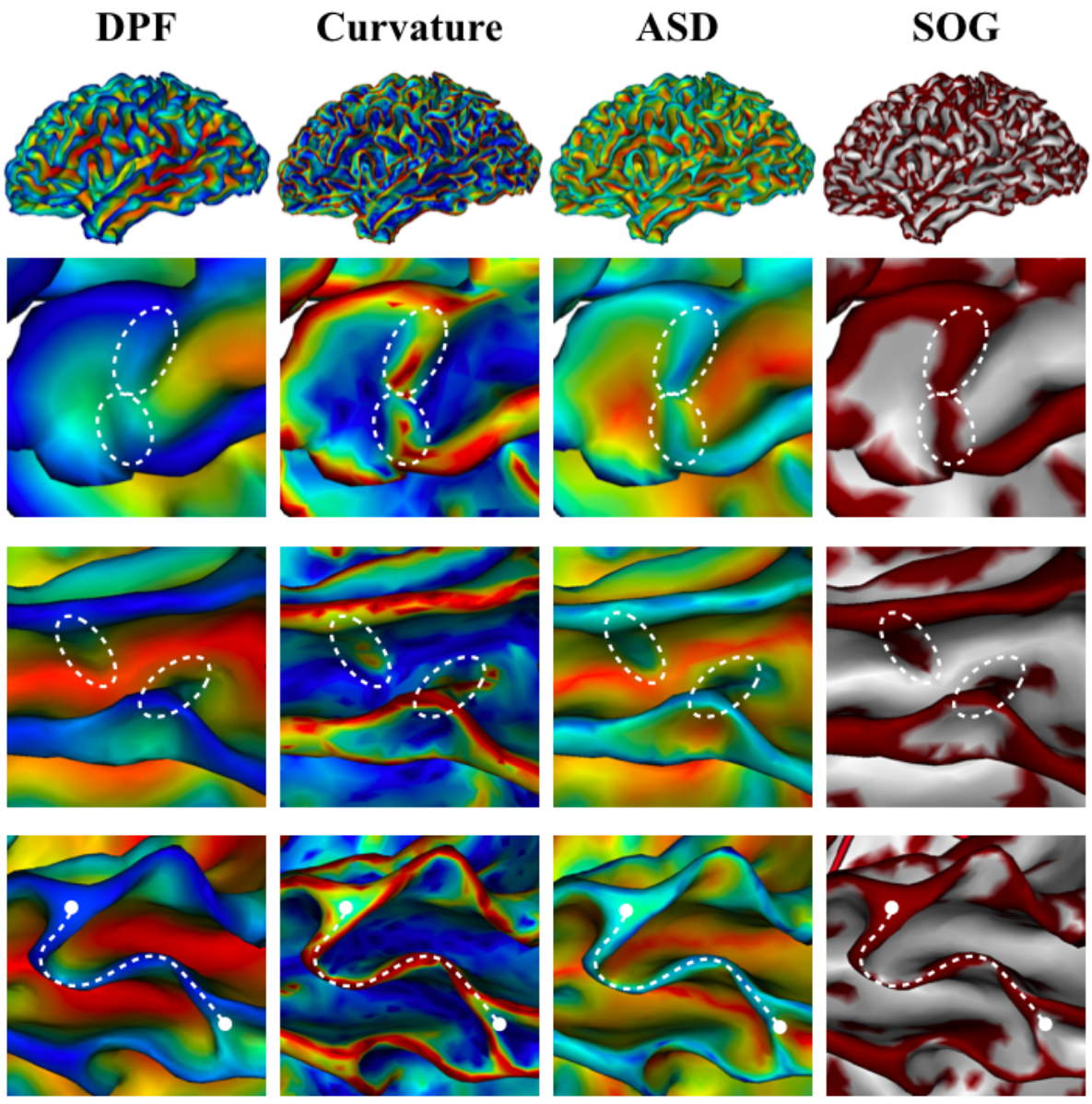


Figure 34: The comparison of different feature maps. All the feature maps are shown without any limit of threshold. The DPF and curvature maps were used in (Le Guen et al., 2018; Bodin et al., 2021). The ASD and SOG maps were in (Li et al., 2010). In the pictures in the second and third rows, the dotted ellipses mark the WPs for the identification of PPs. In the last row, the dotted curve label a superficial PPs. Clearly, the ASD and SOG maps can better differentiate the WPs than the other two maps.

### 3.4.3 Feature images

After building the geometrical maps ASD and SOG, we now extract local feature of interest for each vertex on the fundus of the STS. An illustration of the method is shown in Figure 35 with an ASD map. The method is as follow: we first compute the geometrical map (ASD or SOG) on the mesh of an hemisphere (see Figure 35 (a)). For each vertex on the STS fundus, we then use a new cortical surface profiling process to build a feature vector: values around the vertex are sampled using surface profiling in a disk of radius $r = 13.5mm$ with sampling parameters $\theta = 5°$, $s = 0.3$, and $M = 45$ (see Figure 35 (b)). The disk is aligned such that angle 0° corresponds to the direction of the fundus in the antero-posterior direction, which normalizes the orientation of the features across locations and subjects. The profiling results in a circular feature map (with ASD or SOG values) that is then transformed into a rectangular feature image as shown in (Figure 35 (c)). This feature image therefore captures the geometry of the surrounding surface, in particular the potential presence of wall pinches (visible in blue on Figure 35 (c)).

On account of the high sampling density, for any given local surface patches, the number of sampling points is larger than the vertices of cortical surface. Hence, the feature values of each sampling point was interpolated by their barycentric coordinates of cortical surface. After the feature image extraction, each vertex of the STS fundus corresponds to a local feature image. We therefore propose to use these feature images to solve the 3D PP recognition problem as a 2D image supervised classification problem.

## 3.5 Data preprocessing: the imbalanced property of PPs datasets

As we mentioned before, for all points of the STS fundus, those at the intersection with plis-de-passage were labelled "PP" and the rest were labelled "non-PP". On the selected HPC dataset, we got a total of 15703 vertices of STS fundus, where only 865 of them were labelled as PPs, and 14208 were not. The unbalanced ratio is 1 : 16. This is a typically imbalanced dataset, with PP as the minority class, which lead to difficulties as many algorithms perform better on a balanced dataset.

### 3.5.1 Imbalanced datasets

A dataset is imbalanced if the classification categories are not approximately equally represented. Many real-world problems are imbalanced as their datasets are highly skewed, where most of interested cases belong to the smaller class. However, a standard two-class classification method usually hypothesise that the classes to be discriminated should have

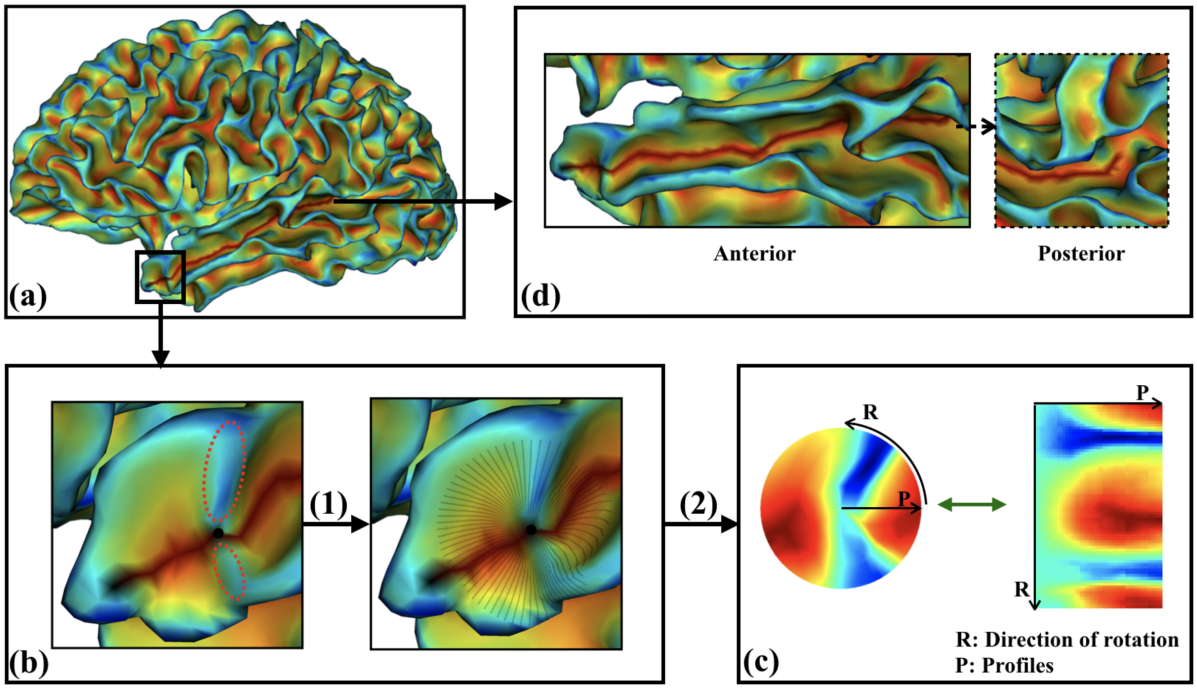


Figure 35: The framework of local feature extraction. (a) Surface with feature map ASD; (b) Surface profiling on a local region. Sampling parameters: $\theta = 5°$, $s = 0.3$, and $M = 45$; (c) Feature images; These two feature images contain the same geometrical information, while the disk feature image shows better visualization of wall pinches. (d) STS fundus (dark red). Steps: (1) Cortical surface profiling; (2) Generate feature images.

a comparable number of instances. In accordance, most current classification systems are designed to optimize the overall performance rather than considering the relative distribution of each class (Chawla, 2009; Liu et al., 2011). As more application of the machine learning methods to the real world problem, the issue with imbalance became more pronounced. Notice that an imbalanced data does not absolutely mean that the learning task suffer from class-imbalance. If the majority class is more important than the minority class, it is not a problem for the majority class dominating the learning. The class-imbalance learning is needed only when the minority class is more important and cannot be sacrificed (Zhou, 2019). We always assumed that the minority class has higher cost than the majority. Examples of applications with such datasets include searching for oil spills in satellite radar images (Kubat et al., 1998), telephone fraud detection (Fawcett and Provost, 1997), credit card fraudulent detection (Chan and Stolfo, 1998; Chen et al., 2009), diagnosis of weld flaws (Liao, 2008), and text categorization (Dumais et al., 1998; Ertekin et al., 2007; Stamatatos, 2008). A number of solutions to the imbalance problem were previously proposed both at the data and algorithmic levels(Chawla et al., 2004). In this part, we mainly focused on the data preprocessing methods. The algorithm based approaches will be discussed in later section.

At the data level, the sampling strategies including over and under-sampling methodologies have received significant attention to counter the effect of imbalanced datasets (Chen et al., 2004; Guo and Viktor, 2004; Kubat et al., 1997; Ling and Li, 1998; Solberg and Solberg, 1996; Sun et al., 2009; Wilson and Martinez, 2000; Phua et al., 2004; Jo and Japkowicz, 2004). As the sampling strategy simply re-balanced the data at the data preprocessing stage, it can be deployed on top of many existing classification approaches. ALthough good, sampling approaches have their various short-comings. Under-sampling majority instances may discard potential important informations against the negative class, while over-sampling positive class by forcing the classifier deliberately to learn from redundant duplicates would induce a problem of overfitting. Various studies in imbalanced datasets have used different variants of over and under sampling, and have presented sometimes conflicting viewpoints on usefulness of oversampling versus undersampling (Chawla, 2003; Maloof, 2003; Drummond et al., 2003; Batista et al., 2004). However, there has been progress in both under and over sampling methods. Meanwhile, many studies considered a combination of the two sampling approaches (Ling and Li, 1998; Japkowicz, 2000; Batista et al., 2004; Liu et al., 2011).

### 3.5.2 Sampling strategy

#### SMOTE

Back to our PPs classification task, it is clear that we need an over-sampling or augmentation strategy to increase the PPs instances. A well-known and widely used oversampling method is SMOTE (Synthetic Minority Oversampling TEchnique) proposed by Chawla et al. (2002). The algorithm starts with searching for the K-nearest neighbors for the minority class sample. Depending upon the amount of over-sampling required, neighbors from the $k$ nearest neighbors are randomly chosen. Then, for each neighbor, it randomly selects a point from the line connecting the neighbor and the instance itself. Finally, this data point is included as a new minority instance (Chawla et al., 2002). By adding the "new" minority instances into training data, it is expected that the over-fitting problem can be alleviated. Many imbalanced class studies using SMOTE achieved favorable results have be reported (Chawla et al., 2002, 2003).

An example is illustrated in Figure 36. For a sample $x_i$ (in blue), the 3-nearest neighbors are included in the light blue circle. Then, one of these nearest neighbors $x_{zi}$ is selected and the new sample is generated by computing the interpolation as follow:

$$x_{new} = x_i + \lambda \times (x_{zi} - x_i) \tag{2}$$

where $\lambda$ is a random number in the range $[0, 1]$. A pseudo-code for SMOTE is presented in Algorithm 1. Some feature disks of generated new PPs instances are shown in Figure 37.

#### Morphological augmentation strategy

Although many studies have shown the good results of SMOTE without over-fitting problem, one major advantage of our PPs study can lead to more confused results when generating new samples by SMOTE. Herein we only divided the points of STS fundus into two categories (PP and non-PP) rather than three categories (superficial PP, deep PP and non-PP) because of the similar characteristics of WPs between superficial and deep PP. This similarity not only gives an explanation for the links between superficial and deep PPs (Bodin et al., 2021), but also generalize the identification of PPs. However, the slightly differences between superficial and deep PPs may create unreliable samples when using the SMOTE.

In addition of the artificially over-sampling methods, such as SMOTE, we also proposed to augment the PPs instances by considering their nearest neighbours. If a point is a PP, then its two nearest neighbours on the STS fundus also can be considered as PPs since their surrounding cortical geometry is similar (see Figure 38 (a), (b)). More generally, we can

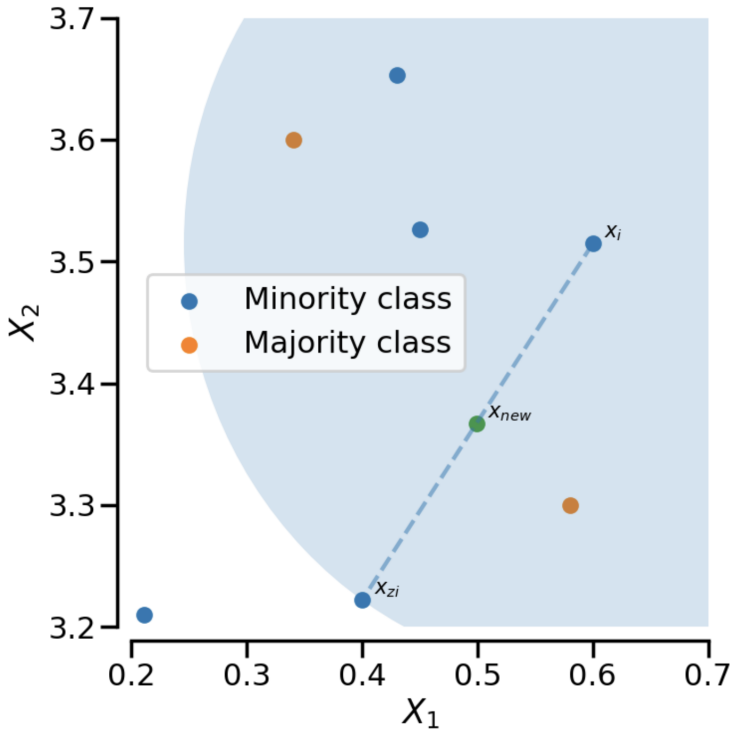


Figure 36: Illustration of new instance generated by SMOTE. Figures adapted from (Lemaître et al., 2017).

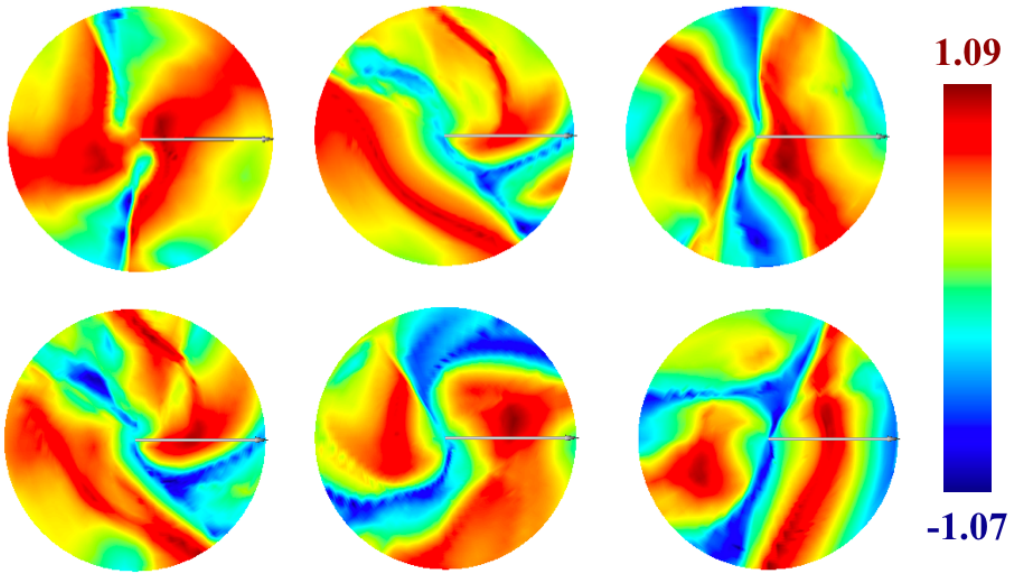


Figure 37: New feature disk generated by SMOTE. 10-nearest neighbors was selected to generate the new PPs feature disks. The wall pinches were visible in blue.

consider the $K$ nearest neighbours as PPs, provided a certain threshold of similarity. Here we consider only $K = 2$.

Unlike the SMOTE, this augmentation strategy will not lead to the over-fitting problem as we directly used the morphological characteristics. Also it increases the number of PPs instances while reducing the number of Non-PPs. Furthermore, we initially selected the intersection vertices between the STS fundus and manual labeled PPs lines as the PPs' vertices in order to facilitate the analysis of PPs, however, the definition of PPs as a small area (called "PPs region") around the vertex instead of a single point provided more PPs instances and benefits for their detection. In order to compare two different augmentation methods, we built two new PPs class with the same size. One used the morphological strategy to augmented the PPs and the other used SMOTE to generate a PPs class of same size.

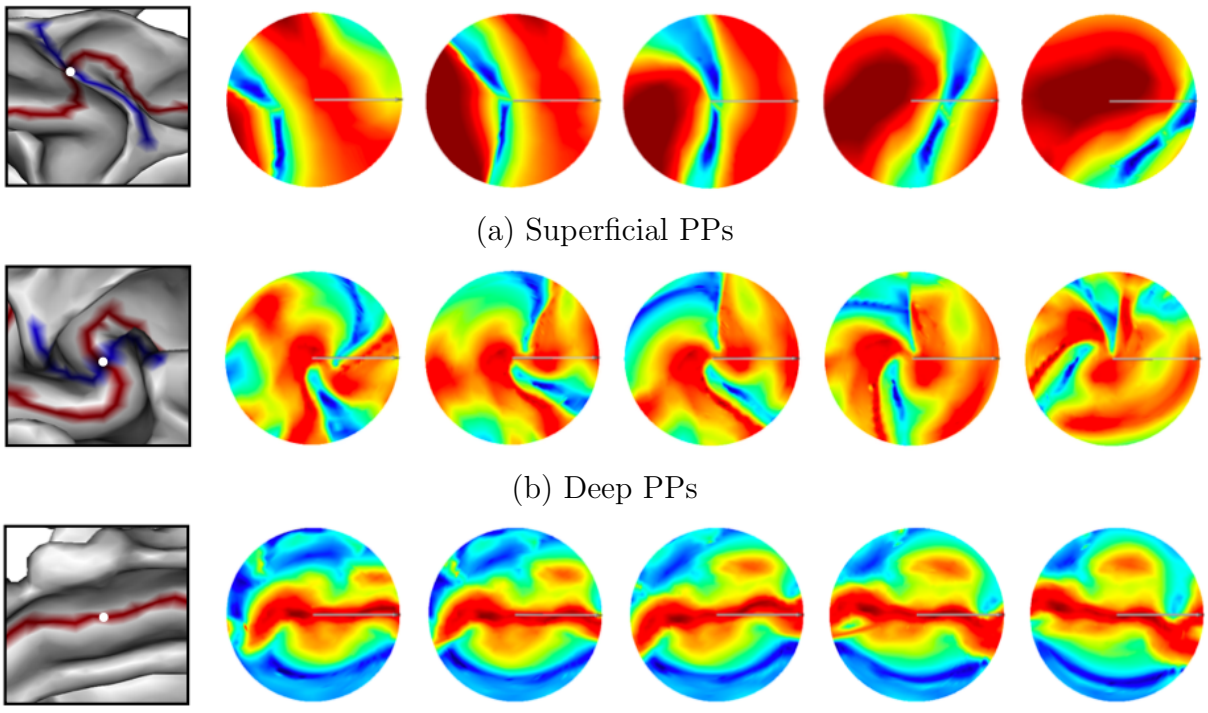

(a) Superficial PPs

(b) Deep PPs

(c) Non-PPs

Figure 38: Feature images of neighbouring vertices on STS fundus. The white points are corresponding to the middle feature images, and the arrows show the direction from anterior to posterior part of STS fundus.

### Under-sampling and balanced dataset

Besides of the PPs, the similarity between non-PPs vertices also provides a support for the under-sampling process in non-PPs data (see Figure 38 (c)). Hence, the non-PPs class

is under-sampled by randomly choosing the samples from it until the new one has the same number of samples with the augmented PPs class. As we considered the two nearest neighbours of PPs as PPs, it should be noted that all the augmented PPs data were not taken into account in the under-sampling process. Combine the two over-sampled PPs datasets and the under-sampled non-PPs dataset respectively, we got two balanced datasets used for training machine learning models. In the balanced dataset, we have a total of 4462 feature images which contains 2231 PPs samples and 2231 non-PPs samples.

**Algorithm 1:** SMOTE(T, N, k)

**Input:** Number of minority class samples $T$; Amount of SMOTE $N\%$; Number of nearest neighbors $k$

**Output:** $(N/100) * T$ synthetic minority class samples

(* *If $N$ is less than 100%, randomize the minority class samples as only a random percent of them will be SMOTEd**);
**if** $N < 100$ **then**
    Randomize the $T$ minority class samples;
    $T = (N/100) * T$;
    $N = 100$
**end**
$N = (int)(N/100)$ (* *The amount of SMOTE is assumed to be in integral multiples of 100.**);
$k$ = Number of nearest neighbors;
$numattrs$ = Number of attributes;
$Sample[][]$ : array for original minority class samples;
$newindex$ : keeps a count of number of synthetic samples generated, initialized to 0;
$Synthetic[][]$ : array for synthetic samples;
(* Compute $k$ nearest neighbors for each minority class sample only. *);
**for** $i \leftarrow 1$ **to** $T$ **do**
    Compute $k$ nearest neighbors for $i$, and save the indices in the $nnarray$;
    Populate $(N, i, nnarray)$
**end**
**while** $N \neq 0$ **do**
    Choose a random number between 1 and $k$, call it $nn$. This step chooses one of the $k$ nearest neighbors of $i$;
    **for** $attr \leftarrow 1$ **to** $numattrs$ **do**
        Compute: $dif = Sample[nnarray[nn]][attr] - Sample[i][attr]$;
        Compute: $gap$ =random number between 0 and 1;
        $Synthetic[newindex][attr] = Sample[i][attr] + gap * dif$
    **end**
    $newindex++$;
    $N = N + 1$
**end**
**return** (* *End of Populate.* *)

## 3.6 Machine learning methods

After the feature image extraction, the 3D morphological characteristics were recorded in the 2D feature images. The detection of PPs problem is converted to a binary supervised classification task of 2D feature images. To deal with our imbalanced PPs dataset, we investigated and combined two over-sampling and one under-sampling strategies to build a balanced dataset.

In this section, we will test two machine learning algorithms used for PPs classification and discuss their prediction results based on the following issues:

1. Impact of imbalanced dataset;
2. Impact of different feature maps (DPF, curvature, SOG, ASD);
3. Comparison of two over-sampling strategies;

### 3.6.1 Algorithms

#### K-nearest neighbors

The k-nearest neighbors algorithm ($k$-NN) is a non-parametric supervised classification method first developed by Evelyn Fix and Joseph Hodges in 1951 (Fix and Hodges, 1989) and later expanded by Thomas Cover (Altman, 1992). The $k$-NN algorithm relies on the principle that similar objects in the input space are also similar in the output space (Zhou, 2019). Hence, it is considered as a lazy learning approach since it does not have an explicit training process but simply stores the training dataset instead. For classification, a simple $k$-NN learner identifies the k instances closest to the test instance from the training data, and then classifies the test instance to the majority class among the k instances.

As a variant of the basic $k$-NN, a weighted $k$-NN algorithm was proposed and successfully used in the local pattern recognition of magnetic resonance imaging (Coupé et al., 2011; Rousseau et al., 2011). This weighted $k$-NN algorithm assigned a weight that measures the similarity to the test instances for all selected nearest neighbors. In more details, for a input instance $i$, let $L_i$ as the prediction label, so we have

$$L_i = \frac{\sum\limits_{j \in I_k} s_{i,j} L_j}{\sum\limits_{j \in I_k} s_{i,j}} \tag{3}$$

where $s_{i,j}$ is the similarity between input instance $i$ and selected instance $j$, and $L_j$ is the manual label of $j$. Consider that the labels $L$ belong to $\{0, 1\}$, the $L_i$ was rounded by

$$L_i = \begin{cases} 1 & L_i \geq 0.5 \\ 0 & L_i < 0.5 \end{cases} \tag{4}$$

### Distance metrics

When doing classification using $k$-NN, it is often necessary to estimate the similarity between two samples (similarity measurement), which often uses the "distance" between the two samples, and what method is used to calculate the distance is very delicate, and even related to the correct classification or not. In this part, we introduce some distance used in our study.

**Structural SIMilarity (SSIM)**

The structural similarity is a well-known measurement in the image quality assessment and it also can be used to estimate the similarity of images (Wang et al., 2004; Coupé et al., 2011).

Given two images (or vectors) $\mathbf{x}$ and $\mathbf{y}$, we have

$$SSIM(\mathbf{x}, \mathbf{y}) = [l(\mathbf{x}, \mathbf{y})]^{\alpha}[c(\mathbf{x}, \mathbf{y})]^{\beta}[s(\mathbf{x}, \mathbf{y})]^{\gamma} \tag{5}$$

where $\alpha, \beta, \gamma > 0$, and

$$l(\mathbf{x}, \mathbf{y}) = \frac{2\mu_x\mu_y + c_1}{\mu_x^2 + \mu_y^2 + c_1} \tag{6}$$

$$c(\mathbf{x}, \mathbf{y}) = \frac{2\sigma_{xy} + c_2}{\sigma_x^2 + \sigma_y^2 + c_2} \tag{7}$$

$$s(\mathbf{x}, \mathbf{y}) = \frac{\sigma_{xy} + c_3}{\sigma_x\sigma_y + c_3} \tag{8}$$

$l(\mathbf{x}, \mathbf{y})$ is the luminance comparison, where $\mu_x, \mu_y$ are the mean values of $x, y$ respectively. $c(\mathbf{x}, \mathbf{y})$ is the contrast comparison and $s(\mathbf{x}, \mathbf{y})$ is the structural comparison, where $\sigma_x, \sigma_y$ are the stand deviation respectively and $\sigma_{xy}$ is the co-variance of $x$ and $y$. $c_1, c_2, c_3$ are constant used to avoid the errors when the denominator is very close to zero. In practice, we set $\alpha = \beta = \gamma = 1$ and $c_3 = c_2/2$, so the $SSIM$ can be simplified as follow,

$$SSIM(\mathbf{x}, \mathbf{y}) = \frac{(2\mu_x\mu_y + c_1)(\sigma_{xy} + c_2)}{(\mu_x^2 + \mu_y^2 + c_1)(\sigma_x^2 + \sigma_y^2 + c_2)} \tag{9}$$

Furthermore, the equation (9) is usually used to compare two windows of images instead of the entire, so we compute the mean SSIM (MSSIM) to compare the whole images:

$$MSSIM(\mathbf{x}, \mathbf{y}) = \frac{1}{M} \sum_{j=1}^{M} SSIM\left(\mathbf{x}_j, \mathbf{y}_j\right) \tag{10}$$

where $\mathbf{x}_j$ and $\mathbf{y}_j$ are the image contents at the $j$-th window and $M$ is the number of windows in the image.

The SSIM value can vary between -1 and 1, where 1 indicates perfect similarity. This method has been implemented in scikit-image (van der Walt et al., 2014).

**Cosine similarity and mean squared error**

Besides, we also use two common similarity measures, cosine similarity and mean squared error (MSE), as a comparison. Given two vectors $\mathbf{x}$ and $\mathbf{y}$, the cosine similarity is represented using a dot product and magnitude as

$$\cos\left(\mathbf{x}, \mathbf{y}\right) = \frac{\mathbf{x} \cdot \mathbf{y}}{\|\mathbf{x}\| \|\mathbf{y}\|} = \frac{\sum_{i=1}^{n} x_i y_i}{\sqrt{\sum_{i=1}^{n} x_i^2} \sqrt{\sum_{i=1}^{n} y_i^2}} \tag{11}$$

where $x_i$ and $y_i$ are components of vector $\mathbf{x}$ and $\mathbf{y}$ respectively. Suppose the image size is $m \times n$, the MSE is computed as

$$MSE = \frac{1}{mn} \sum_{i=0}^{m-1} \sum_{j=0}^{n-1} [\mathbf{x}(i,j) - \mathbf{y}(i,j)]^2 \tag{12}$$

where $\mathbf{x}(i,j)$ and $\mathbf{y}(i,j)$ represent the value of the pixel $(i,j)$. The MSE computes the strict differences between two corresponding pixels in location, so a value of 0 for MSE means perfect similarity.

### Support Vector Machine

Support Vector Machines (SVMs, also support-vector networks (Cortes and Vapnik, 1995)) are supervised learning models with associated learning algorithms that analyze data used for classification and regression analyse. SVM is firstly designed for binary classification tasks. Given a training dataset of instance-label pairs $(\mathbf{x}_i, y_i), i = 1, \ldots, l$ where $\mathbf{x}_i \in R^n$ and $y \in \{1, -1\}^l$, the SVM require the solution of the following optimization problem:

$$\begin{aligned} \min_{\mathbf{w}, b, \boldsymbol{\xi}} \quad & \tfrac{1}{2}\mathbf{w}^T\mathbf{w} + C \sum_{i=1}^{l} \xi_i \\ \text{subject to} \quad & y_i \left(\mathbf{w}^T \phi\left(\mathbf{x}_i\right) + b\right) \geq 1 - \xi_i \\ & \xi_i \geq 0 \end{aligned} \tag{13}$$

where $\phi(\mathbf{x}_i)$ maps $\mathbf{x}_i$ into a higher-dimensional space and $C > 0$ is the penalty parameter of the error term. Due to the possible high dimensionality of vector variable $w$, the dual problem was usually solved

$$\begin{aligned} \min_{\boldsymbol{\alpha}} \quad & \tfrac{1}{2}\boldsymbol{\alpha}^T Q \boldsymbol{\alpha} - \boldsymbol{e}^T \boldsymbol{\alpha} \\ \text{subject to} \quad & \boldsymbol{y}^T \boldsymbol{\alpha} = 0 \\ & 0 \le \alpha_i \le C, \quad i = 1, \ldots, l \end{aligned} \tag{14}$$

where $e = [1, \ldots, 1]^T$ is the vector of all ones, $Q$ is an $l$ by $l$ positive semidefinite matrix, $Q_{ij} \equiv y_i y_j K(\boldsymbol{x}_i, \boldsymbol{x}_j)$, and $K(\mathbf{x}_i, \mathbf{x}_j) \equiv \phi(\mathbf{x}_i)^T \phi(\mathbf{x}_j)$ is called the kernel function.

After problem (14) is solved, using the primal-dual relationship, the optimal $\mathbf{w}$ satisfies

$$\mathbf{w} = \sum_{i=1}^{l} y_i \alpha_i \phi(\mathbf{x}_i) \tag{15}$$

and the decision function is

$$\operatorname{sgn}\left(\mathbf{w}^T \phi(\boldsymbol{x}) + b\right) = \operatorname{sgn}\left(\sum_{i=1}^{l} y_i \alpha_i K(\boldsymbol{x}_i, \boldsymbol{x}) + b\right) \tag{16}$$

Different kernel functions allow the SVM to fit various data, hence a proper selection of kernel function can improve the performance of SVM. However, it's not easy to choose or devise a proper function for a specific problem. There are four basic kernels:

- linear: $K(\mathbf{x}_i, \mathbf{x}_j) = \mathbf{x}_i^T \mathbf{x}_j$.
- polynomial: $K(\mathbf{x}_i, \mathbf{x}_j) = \left(\gamma \mathbf{x}_i^T \mathbf{x}_j + r\right)^d, \gamma > 0$.
- Gaussian radial basis function (RBF): $K(\mathbf{x}_i, \mathbf{x}_j) = \exp\left(-\gamma \left\|\mathbf{x}_i - \mathbf{x}_j\right\|^2\right), \gamma > 0$.
- sigmoid: $K(\mathbf{x}_i, \mathbf{x}_j) = \tanh\left(\gamma \mathbf{x}_i^T \mathbf{x}_j + r\right)$.

Here, $\gamma$, $r$ and $d$ are kernel parameters. The degree $d$ is specified for polynomial kernel and $r$ is usually set to zero.

For all parameters mentioned above, the $C$ parameter trades off correct classification of training examples against maximization of the decision function's margin. For larger values of $C$, a smaller margin will be accepted if the decision function is better at classifying all training points correctly. A lower $C$ will encourage a larger margin, therefore a simpler decision function, at the cost of training accuracy. Intuitively, the $\gamma$ parameter defines how far the influence of a single training example reaches, with low values meaning far and high

values meaning close. The $\gamma$ parameters can be seen as the inverse of the radius of influence of samples selected by the model as support vectors.

In SVM, the support vectors are important to the training set. Theoretically, the support vectors lie closest to the decision boundary and form the margin between two sides. Moreover, if we removed all other training data and repeated the training process, we could get the same separating hyperplane. This fact gives us the advantage of classifying by learning with only a small number of support vectors, as all we need to know is the position of the decision boundary and other training data can be considered redundant. In addition, it is most significant in the imbalanced problem, as the SVMs can be less affected by the large number of negative instances far from the decision boundary (Liu et al., 2011).

### 3.6.2 Experiments and results

#### Data

In order to investigate strategies for imbalanced data, we used the following datasets

1. Balanced datasets generated by SMOTE with feature map ASD;
2. Balanced datasets generated by morphological strategy with feature maps ASD, SOG, DPF and curvature;
3. Imbalanced dataset with feature map ASD.

The original imbalanced dataset contains 15703 feature images, with 865 PPs and 14208 non-PPs. As mentioned for the morphological over-sampling strategy, we considered the two nearest neighbors of PP vertices also as PPs, leading to a total of 2231 PP samples. Herein, the number of augmented PPs is not exactly twice as much as the manually labeled PPs because some neighboring vertices overlapped on the STS fundus. To compare two over-sampling strategy, we used the SMOTE to generate the same number of PPs as the morphological one. Therefore, both two balanced datasets contain 4462 feature images with 2231 PPs and 2231 non-PPs instances. Here we named the balanced datasets generated by SMOTE as the SMOTE dataset, and the morphological strategy datasets as MorS dataset.

In this section, we randomly selected 500 instances as TEST data and the rest data used to train the machine learning models. Hence, the data was divided as follow:

1. Test dataset: 500 images with 250 PPs and 250 non-PPs;
2. Balanced training dataset: 3962 images with 1981 PPs and 1981 non-PPs;
3. Imbalanced training dataset: 12565 images with 1981 PPs and 10484 non-PPs.

### Base level models and experiments

**$k$-NN:** We implemented the weighted $k$-NN in Python. The SSIM was computed with the scikit-image package (van der Walt et al., 2014). The cosine similarity and MSE were computed with the scikit-learn package (Pedregosa et al., 2011). The best parameter $k$ was tested on $k = 5, 10, 15, 20, 25, 30, 35$ by training models on balanced datasets of ASD feature maps.

Besides, we compared the feature images with different cortical surface profiling sampling distances $(9mm, 13.5mm, 18mm)$.

**SVM:** We trained the SVM models using the SVM package of scikit-learn, which internally used libsvm (Chang and Lin, 2011) and liblinear (Fan et al., 2008) to handle all computations. Also, the implements of SVM in scikit-learn package provided a probability for each predicted samples. The linear, polynomial and RBF kernels were used and the optimal parameters were selected by a five folds cross-validated grid-search over a parameter grid. For the polynomial kernel, the parameter degree $d$ was selected from $\{2, 3, 4, 5\}$, and $\gamma$ was varied from $10^{-3}$ to 10 by factors of 10. For the RBF kernel, the parameter $C$ was selected from $2^{-5}$ to 8 by factors of 2 and $\gamma$ was from $10^{-9}$ to 1000 by factors of 10.

In our experiments, the SVM with linear, polynomial and RBF kernels were trained on the balanced datasets. Besides, a weighted SVM provided in scikit-learn to deal with the imbalance problem was trained on the imbalanced dataset. In this model, the labels are weighted inversely proportional to class frequencies in the original data. The RBF kernel of default parameter settings in scikit-learn were selected for this model.

### Evaluation measures

In machine learning, evaluation measures are based on the $ConfusionMatrix$, a two-class problem confusion matrix with positive and negative values is illustrated in Table 1

Table 1: Prediction results with different training datasets

| | Ground-truth Positive | Ground-truth Negative |
|---|---|---|
| Predicted Positive | TP (True Positive) | FP (False Positive) |
| Predicted Negative | FN (False Negative) | TN (True Negative) |

To evaluate the model performance, we computed the accuracy of entire data, PPs data and non-PPs data. For the overall accuracy, we have:

$$ACC = \frac{TP + TN}{TP + TN + FP + FN} \tag{17}$$

For PPs data,

$$ACC_{pp} = \frac{TP}{TP + FN} \tag{18}$$

and non-PPs,

$$ACC_{non-pp} = \frac{TN}{TN + FP} \tag{19}$$

In particular, we also computed the accuracy of PPs across different ranges of depth. Here the depth is assigned for the intersected points between PPs lines and STS fundus. This measure allows us to study the detection performances as a function of depth, to see how algorithms perform on superficial or deep PPs.

### Results and analyses

#### $k$-NN

**Surface profile sampling size and similarity measures:** The radius of profile sampling is related to the size of the feature images. The feature images generated with a larger sampling radius capture larger cortical surface areas, again containing more geometrical information and noise. Before training the machine learning models, we first tested the influences of various sampling radii, and compared the various similarities measures.

Table 2 - 4 shows the prediction results on the feature images whose profiling radius are $9mm$, $13.5mm$, $18mm$ respectively and the best results are bold. Here we used the 10-NN models. As we can see from these tables, the SSIM performs well on the $9mm$ and $13.5mm$ dataset and worst on the $18mm$ dataset. Then the cosine similarity also gets good results that are close to the SSIM, while performing better than SSIM on the $9mm$ dataset. All models using MSE performs worst. However, these three sampling distances do not result in a change in the accuracy, where the accuracy of SSIM is around 75%, the Cosine similarity is from 72.3% to 76%. Obviously, compared to the other two similarities, the models using SSIM have the most consistent performance to the sampling distance. Thus, we chose the SSIM as the similarity measures of $k$-NN models. Among these models using SSIM, we chose the profile sampling radius as $13.5mm$ to generate the feature images.

**Optimal $k$:** To facilitate comparison of other issues, we selected the optimal $k$ of weighted $k$-NN models. The best choice of $k$ depends upon the data, generally larger values of $k$ reduce effect of the noise on the classification (Everitt et al., 2011). Herein, we used the feature images built by ASD feature maps and selected the SSIM as the similarity measure to training the models. Table 5 gives the accuracy of models with different $k$ from

Table 2: The accuracy of 10-NN method (9mm)

| Similarity | Entire data(%) | PPs data (%) | Non-PPs data (%) |
|---|---|---|---|
| SSIM | 75 | **70.8** | 79.2 |
| Cosine | **76** | 68 | **84** |
| MSE | 72.6 | 69.6 | 75.6 |

Table 3: The accuracy of 10-NN method (13.5 mm)

| Similarity | Entire data (%) | PPs data(%) | Non-PPs data(%) |
|---|---|---|---|
| SSIM | **75.4** | **70.8** | **80.0** |
| Cosine | 73 | 69.6 | 76.4 |
| MSE | 66.4 | 61.6 | 71.2 |

Table 4: The accuracy of 10-NN method (18mm)

| Similarity | Entire data(%) | PPs data(%) | Non-PPs data(%) |
|---|---|---|---|
| SSIM | **74.4** | 70.4 | **78.4** |
| Cosine | 72.4 | **70.8** | 74 |
| MSE | 66 | 57.2 | 74.8 |

5 to 35. Among these $k$ values, the prediction accuracy reaches a local maximum at $k = 10$ and $k = 25$ both in the entire and PPs dataset, and the model with $k = 10$ performs best in PPs cases. Then, we compared the accuracy of PP detection across different depth ranges using 10-NN and 25-NN models. As shown in Table 6, the model with $k = 10$ performed better on most deep PPs, instead the model with $k = 25$ gets better on superficial PPs. Since deep PPs are more difficult to detect than superficial ones, we selected the $k = 10$ as the benchmark used for training weighted $k$-NN models.

Table 5: The accuracy of different selected $k$ (SSIM, $r = 13.5mm$)

| k values | Entire data (%) | PPs data (%) | Non-PPs data(%) |
|---|---|---|---|
| 5 | 71.6 | 58.8 | **84.4** |
| 10 | 75.2 | **70.4** | 80 |
| 15 | 73.8 | 65.9 | 81.6 |
| 20 | 73.8 | 66.4 | 81.2 |
| 25 | **76** | 69.2 | 82.8 |
| 30 | 75.8 | 68.4 | 83.2 |
| 35 | 75.4 | 67.2 | 83.6 |

Table 6: The accuracy of PPs in different depth ranges (%)

| k values | $d \in [0, 5]$ | $d \in (5, 10]$ | $d \in (10, 15]$ | $d \in (15, 20]$ | $d \in (20, +\infty]$ |
|---|---|---|---|---|---|
| 10 | 87.5 | 83.3 | **70.8** | **56.8** | **67.4** |
| 25 | **91.7** | **86.7** | 60.4 | **56.8** | 65.1 |

**Feature maps:** We trained weighted 10-NN models on the feature images of four

different feature maps (ASD, SOG, DPF and Curvature) using the SSIM similarity measure. In the following, curvature is abbreviated to "CURV". Table 7, 8 show the results. Clearly the models using DPF and curvature maps only predict few PPs, while the models with ASD maps performed best. This is consistent with the fact that it is difficult to visually identify wall pinches using DPF and curvature maps without any threshold.

Table 7: Prediction results with different feature maps

| Feature map | Entire data (%) | PPs data (%) | Non-PPs data(%) |
|---|---|---|---|
| ASD | **75.2** | 70.4 | 80 |
| SOG | 67.6 | **70.8** | 64.4 |
| DPF | 52.8 | 6.0 | **99.6** |
| CURV | 53.8 | 8.8 | 98.8 |

Table 8: The accuracy of PP detection in different depth ranges (%)

| Feature map | $d \in [0, 5]$ | $d \in (5, 10]$ | $d \in (10, 15]$ | $d \in (15, 20]$ | $d \in (20, +\infty]$ |
|---|---|---|---|---|---|
| ASD | **87.5** | **83.3** | 70.8 | 56.8 | **67.4** |
| SOG | 85.4 | 73.3 | **75** | **65.4** | 58.1 |
| DPF | 8.3 | 16.7 | 6.3 | 2.5 | 2.3 |
| CURV | 25.0 | 6.7 | 6.3 | 4.9 | 2.3 |

**Imbalanced, SMOTE and morphological balanced data:** We trained weighted 10-NN models on the three different datasets using the ASD feature maps and SSIM similarity measure. Here the sampling radius of each feature image is $13.5mm$. Table 9, 10 show the results. As we can see, the weighted $k$-NN model failed to predict the PPs on the imbalanced data, which means there are more non-PPs samples than PPs in the 10 nearest neighbors in the imbalanced data. This result is understandable considering the ratio of PPs: non-PPs $\approx 1 : 16$. Besides, we got a better prediction results on the balanced dataset generated using the morphological strategy (MorS) than SMOTE. Both strategies lead to a better detection of superficial PPs but the MorS strategy is consistently better at all depths.

### SVM

For comparison with the weighted $k$-NN models, we used the same data to train the SVMs. The SVMs with optimal parameters and their prediction results were shown in Table 11, 12. As in $k$-NN, the weighted SVM was trained on the imbalanced dataset. As can be seen from the tables, the best prediction result of SVM is better than the $k$-NN. Among various SVMs, it can be seen that the SVM trained on the balanced dataset using MorS performs better than imbalanced dataset and SMOTE dataset, and this is consistent with the results of $k$-NN models. However, the SVM trained on the SMOTE dataset failed to predict the

Table 9: Prediction results with different training datasets

| Training data | Entire data (%) | PPs data (%) | Non-PPs data(%) |
|---|---|---|---|
| MorS data | **75.2** | **70.4** | 80 |
| SMOTE data | 60.0 | 60.0 | 60.0 |
| Imbalanced data | 50.0 | 0.0 | **100.0** |

Table 10: The accuracy of PPs in different depth ranges (%)

| Training data | $d \in [0, 5]$ | $d \in (5, 10]$ | $d \in (10, 15]$ | $d \in (15, 20]$ | $d \in (20, +\infty]$ |
|---|---|---|---|---|---|
| MorS data | **87.5** | **83.3** | **70.8** | **56.8** | **67.4** |
| SMOTE data | 79.2 | 70.0 | 54.2 | 54.3 | 48.8 |
| Imbalanced dataset | 0 | 0 | 0 | 0 | 0 |

PPs. This may be caused by the nearest neighbors of PPs, which are very similar to PPs as shown in 38. Unlike MorS, these neighbors are labelled as non-PPs when training ML models on SMOTE data. The SVM using RBF kernels perform better than linear and polynomial kernels.

In comparison of four feature maps, different from $k$-NN models, the DPF and curvature maps show good performances, and in particular the DPF got the best prediction results on this TEST data. Herein, for convenience, we use feature map names to represent the corresponding models. As we can see from Table 12, all the models have good predictions for very superficial PPs whose depth is below $5mm$ and the SOG perform best. The ASD got the best results for the PPs whose depth from 5 to $20mm$, while the DPF performed best for the PPs whose depth more than $10mm$.

We should note that all the results above only show the performances of models on the balanced TEST data designed by a hold-out strategy that splits the data into a training and test set. Although it can be used to compare these models, the results do not exactly reflect the general situation where the ratio of PPs : Non-PPs $\approx 1 : 5$ after augmentation of PPs. Hence, to further compare the SVM models with four feature maps, we trained and tested SVM models with a 5-fold cross-validation. In each fold, the training data is a balanced dataset and the test data has the same distribution of PPs and Non-PPs as the original data. The mean of prediction accuracy results are shown in Table 13, 14. In this cross-validation, the DPF and SOG fail to predict the PPs instances, while the CURV predicts a majority of PPs. Only ASD leads to a good prediction result for all types of data. Notably, the overall accuracy of DPF and SOG is high but the accuracy for PPs data is low, which is common in imbalanced datasets. In fact, it is meaningless to achieve high overall accuracy when the data is highly imbalanced because the prediction results of PPs are more important for us. In addition, we find that the CURV gives better results as the

Table 11: Prediction results of SVM

| SVM | Entire data(%) | PPs data(%) | Non-PPs data(%) |
|---|---|---|---|
| RBF (C=2.0, $\gamma = 0.001$), MorS, ASD | 78.4 | 80.8 | 76 |
| RBF (C=4.0, $\gamma = 0.001$), MorS, SOG | 66.0 | 68.4 | 63.6 |
| RBF (C=4.0, $\gamma = 0.001$), MorS, DPF | **82.4** | **82.8** | 82.0 |
| RBF (C=2.0, $\gamma = 0.001$), MorS, CURV | 78.6 | 80.0 | 77.8 |
| polynomial (degree = 3), MorS, ASD | 74.6 | 66.4 | 82.0 |
| linear, MorS, ASD | 61.2 | 61.6 | 60.8 |
| RBF, weighted SVM, IMB, ASD | 76.8 | 68.4 | **85.2** |
| RBF, SMOTE, ASD | 50.0 | 0.0 | 100.0 |

IMB: imbalanced data.

Table 12: The accuracy of PPs in different depth ranges on SVM (%)

| SVM | $d \in [0, 5]$ | $d \in (5, 10]$ | $d \in (10, 15]$ | $d \in (15, 20]$ | $d \in (20, +\infty]$ |
|---|---|---|---|---|---|
| RBF (C=2.0, $\gamma = 0.001$),$*$, ASD | 91.7 | **86.7** | **81.25** | **79.0** | 70.7 |
| RBF (C=4.0, $\gamma = 0.001$),$*$, SOG | **100** | 76.7 | 68.75 | 53.1 | 55.8 |
| RBF (C=4.0, $\gamma = 0.001$),$*$, DPF | 93.75 | 80.0 | **81.25** | **79.0** | **81.4** |
| RBF (C=2.0, $\gamma = 0.001$),$*$, CURV | 85.4 | 80.0 | **81.25** | 76.5 | 79.1 |
| polynomial (degree = 3),$*$, ASD | 81.3 | 76.7 | 62.5 | 56.8 | 65.1 |
| linear,$*$, ASD | 75.0 | 63.3 | 70.8 | 51.9 | 53.4 |
| RBF, weighted SVM, IMB, ASD | 77.1 | 70 | 66.7 | 69.1 | 58.1 |
| RBF, SMOTE, ASD | 0 | 0 | 0 | 0 | 0 |

IMB: imbalanced data; $*$ : MorS.

depth increases. This is due to the fact that the curvature gets more negative as you get deeper, and the WP stands out more even it show a slightly positive curvature value.

Table 13: Prediction results with different training datasets

| Feature map | Entire data (%) | PPs data (%) | Non-PPs data(%) |
|---|---|---|---|
| ASD | 75.2 | **77.3** | 74.7 |
| DPF | 82.2 | 3.7 | 98.6 |
| SOG | **82.5** | 0.4 | **99.7** |
| CURV | 21.9 | 67.8 | 12.3 |

Table 14: The accuracy of PPs in different depth ranges (%)

| Feature map | $d \in [0, 5]$ | $d \in (5, 10]$ | $d \in (10, 15]$ | $d \in (15, 20]$ | $d \in (20, +\infty]$ |
|---|---|---|---|---|---|
| ASD | **85.7** | **75.8** | **78.3** | 71.6 | 77.4 |
| DPF | 13.7 | 8.6 | 2.8 | 0 | 0 |
| SOG | 1.6 | 1.3 | 0.3 | 0 | 0 |
| CURV | 28.12 | 57.6 | 70.6 | **81.2** | **81.9** |

### 3.6.3 Summary

In this section, we focused on the three issues raised at the beginning. Several machine learning models were trained to help us learn more about the ML models and the effects of imbalanced data. First, among all our experiments, the SVM with RBF kernel using the MorS training dataset got the best result, and the ASD seems to be the optimal feature map. Then, directly training a machine learning model on imbalanced data will fail to classify the minority class, and the over-sampling methods can improve the prediction results by reducing the skew of the data. However, different over-sampling strategies have been tested for our problem, and the well-known SMOTE method performed worse than the morphological strategy we proposed. Concerning the feature maps used to train the machine learning models, we got similar results as described in the section3.4, namely the DPF and curvature maps were not optimal neither for observation nor for training machine learning models. Moreover, the variabilities of DPF and curvature values across different WPs also make their application difficult in general. Here, we only used the general accuracy, the accuracy of PPs and Non-PPs to evaluate performances. Clearly, it is not optimal for evaluating class-imbalance learning. In the next sections, we discuss how to address the imbalanced issue in a more appropriate way. In particular we present evaluation metrics and algorithmic improvements to the classification process, both designed specifically for imbalanced data learning.

## 3.7 Evaluation measures with class-imbalance

The choice of a performance index is critical to evaluate the goodness of a classifier. As we mentioned in previous sections, in machine learning, evaluation measures are based on the $ConfusionMatrix$, a two-class problem confusion matrix with positive and negative values is illustrated in Table 1 Traditionally, the overall performance of machine learning algorithm is usually evaluated with the "accuracy":

$$ACC = \frac{TP + TN}{TP + TN + FP + FN} \tag{20}$$

However, it is often meaningless to achieve high accuracy when the data is highly imbalanced. As the PPs problem in our study, the ratio of PPs : Non-PPs $\approx 1 : 16$, a straightforward method of guessing all instances as Non-PPs would achieve an accuracy 93.75%, though the accuracy seems high, we can not detect any PPs. Therefore a high overall accuracy may mislead the performance of classifiers in the context of imbalanced class problem, moreover, the higher rate of correct detection on the minority class is particular required (Liu et al., 2011; Maratea et al., 2014; Zhou, 2019).

Several common measures can be defined from Confusion Matrix:

- The *Recall* (or true positive) measures the accuracy of positive instances.

$$Recall = \frac{TP}{TP + FN} \tag{21}$$

- The *Precision*

$$Precision = \frac{TP}{TP + FP} \tag{22}$$

- The *Specificity* (or true negative) measures the accuracy of negative instances.

$$Specificity = \frac{TN}{TN + FP} \tag{23}$$

- The false positive rate

$$FPR = \frac{FP}{FP + TN} \tag{24}$$

Some measures were proposed for imbalanced class problems:

- The *G-mean* (or Geometric mean) is the geometric mean of the accuracy of each class.

$$G\text{-}mean = \sqrt{Specificity \times Recall} \tag{25}$$

where the sizes of different classes have already been considered so it is a good measurement for class-imbalanced learning.

- The *F-measure* (or balanced $F_1$-score)

$$F\text{-}measure = 2 \times \frac{Precision \times Recall}{Precision + Recall} \tag{26}$$

is designed as the harmonic mean of precision and recall, and it can be generalized in $F_\beta$

$$F_\beta = (1 + \beta^2) \times \frac{Precision \times Recall}{\beta^2 \times Precision + Recall} \tag{27}$$

where $\beta$ is a weight for precision and recall. The greater the $\beta$, the higher the domination of recall.

- The *Adjusted F-measure* ($AGF$) (Maratea et al., 2014)

$$AGF = \sqrt{F_2 \times InvF_{0.5}} \tag{28}$$

where $F_2$ is computed by setting $\beta = 2$ in $F_\beta$ and $InvF_{0.5}$ is computed on the following confusion matrix:

| | Ground-truth Negative | Ground-truth Positive |
|---|---|---|
| Predicted Positive | TN (True Negative) | FN (False Negative) |
| Predicted Negative | FP (False Positive) | TP (True Positive) |

Compare to 1, this confusion matrix switches the class labels of each samples (positive samples become negative and vice versa). With the confusion matrix in table 3.7, the $InvF_{0.5}$ is computed as the standard $F_{0.5}$

Besides, the ROC curve (Swets, 1988) was used to assist the evaluation. "ROC" is the abbreviation fro *Receiver Operating Characteristic*. A ROC curve demonstrates a trade-off between true positive and false positive rates provided with different classification parameters, and illustrates how the accuracy on positive instances drops with the error rate on majority instances. Informally, one point in ROC space is superior to another if it is closer to the upper-left corner (TP is higher, but FP is lower). Thus, ROC curves allow for a visual comparison of classifiers: the larger the area below the ROC curve, the higher classification potential of the classifier.

Hence, in the later sections, we chose *Recall*, *G-mean*, *F-measure* and *AGF* as the performance measures. We also use the ROC curve as an assistance to the evaluation.

## 3.8 Ensemble learning methods

To solve the imbalanced class learning problem, two categories of techniques have been proposed: sampling approaches and algorithm-based approaches. In section 3.5.2, we discussed some sampling approaches and demonstrated the performance improvements to the algorithm by using them on the imbalanced data. Algorithm-based approaches are twofold. The first category aim at improving a classifier's performance based on its inherent characteristics. For example, methods that are particular tailored for Decision Trees, Neural Networks (MLPs), Naive Bayes systems, etc. The second category is ensemble learning methods, which intergrates several weak classifiers to improve the generalization or robustness over a single estimator (Opitz and Maclin, 1999; Polikar, 2012; Rokach, 2010).

In classification problems, ensemble methods contain a number of classifiers called *base classifiers*. Ensemble methods are appealing mainly because they are able to boost *weak classifiers* which perform slightly better than random guess in oprder to get a *strong classifier* with high accuracy. Hence, sometimes *base classifiers* are also referred to as *weak classifiers*. In order to further improve the performance of prediction results on the imbalanced data sets, ensemble learning methods have been widely studied and applied (Chawla et al., 2003; Chen et al., 2004; Guo and Viktor, 2004; Liu, 2009; Liu et al., 2011).

In this section, we first quickly introduce some ensemble methods and then we apply these methods to our problem. We then propose an ensemble SVM algorithm for automatic detection of PPs. Finally,experimental results are presented and discussed.

### 3.8.1 The Bagging Algorithm

The name Bagging was the abbreviation of *Bootstrap AGGregatING* (Breiman, 1996). As the name implies, two key processes of Bagging are bootstrap and aggregation. Bagging is a famous representative of parallel ensemble learning methods, and it is directly based on bootstrap sampling.

Given a dataset $D$ that contains $n$ samples, Bagging randomly generates $T$ new training datasets $D_i$ of size $m$ by sampling from $D$ uniformly and with replacement, a sampling method known as bootstrap sample (Efron and Tibshirani, 1994). In each $D_i$, some samples are repeated and others are unselected.

Then we use these $T$ datasets to generate $T$ models and combine them by voting the prediction results. Although it is usually applied to decision tree methods, it can be used with any type of classification method. A general Bagging algorithm is shown in Algorithm 2.

**Algorithm 2:** Bagging

**Input:** Data set $D = \{(\mathbf{x}_1, y_1), (\mathbf{x}_2, y_2), \ldots, (\mathbf{x}_m, y_m)\}$, $y \in \{-1, 1\}$ ;
Base learning algorithm $\mathcal{L}$; Number of base learners $T$.

**for** $i \leftarrow 1$ **to** $T$ **do**
  $l_i = \mathcal{L}(D, \mathcal{D}_{bs})$ (* $\mathcal{D}_{bs}$ is the bootstrap distribution *)
**end**

**Output:** Majority vote of predict label $sgn(\sum_{i=1}^{T} l_i(\mathbf{x}))$.

### Random Forest

(Breiman, 2001). It operates by constructing a multitude of decision trees. The decision tree consists of a set of tree-structured decision tests working in a *divide-and-conquer* way. Each non-leaf node is associated with a feature test called *split*; data falling into the node will be split into different subsets according to their different values on the feature test. Each leaf node is associated with a label, which will be assigned to instances falling into this node. In prediction, a series of feature tests is conducted starting from the root node, and the result is obtained when a leaf node is reached (Rokach and Maimon, 2007; Zhou, 2019).

In RF, each tree in the ensemble is built from a sample drawn with replacement (i.e., a bootstrap sample) from the training set. And furthermore, a random selection of features is introduced into the training process. Specifically, the traditional decision tree greedily chooses the best split feature from the current features set (suppose there are $d$ features) in the construction of the tree. However, the RF first randomly selects $k$ features from the current features set, and then choose the best split feature of the subset. Herein, the $k$ constrains the stochastic extent: If $k = d$, the base decision tree is the same as the traditional decision tree; If $k = 1$, it means we randomly select one feature to split; In general, the recommendation is $k = \log_2 d$.

### Extremely Randomized Trees

The Extremely randomized trees (or *Extra-Trees*) builds an ensemble of unpruned decision or regression trees according to the classical top-down procedure. Its two main differences with RF are that it splits nodes by choosing cut-points fully at random and that it uses the whole learning sample (rather than a bootstrap replica) to grow the trees (Geurts et al., 2006). In other words, in extremely randomized trees, randomness goes one step further in the way splits are computed. This usually allows to reduce the variance of the model a bit more, at the expense of a slightly greater increase in bias.

### 3.8.2 Ensemble Support Vector Machine

Although weak classifiers can be boosted by using ensemble methods, the resulting performances are still related to those of the base classifiers. Generally the base classifiers are also trained on balanced datasets. Hence, a general problem of bagging algorithms is the neglect of potentially useful information contained in the majority class instances. To keep a high efficiency of under-sampling but reduce the possibility of ignoring information, a simple strategy was adopted in many ensemble methods (Liu, 2009; Liu et al., 2011). It randomly genrates multiple subsets of samples $\{N_1, N_2, \ldots, N_T\}$ from the majority class $N$. The size of each subset is the same as the minority class $P$, i.e.$|N_i| = |P|$. Then, the union of each pair of $N_i$ and $P$ is used to train the base classifiers.

We proposed the ensemble SVM (EnsSVM) algorithm by combining this sample strategy and the morphological over-sampling strategy used in section 3.5.2. The algorithm is illustrated in Figure 39. At first, we augment the PPs instance by labelling their two nearest neighbors on the STS fundus as PPs (section 3.5.2), and get a total of $S$ PPs. Here, the rebalancing process is important to avoid learning from extremely imbalanced data, and a certain amount of training data is necessary to get reliable base classifiers. We then divide the data into training and test data. Note that this step is only needed for the algorithm evaluation, while for a final model applied to detect PPs in new data, we learn from the full dataset. After that, the majority (non-PP) data is under-sampled $T$ times to generate $T$ bootstrap samples (sampling with replacement) and the size of each subset of samples is $S$. Afterwards we combined each bootstrap samples with the over-sampled positive instance (PPs) to form the balanced training data used to train the base SVM. Finally, for a test instance, the classification decision was made through a majority voting. A formal EnsSVM algorithm is shown in Algorithm 3.

### 3.8.3 Experiments and results

To assess the performance of the ensemble learning method presented in this section, we trained and tested the algorithms on the HCP data with a 10-fold cross-validation. For the models with parameters selection, we used the $10 \times 10$ nested cross-validation (or called double cross-validation). Since the nested cross-validation integrates the model selection procedure independently to prevent selection bias, it can further overcome the bias in performance evaluation and reflect best practice in operational use (Cawley and Talbot, 2010). Here, for each fold of cross-validation, the test data category has the same distribution as the original data and the feature vectors (or images) are generated using ASD feature maps. The performance of all algorithms was estimated with the evaluation measures presented in

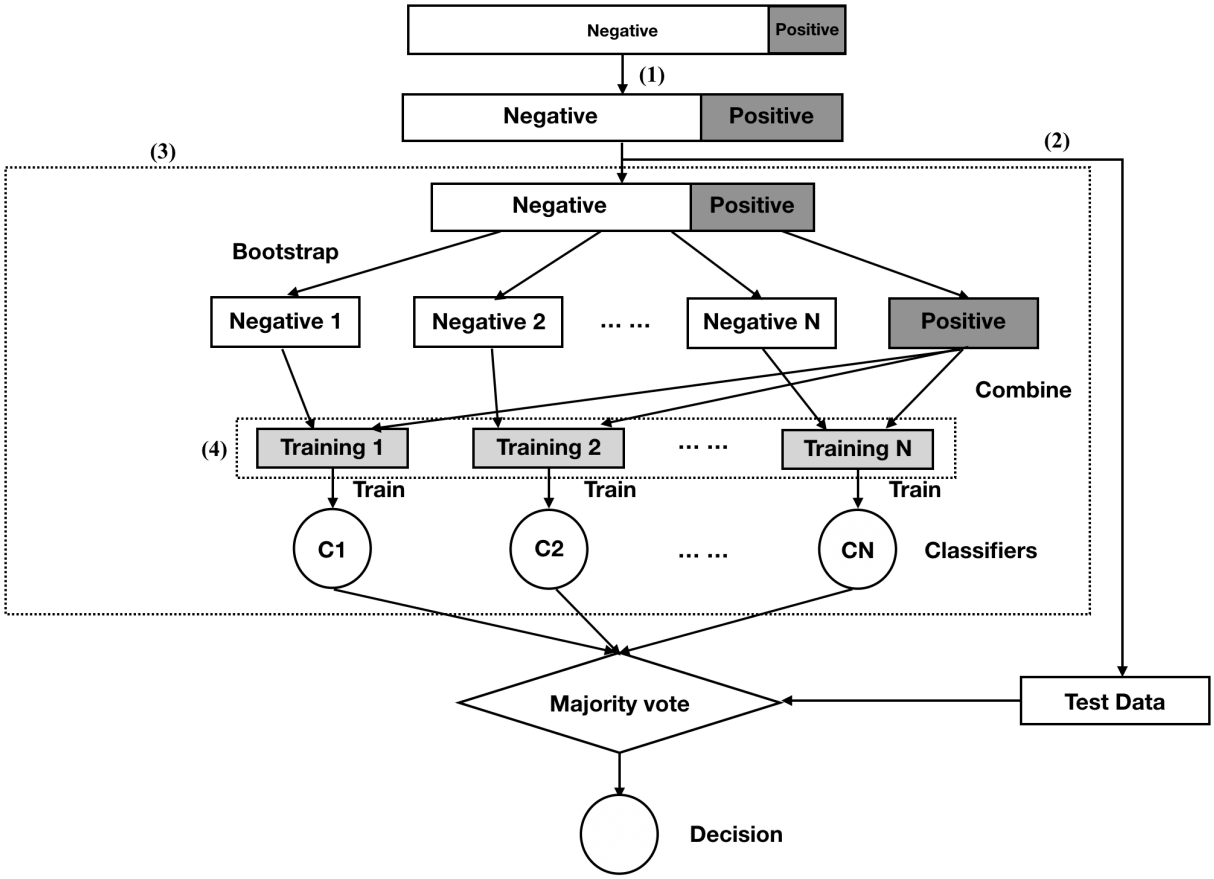


Figure 39: The ensemble SVM algorithm. (1) Augment the PPs instances by considering the two nearest neighbors of PPs as also PPs; (2) Divide the data into training and test data; (3) Build the base classifier; (4) The balanced datasets for training base classifiers.

**Algorithm 3:** EnsSVM

**Input:** Data set $D$; Number of nearest neighbors: $K$; Number of base SVM: $T$.

Split $D$ into minority class $P$ and majority class $N$;

$N_2, P_2 = MorS(N, P, K)$ (* over-sample the $P$ by the morphological strategy with $K = 2$ *) ;

For all data, divide the data into training and test data with same distribution of $P_2$ and $N_2$. Denoted as $D_{train} = \{(\mathbf{x}_1, y_1), \ldots, (\mathbf{x}_n, y_n)\}$, $D_{test} = \{(\mathbf{x}_{n+1}, y_{n+1}), \ldots, (\mathbf{x}_{n+l}, y_{n+l})\}$;

$S = Size(P_{train})$ (* get the size of minority class in training data $P_{train}$ *);

**for** $i \leftarrow 1$ **to** $T$ **do**

  $N_i = Bootstrap(N_{train}, S)$ (* get bootstrap datasets of $N_{train}$, and each set has $S$ instances *);

  $BT_i = P_{train} \cup N_i$ (* form the balanced training dataset *);

  Build a base classifier $SVM_i$ with $BT_i$;

  Feed $SVM_i$ with $D_{test}$, and get a predicted class label array $Arr_i$;

**end**

**for** $j \leftarrow 1$ **to** $l$ **do**

  Get $y_{n+j}$ by casting a majority vote over $Arr_1, Arr_2, \ldots, Arr_i$

**end**

**Output:** Predicted class label for $D_{test}$.

section 3.7. The ensemble methods were trained as follow:

**General bagging models:** We trained the bagging methods using the base classifier of $k$-NN, linear SVM and SVM with RBF kernel respectively. All bagging models were trained on balanced datasets containing 4462 feature images of 2231 PPs and non-PPs.

**Random Forest and Extra-trees:** We trained RF and Extra-trees with $50, 200, 500$ decision trees(DT). Suppose there are $d$ features, the number of features considered at each split $k = \sqrt{d}$. Both models were trained on the balanced dataset. As a comparison, we also trained a RF model on the imbalanced dataset. Herein, we used the scikit-learn implementations of RF and Extra-trees. It should be noted that the implementations combine the base classifiers by averaging their probabilistic prediction rather than doing a simple majority vote.

**EnsSVM:** We used SVM with RBF kernels as the base classifiers of EnsSVM. The optimal parameters of RBF kernels were selected by cross-validated grid-search over a parameter grid of $C$ and $\gamma$, where the parameter $C$ was selected from a sequence of equal differences 1 to 10 by factors of 1 and the parameter $\gamma$ was selected from a sequence of $10^{-4}$ to $10^{-3}$ by factors of $10^{-4}$.

As a comparison, we also trained some single base classifiers including a single SVM trained on the balanced data by MorS and a single SVM trained on the imbalanced data after augmentation of PPs by Mors (imbalanced ratio $\approx 1 : 5$); In addition, the other

SVMs used the RBF kernel, and the training of General bagging models and EnsSVM was performed using 21 component classifiers, which we determined empirically to be a high enough number to get robust and high performances.

Table 15 presents the performance for all the methods. As visible, EnsSVM achieves the best results in Recall, G-mean and AGF, and the Extra-trees of 500 desion trees performs best in F-measure. In comparison with the single SVM, ensemble methods show improved performances. Moreover, in RF and Extra-trees, as the number of decision tree increases, the model results get better until the upper limit. Also, the results of Bagging 10-NN model indicate that not all base classifiers can be boosted by the ensemble method.

Table 15: The Average value of model performance measures

| Models | Recall | G-mean | F-measure | AGF |
|---|---|---|---|---|
| EnsSVM | **0.811** | **0.773** | 0.527 | **0.774** |
| Bagging SVM | 0.786 | 0.764 | 0.520 | 0.764 |
| SVM (balanced data) | 0.781 | 0.764 | 0.522 | 0.764 |
| SVM (imbalanced data) | 0.298 | 0.540 | 0.423 | 0.550 |
| Bagging linear SVM | 0.715 | 0.487 | 0.291 | 0.540 |
| Random Forest 500DT | 0.749 | 0.762 | 0.528 | 0.760 |
| Random Forest 200DT | 0.746 | 0.759 | 0.523 | 0.758 |
| Random Forest 50DT | 0.732 | 0.751 | 0.516 | 0.749 |
| Extra-trees 500DT | 0.761 | 0.766 | **0.531** | 0.764 |
| Extra-trees 200DT | 0.757 | 0.765 | **0.531** | 0.764 |
| Extra-trees 50DT | 0.742 | 0.758 | 0.525 | 0.756 |
| Bagging 10-NN | 0.282 | 0.501 | 0.310 | 0.497 |

Besides the measures above, we depict the mean ROC curves created from 10-fold cross-validation of 4 selected ensemble methods in Figure 40. Clearly, combining all measures, the EnsSVM outperforms the other methods in general.

In order to better understand our results, we focused on the prediction results of our EnsSVM model. Figure 41(a) shows the Recall rate across different ranges of depth. Intuitively, the deeper a PP the more buried it is and the more difficult it is to detect. Our model yielded an excellent prediction (mean Recall $> 90\%$) on the most superficial PPs with depth $\in [0, 5.0)mm$. As depth increases, the prediction accuracy decreases. In particular, for the deepest PPs, with depth $\in [20, \infty)mm$, Recall falls below its overall mean (81.1%) but is still high with a score of 78.5%. The mean recall is above 80% for all depth below $15mm$. Using the same DPF-based criterion than (Bodin et al., 2021), we divided PPs in two groups, superficial and deep, and calculated Recall (Figure 41(b)) for both groups. The mean Recall of superficial PPs and Deep PPs is 92.4% and 78.98% respectively. The above results indicate that the EnsSVM has a relatively good prediction accuracy for the detection

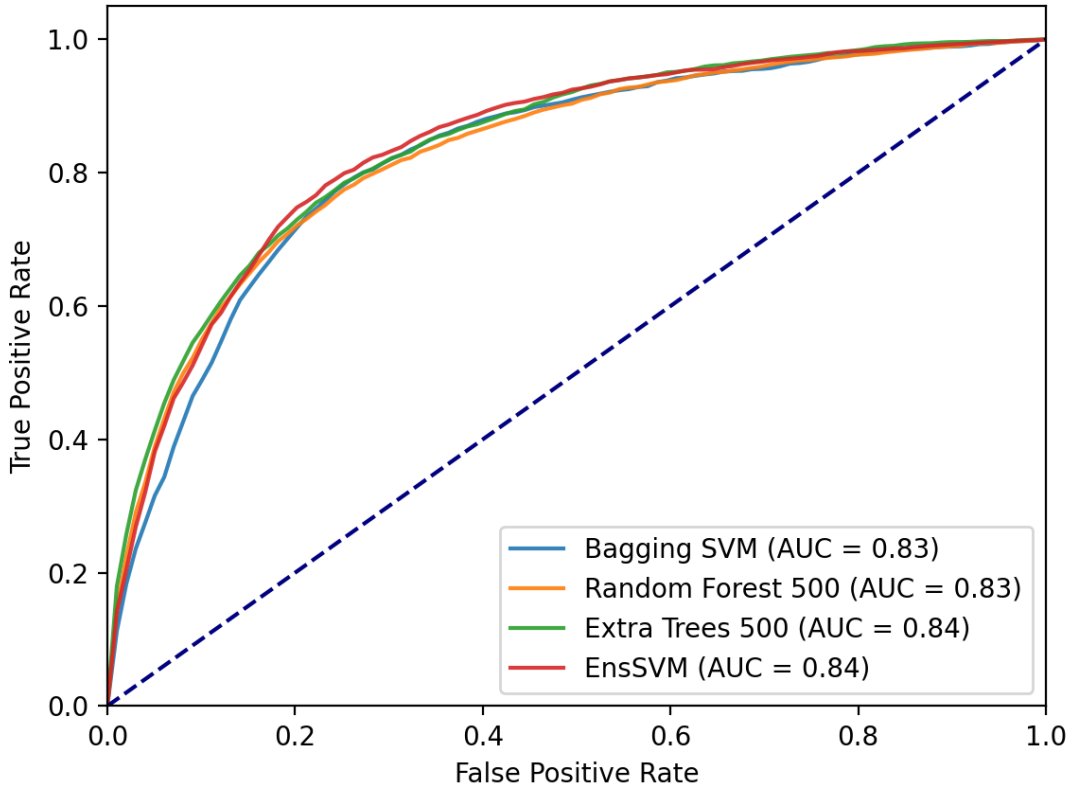


Figure 40: ROC curve of ensemble methods. The AUC is the area under the curve.

of PPs, including for the very difficult cases with PPs buried in the depth of the STS.

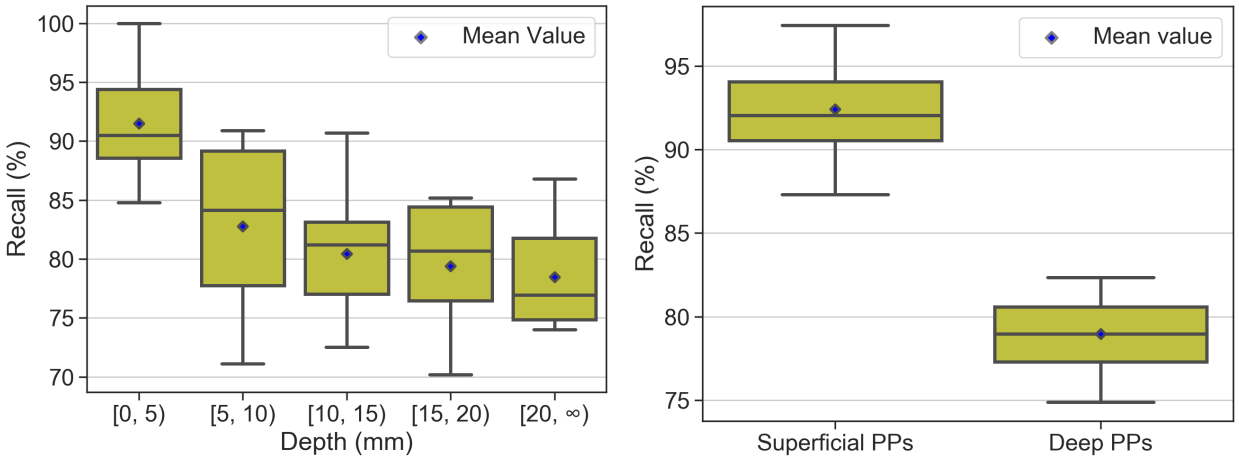


(a) Recall vs. Depth (b) Recall vs. Types of PPs

Figure 41: The Recall of EnsSVM across various categories of PPs.

## 3.9 PPs regions and post-processing

In the earlier sections, we compared a number of machine learning methods and finally proposed the EnsSVM to solve our PPs detection problem. In addition to the correctly predicted PPs (TP cases), the wrongly predicted PPs (FP cases) also need to be taken carefully when putting the models into practice. In this section, we first study FP cases produced by ensemble methods. Then, a post-processing method is proposed as a solution to the FP cases. Finally, we apply our method on the TVA data without manual labelled PPs for an empirically evaluation of the model performances, and a quantitative comparison of PPs is presented with the manually identified PPs from the HCP data.

### 3.9.1 False positive PPs

Table 16: The false positive rate of four ensemble methods

| | EnsSVM | Bagging SVM | Random Forest 500DT | Extra-trees 500DT |
|---|---|---|---|---|
| FPR | 0.263 | 0.258 | 0.227 | 0.230 |

Table 16 shows the average false positive rates (FPR) of selected ensemble methods among 10-fold cross-validations. Approximately 25% of Non-PPs instances were predicted as PPs. We found that the number of FP instances was almost as much as the number of PPs instances in each fold. In order to further analyse the FP instances, we randomly chose 10 subjects from the HCP data as test data and used the rest 90 subjects to train

the EnsSVM model. After getting the EnsSVM model, we applied it to the test data and displayed the prediction result on the STS fundus using Anatomist visualization software (Le Troter et al., 2011).

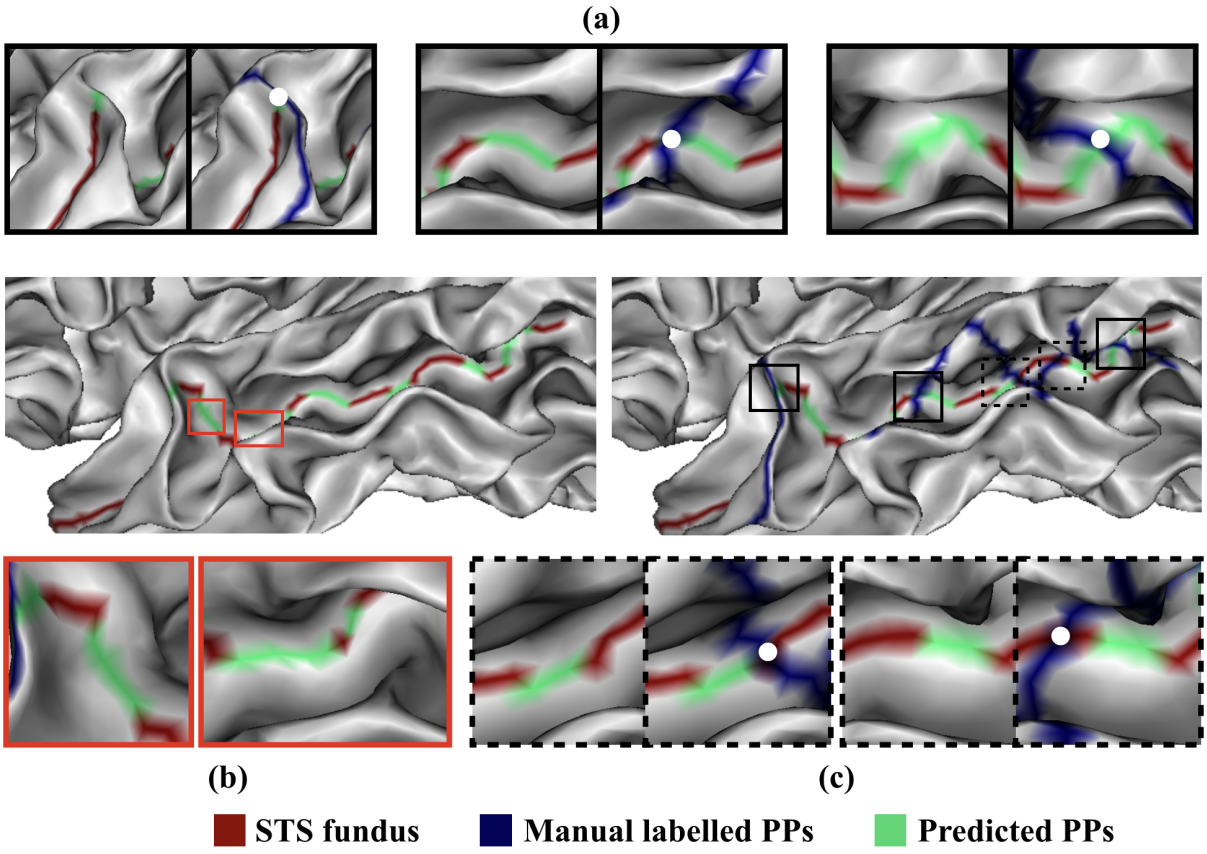


Figure 42: An example of predicted PPs using EnsSVM models. In the middle, the prediction results were projected on the STS fundus. The LEFT without manual labelled PPs and the RIGHT with the manual labelled PPs. In these figures, the predicted vertices of PPs are colored in green and the non-PPs were in dark red. The dark blue lines across the STS are manual labelled PPs lines. The intersection points between PPs lines and STS fundus were marked with the white dots. Three different cases of prediction results are marked in different box. (a) Black solid box: the manual labelled PPs are in the predicted PPs regions; (b) Red solid box: the predicted PPs regions without manual labels; (c) Black dotted box: the manual labelled PPs near the predicted PPs regions.

An example of prediction results of PPs is illustrated in Figure 42. As we can see from it, instead of single vertex, most predicted results of PPs vertices were close to each other and connected as a single region. The original PPs points (in white) were located in or nearby the predicted regions. Actually, when we trained the machine learning models, we also considered the two nearest neighbors of manual labelled PPs as the ground-truth and these three points formed a manual PPs region.

When predicted regions include the original PP point, the model clearly detected the

PP (Fig. 42(a), 43(a)). When predicted regions do not include the PPs points, but are adjacent to it, the manual and predicted PPs regions were adjacent or partially overlapped (see Figure 43). We believed these situations remained the cases for correct predicted PPs. In addition to these two cases, we still detect regions that are far from any manually labelled PP. See for instance Figure 42(b)-left in which the detected regions are indeed FP cases with no sign of a WP.

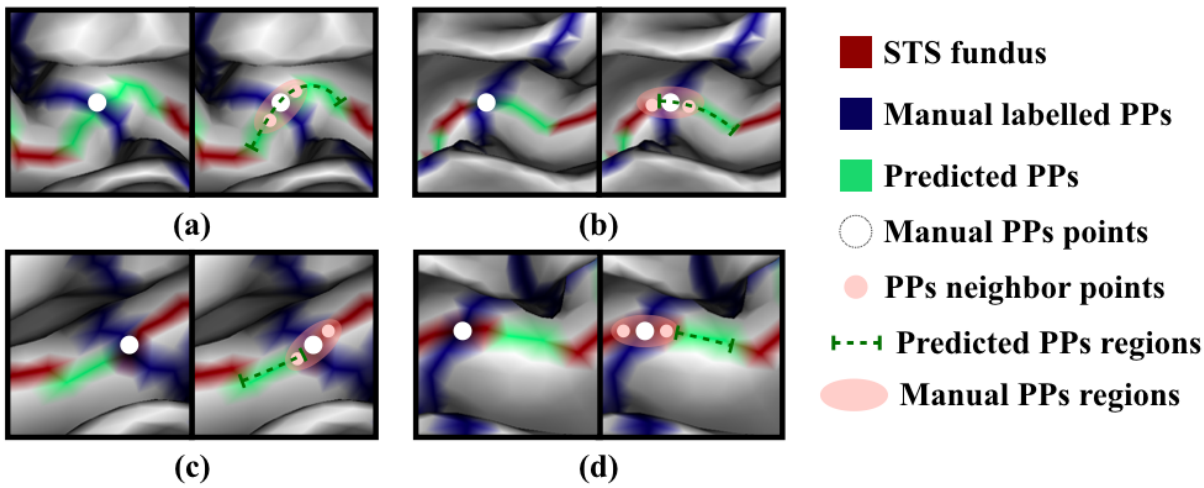


Figure 43: Location of manual labelled and predicted PPs. In each sub-figure, the LEFT shows the original manual labelled PPs and predicted PPs. The RIGHT shows the manual PPs regions of three PPs instances used for training (in pink ellipse) and the region of predicted PPs (in green dotted arrow). Here we take the manual PPs regions as the ground-truth and have the following cases: (a) the ground-truth is well located in the predicted PP region; (b), (c) the ground-truth and predicted PPs regions have overlapping parts; (d) No overlap between the ground-truth and the predicted PP region, but they are adjacent to each other.

Back to the FPR, as a evaluation measure, FPR is inappropriate as a major index in the class-imbalance problem. For example, if we simply predicted all the samples as negative class, the FPR is zero but no positive case detected. In our problem, the FP instances are the points that are predicted as PPs but do not intersect with the ground-truth. However, most FP instances are adjacent to the ground-truth, and some predicted regions include both TP and FP instances. Hence, the FP cases inspired us to learn more about the PPs regions and propose a post-processing strategy to refine the prediction results of EnsSVM.

### 3.9.2 PPs regions

After our data augmentation strategy, each ground truth PP region corresponds to a manually labelled PP and contains three points: the manually labelled PP point and its two

adjacent points on fundus (see Figure 43 Manual PPs regions). We therefore assume that a PP region on the STS fundus is composed of at least three consecutive points, and a set of more than 5 consecutive points should be considered as containing more than one PP (e.g. when PPs are close enough they will be detected as a single region). For a better understanding of the results, we used all HCP data to train a EnsSVM and applied it to the TVA dataset. For each point, we got the predicted label and the associated probability from the EnsSVM. Here the probability is the mean probability of all based SVM classifiers.

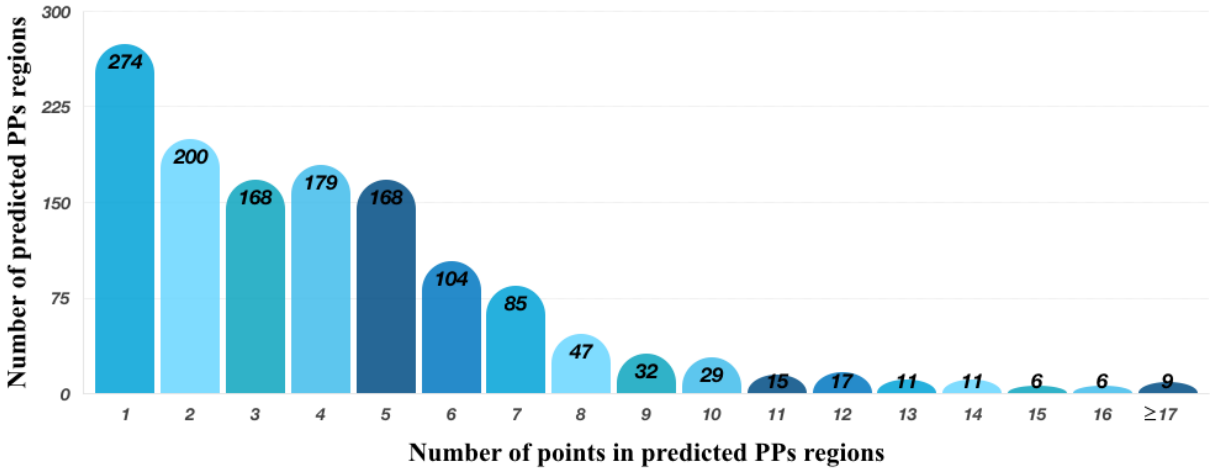


(a) Histogram: count of predicted PPs regions

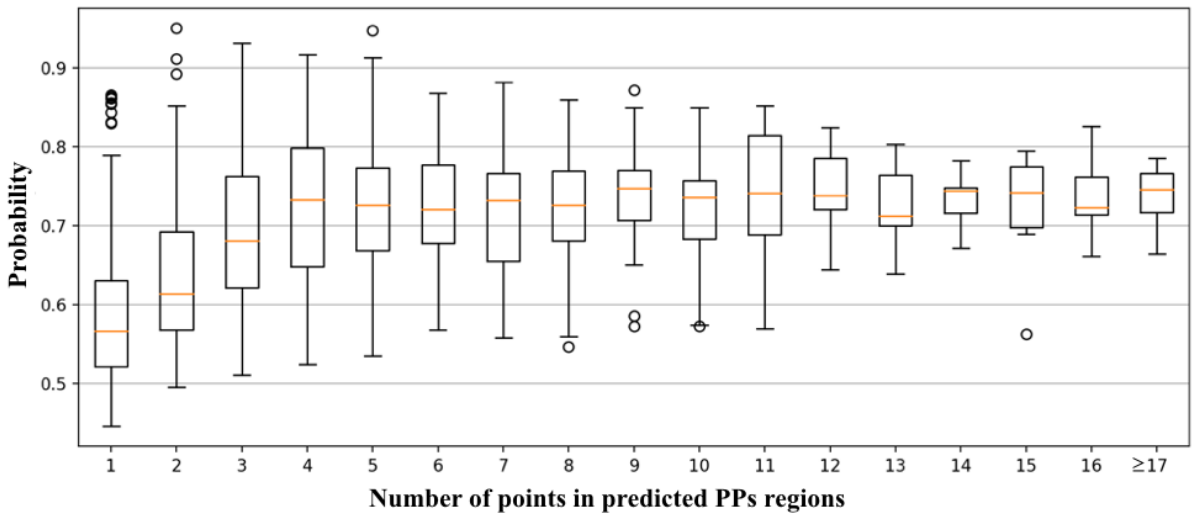


(b) Box graph: average probability of predicted PPs regions

Figure 44: Statistics of predicted PPs regions using EnsSVM in TVA data. (a) we count the number of predicted regions with different points; (b) the average probability of each region is calculated by the average of the probabilities of the predicted PPs points in each region.

Figure 44 shows the histogram of the number of points per PP region, as well as the probabilities associated to regions of a certain size. As we can see, most predicted PPs

regions contained 5 points or less, but some can contain up to 17 or more points. Regions with one or two points are the most frequent, wit 274 and 200 occurrences respectively. However, they also have the lowest associated probability, with a median probability of 0.56 and 0.61 respectively. It should be noted that the average probability of all predicted PPs regions containing three or more points is higher, around 0.7. Therefore, we believed that most of the predicted PPs regions with only one or two points were FP cases.

To further test our hypothesis, we randomly selected 10 subjects with manually labelled PPs (both left and right hemispheres) and used the remaining data to train the EnsSVM model. The results of PPs regions as shown in Figure 45. Similarly, the probability of a region containing 1 or 2 vertices is significantly smaller than that of other regions. After comparing with manual labels, the regions containing only 1 to 2 vertices are all FP cases.

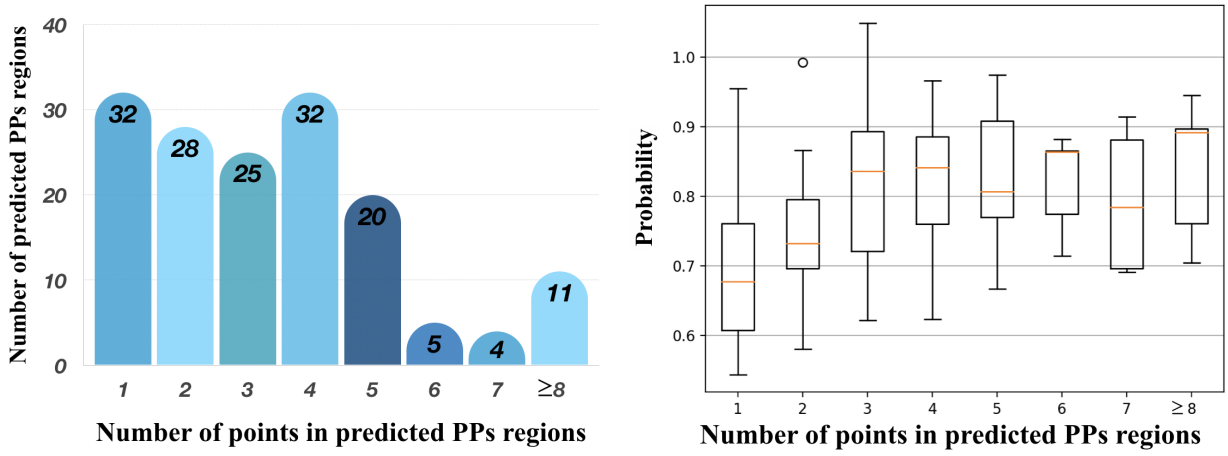


(a) (b)

Figure 45: Statistics of predicted PPs regions using EnsSVM on test dataset of 10 subjects. (a) we count the number of predicted regions with different points; (b) the average probability of each region is calculated by the average of the probabilities of the predicted PPs points in each region.

Besides, and as mentioned before, we also consider that predicted PPs region with more than 5 points probably contain more than one PP (e.g. when PPs are close enough they will be detected as a single region). Therefore, based on the definition and statistical analysis of PPs regions, once the points of the STS fundus have been classified, we propose the post-processing strategy to select the PPs from the PPs regions. The main steps of post-processing are as follow:

1. For each vertex on STS fundus, get its prediction label and the associated probability from the SVMs.

2. Compute PP regions as connected components of the PP label set.

3. Discard all regions with less than 3 vertices.

4. For regions with 5 vertices or less, select the vertex with maximum probability to represent the PP.

5. For regions with more than 5 vertices,

   a. Split the region at the vertex with minimum PP probability.

   b. If sub-region contains 5 vertices or less, go to step 4. Otherwise, iterate step 5.

The details are shown in Algorithm 4.

**Algorithm 4:** Post-processing

**Input:** Vertices of STS fundus $V = \{v_1, v_2, \ldots, v_n\}$; Predicted labels of vertices $L = \{l_1, l_2, \ldots, l_n\}$; Probabilities of vertices $P = \{p_1, p_2, \ldots, p_n\}$

**Output:** Selected vertices as PPs points $PPs$.

$PPs[]$: array for selected PPs;
$R = ConnectRegion(V, L)$ (* compute PPs regions as connected components of PP label set *);
$S = Size(R)$ (* get the number of points in each PP region *);
$R' = R - R_{S<3}$ (* discard all regions with less than 3 vertices *);
**for** $r \in R'_{S\leq 5}$ **do**
    (* regions with 5 vertices or less *);
    Select the vertex with maximum probability $V_{max(P)}$ to represent the PP;
    $PPs = PPs \cup V_{max(P)}$
**end**
**for** $r \in R'_{S>5}$ **do**
    (* regions with more than 5 vertices *);
    $R_{subs} = Split(r, V_{min(P)})$ (* Split the region at the vertex with minimum PP probability and get two sub-regions *);
    **for** $r_{sub} \in R_{subs}$ **do**
        **if** $0 < Size(r_{sub}) \leq 5$ **then**
            Select the vertex with maximum probability $V_{max(P)}$ to represent the PP;
            $PPs = PPs \cup V_{max(P)}$
        **else**
            $R'_{S>5} = R'_{S>5} \cup r_{sub}$ (* Iterate step 10 *)
        **end**
    **end**
**end**

### 3.9.3 Validation on TVA Data

We applied our method, including post-processing of regions, on the TVA data and quantitatively compared the distribution of PPs in the STS with the manually identified PPs from the HCP data.

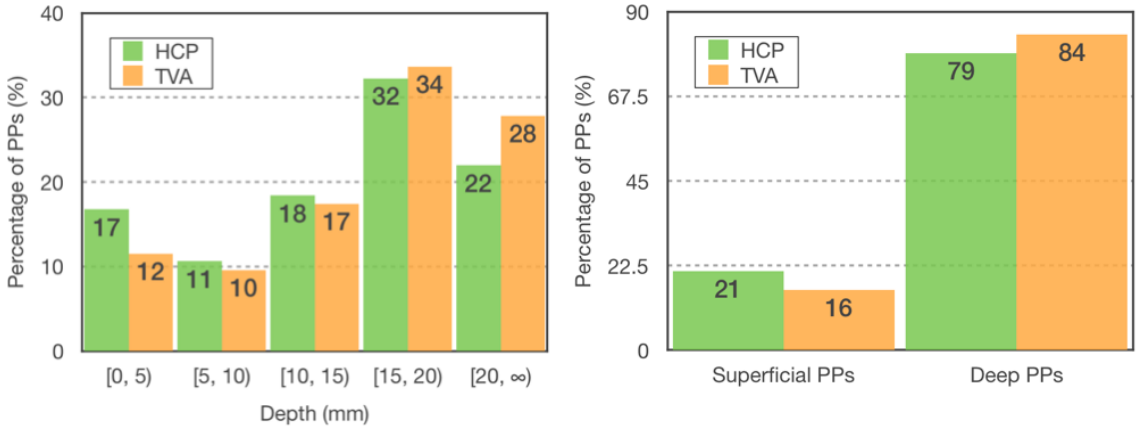


(a) HCP vs. TVA

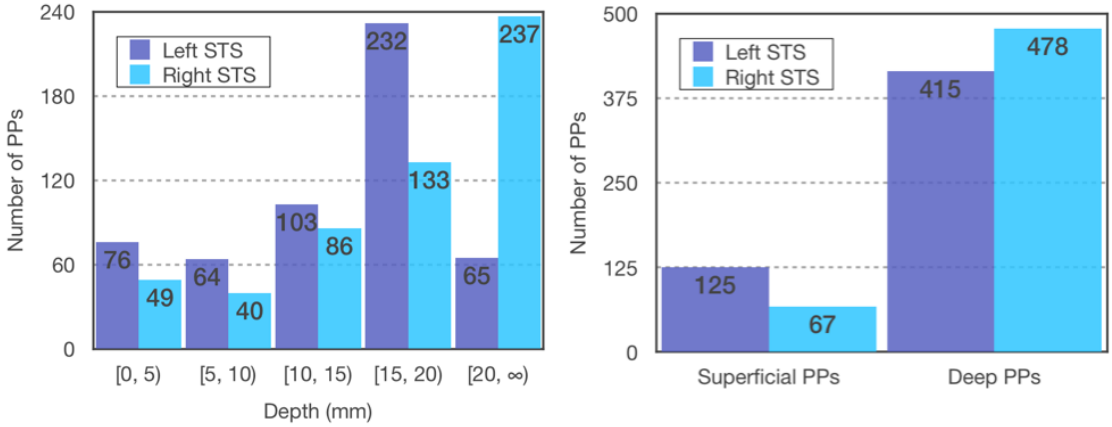


(b) Left STS vs. Right STS

Figure 46: The prediction results of PPs

On both hemispheres of the 92 subjects of the TVA data, 1085 PPs were detected, with 540 PPs in the left STS and 545 PPs in the right hemisphere. We detected 2 to 11 PPs in the left STS ($\text{Mean}_l = 5.86$) against 3 to 10 in the right STS ($\text{Mean}_r = 5.92$), and there was no significant difference between left and right STS across individuals ($p = 0.84$; Wilcoxon signed-rank test), which is identical to the manual results produced on the HCP data (Bodin et al., 2021). It is noticeable that our automatic classification detected more PPs per hemisphere than the manual identification on the HCP data ($\text{Mean}_l = 4.5$, $\text{Mean}_r = 4.3$). Nevertheless, the distribution of the number of PPs across depth ranges or different types of PPs is similar, as shown in Figure 46(a).

Again, PPs were subdivided into into superficial and deep ones. In the left STS, the number of superficial PPs $N_s = 125$ and the number of deep PPs $N_d = 415$, with a ratio of $1 : 3.32$, while in the right STS, $N_s = 67$ and $N_d = 478$, with a ratio of $1 : 7.13$. The ratios of superficial PPs to deep PPs differed significantly between left and right STS across individuals ($p < 0.05$; Wilcoxon) which is consistent with manual results presented in (Bodin et al., 2021). This difference in distribution across depth ranges between left and right is illustrated in Figure 46(b). It is visible that the PPs in the right STS are located in deeper regions than the left (see Figure 47), which again is consistent with (Bodin et al., 2021) and is in agreement with the fact that the right STS is notoriously deeper than the left STS (Leroy et al., 2015).

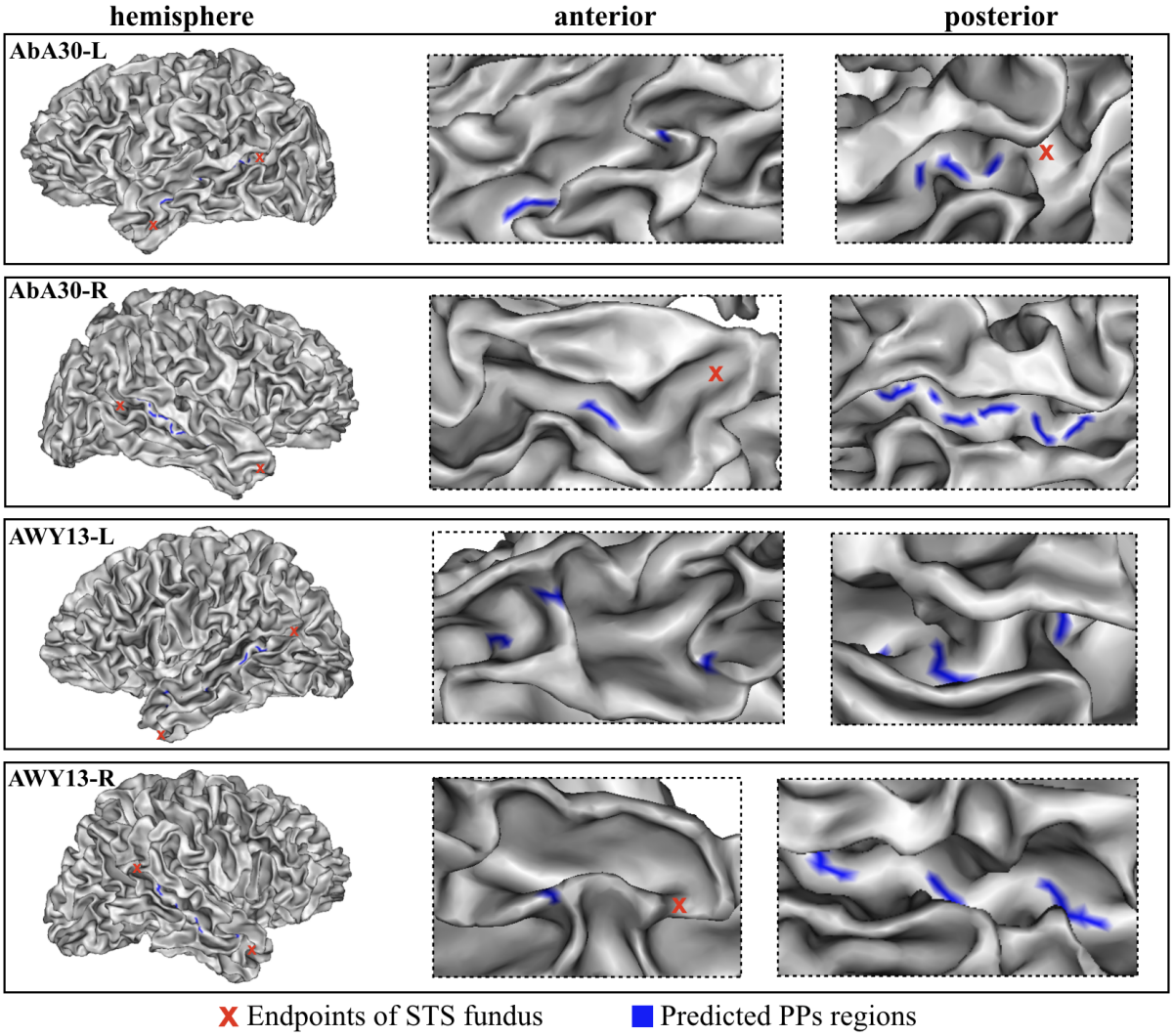


Figure 47: Comparison of prediction results between left and right hemispheres. More PPs in the anterior part of STS are detected in left-hemispheres than right-hemispheres. In general, the posterior part of STS is deeper than the anterior part.

## 3.10 Conclusion

PPs, an interesting benchmark for models of the cortical folding process, have been little studied until the last decades. Nevertheless, most studies were mainly focused on the superficial PPs instead of the deep PPs. The difficulty in identifying all the PPs, and furthermore the lack of a systematic method of automatically detection blocked the further studies. In this chapter, we presented a method to automatically detect the PPs by using the morphological characteristic "WPs" in (Bodin et al., 2021). At first, to better distinguish the new characteristic, the cortical surface profiling method (Li et al., 2010) was used to generate the new feature maps ASD and SOG. Both the results of experiments and visualisation showed the superiority of new maps in PPs identification compared to the DPF and curvature map. Then, for each vertex of the STS fundus, we used the same surface profiling method to generate their feature images recording the local geometrical information. After that, the 3D PP recognition problem is converted to a 2D image classification problem of class-imbalance where more points in the STS are non-PPs than PPs. To solve this case, an ensemble SVM model with a rebalancing strategy was proposed. Our results are very consistent with manual labelling, and show similar distributions of PPs across two different dataset.

Herein, we considered the vertices in STS as PPs or non-PPs, which makes the problem a binary classification. As PPs have been divided into "Superficial" and "Deep" by setting a DPF threshold in (Bodin et al., 2021), a multiclass classification (e.g. Non-PPs, Superficial PPs and Deep PPs) can be further investigated but obviously multiclass will lead to more unbalanced ratios among different classes. Also, as PPs have been shown to be associated with a specific type of superficial white matter (Bodin et al., 2021; Pron et al., 2021), the utilization of local connectivity information will not only give us a better understanding of PPs, but may also improve our model results. In the next chapter, we will focus on the local connectivity of short-ranged U-fibers.

# 4 Plis de Passage, short-range U-fibers connectivity and myelin maps

## 4.1 Introduction

Structural connectivity, which can be defined as the existence of white matter tracts physically interconnecting brain regions (Sporns et al., 2005; Uddin, 2013), arouses great interest in but not limited to the neurodevelopmental process (Dubois et al., 2014), functional organization (Saygin et al., 2012; Wendelken et al., 2017) and brain diseases (Griffa et al., 2013). Thanks to the development of modern in vivo brain imaging techniques in the last few decades, studies of the link between structural connectivity and cortical folding patterns have emerged (Li et al., 2010; Zhang et al., 2014; Shinohara et al., 2020; Van Essen, 2020; Zhang et al., 2020a,b; Bodin et al., 2021; Pron et al., 2021).

In particular, the U-fibers, which are known to connect adjacent gyri and cover the superficial layer of the brain (Oishi et al., 2008; Zhang et al., 2018; Shah et al., 2019), have shown a potential relationship to the PPs (Bodin et al., 2021; Pron et al., 2021) and some specific folding patterns, such as "Pyramid-Shape Crossings" (Shinohara et al., 2020) and "3-hinge gyri"(Zhang et al., 2020a). In more details, Pron et al. (2021) proposed a description of short-range U-fibers along the central sulcus (CS) at group level and provided the evidence of a significant relationship between the position of three U-fiber bundles and the hand area, which showed a relationship to the PPFM (Boling et al., 1999; Boling and Olivier, 2004; Yousry et al., 1997; Cykowski et al., 2008). Bodin et al. (2021) extracted the U-fibers along the superior temporal sulcus (STS) and found a co-localization of U-fibers and PPs, namely a dense short-range U-fibers below PPs location. Shinohara et al. (2020) observed and defined a novel anatomical structure called "pyramid-shape crossing" (see Figure 48(a)), which can be seen as a junction of inter-gyral U-fibers and intra-gyral U-fibers, by using fiber dissection and neuroimaging techniques. Zhang et al. (2020a) proposed a new method to compared the location of "3-hinge gyri" and underlying structural connectivity across individuals, and found a high dMRI-derived fiber density correlation.

As we can see from the Figure 48(a), the labelled junctional areas (3-way gyral junctions) of white matter ridges reveal how U-fibers contribute to the formation of the "pyramid-shape crossing" (Shinohara et al., 2020). For example, the area 18 was a convergence points of the intra-gyral U-fibers from 19, 16 and the inter-gyral U-fibers from 7 and 26. Also, we can clearly see the "wall pinches" (WPs) near the junctional area. In this example, moreover, the arrow 20-28 labelled a superficial PP and arrow 18-26 labelled a deep PP. Figure 48(b) show some examples of various gyral locations, and it visible in particular that the 3-hinge

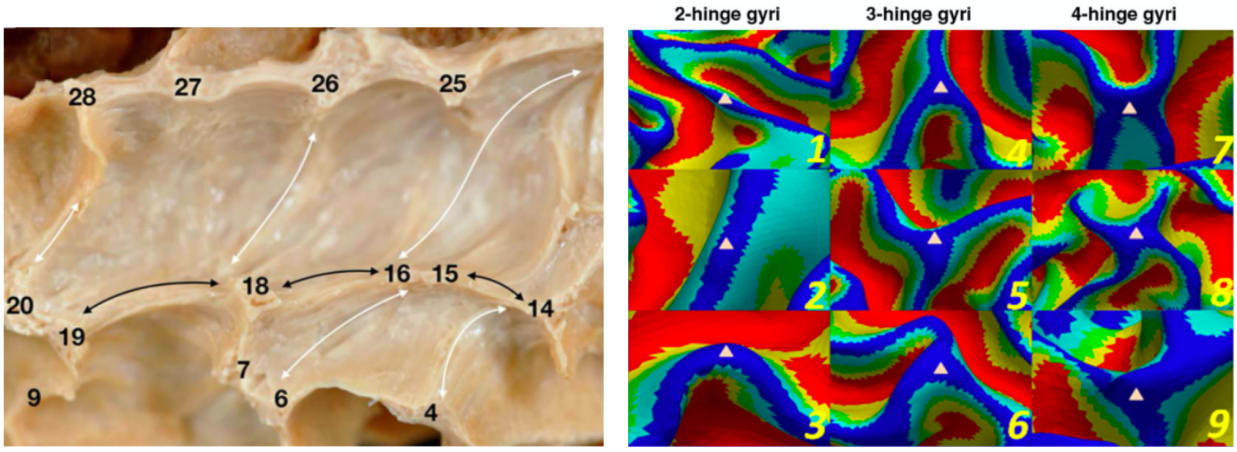


(a) (b)

Figure 48: (a) Examples of fiber dissection. The digital numbers label the pyramid-shape crossings area of various types of U-fibers. The white arrows show the inter-gyral U-fibers to connect between adjacent ridges, while the black arrows show the intra-gyral U-fibers to connect adjacent crossing. Figure adapted from (Shinohara et al., 2020); (b) Examples of N-hinge gyri. Small triangles denote the centers of detected gyri patterns. Figure adapted from (Li et al., 2010).

gyri are at the junction of a gyrus and a PP. So it seems that although defined in different nomenclatures, 3-way junctions (Shinohara et al., 2020), 3-hinge gyri (Li et al., 2010), and wall pinches/PPs are actually referring to similar structures and that they all have a link with underlying connectivity.

In this chapter, we study the structural connectivity, particularly short-range U-fibers, underlying the location of PPs. We first introduce a method to extract U-fibers used in this study and build density maps. Then, we carry out some machine learning experiments using the obtained density maps and analyse their results. After that, the myelin map as a supplement to the structural connectivity is discussed.

## 4.2 Materials and methods

In this study, we use the same processing pipeline than (Bodin et al., 2021; Pron et al., 2021) to process the diffusion MRI data and generate the streamlines or bundles of fibers, referred to as fibers. After getting all the fibers, we extract the U-fibers in regions of interest(ROIs) and separate them into different groups according to their pathways. Then, we generate density maps of their terminations on the cortical surface. Finally, a clustering approach is proposed to integrate the various density maps and generate a new one that shows the distribution of different U-fiber terminations along the cortical surface. The pipeline is illustrated in Figure 49 and described in the following sections.

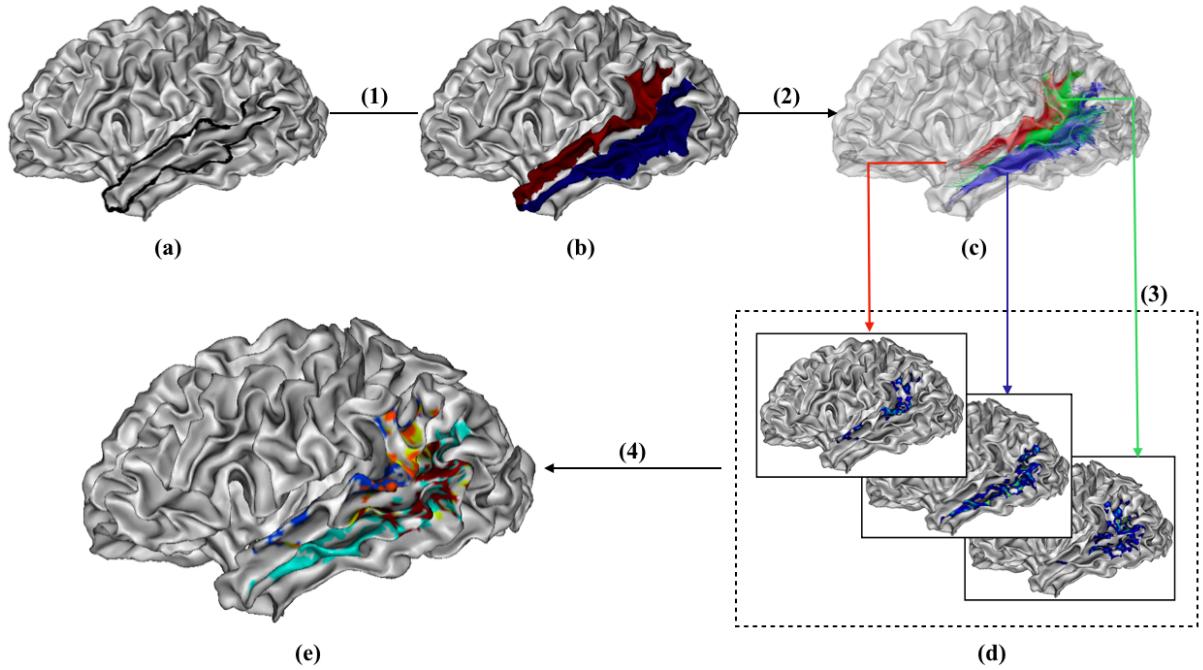


Figure 49: Analysis pipeline of U-fibers extraction and density maps generation of an example in STS. (a) Gyri identification, gyral crest lines of superior temporal gyrus(STG) and middle temporal gyrus (MTG); (b) STG (red) and MTG(blue) surface areas; (c) Extracted U-fibers: intra-STG U-fibers (red), intra-MTG U-fibers (blue), inter STG-MTG U-fibers (green); (d) Density maps of the U-fibers terminations; (e) Clustering results of three different density maps. Step: (1) Generate the ROIs from the gyral crest lines of STG and MTG; (2) Extract the different U-fibers depending on the area where their endpoints terminate. (3) Generate the density maps of U-fibers endpoints along the cortical surface. (4) Clustering the density maps of three different U-fibers.

### 4.2.1 Image acquisition and preprocessing

The structural MRI data of 100 HCP subjects used to generate cortical surfaces was processed in the same way than in section 3.2.

dMRI scans pre-processed by the HCP, i.e., corrected for subject movement, susceptibility induced artefacts, eddy-current induced distortions and gradients non linearities (Jenkinson et al., 2012; Glasser et al., 2013), were used to build whole brain tractograms with Mrtrix3 (http://www.mrtrix.org)(Tournier et al., 2019). dMRI pre-processed scans were first corrected for non-uniform intensity as recommended in (Jeurissen et al., 2014): for each subject, a single multiplicative bias field map was estimated from the mean $b = 0s.mm^{-2}$ volume adopting the ANTS (https://github.com/ANTsX/ANTs) N4 algorithm (Tustison et al., 2010) and this bias field was used to correct intensity of the whole dMRI sequence. For each subject, a multiple shell multiple tissue (MSMT) (cerebrospinal fluid, grey matter, white matter) response function was derived from the FreeSurfer tissue segmentation relying on the *dwi2response* command with default parameters. The resulting response function was used to fit a constrained MSMT spherical deconvolution model (Jeurissen et al., 2014) on the brain diffusion signal. Whole brain probabilistic tractography (Tournier et al., 2010) was performed with the *tckgen* command (algorithm = iFOD2, step = $0.625mm$, angle = $45°$, nb_streamlines = $5 \times 106$, minlength = $2.50mm$, maxlength = $300mm$) with seeding from the grey matter/white matter (GM/WM) interface volume and anatomical constraints (e.g., endings in the grey matter, see (Smith et al., 2012b)stemming from the FreeSurfer tissue segmentation.

The generated tractograms were filtered within the *Convex Optimization Modeling for Microstructure Informed Tractography* (COMMIT) framework (https://github.com/daducci/COMMIT) (Daducci et al., 2013, 2014) to remove spurious or overrepresented streamlines with respect to the dMRI signal. Stick-Zeppelin-Ball (Panagiotaki et al., 2012) with default diffusivity parameters (parallel diffusivity= $1.7 \times 10^{-3} mm^2.s^{-1}$, intracellular fraction = 0.7 , isotropic diffusivities = $1.7 \times 10^{-3}$ and $3.0 \times 10^{-3} mm^2.s^{-1}$) was selected as a forward model (Daducci et al., 2014). The resulting tractograms contained an average of one million streamlines, which corresponds to a reduction of eighty percent.

The association streamlines, i.e., connecting ipsilateral cortical territories, were extracted from the filtered tractogram, using their endpoints and a binary mask of each hemisphere cortical grey matter. These streamlines were further filtered with respect to the GM/WM mesh as follows. The exact signed distance from the streamlines points to the GM/WM mesh was computed relying on trimesh (https://github.com/mikedh/trimesh). Each segment composing a streamline was classified into intersection, intracortical (grey matter) or subcortical (white matter) using the values of the signed distance at the mesh of its endpoints. Streamlines with more than two intersections with the mesh were excluded. Regarding streamlines with at most two intersections, only the intersections and the subcortical components were retained, with the latter having a length greater than the minimum

value of $2.50mm$.

### 4.2.2 U-fibers extraction

According to the criteria in (Bodin et al., 2021; Pron et al., 2021), we extracted the U-fibers in both central Sulcus(CS) and STS. At first, the extraction of specific cortical landmarks related to these two sulci were semi-automatic generated by using the SurfPaint module (Le Troter et al., 2011). This software can extract either gyral crest or sulcal fundus lines as geodesic lines between two extremities, with these geodesic lines minimizing or maximizing, respectively, the DPF along their path. The gyral lines extremities based on anatomical landmarks identifiable in each subject as described in previous studies (Bodin et al., 2018, 2021; Pron et al., 2021), and the selections of extremities are as follow:

**CS:** The dorsal extremity of the gyral crest lines was set at the apex of the characteristic notch made by the CS on the medial face of the GM/WM mesh. The ventral extremity was set on the crest of the subcentral gyrus (SubCG).

**STS:** The anterior extremity was chosen at the tip of the temporal lobe excluding the last polar sulcus that is often oriented transversally to the STS (Ochiai et al., 2004). The posterior extremity was chosen at the intersection between the STS horizontal main branch and its posterior ascending branches (Segal and Petrides, 2012).

After we manually determined the extremities, the fundus line and two gyral crest lines were drawn automatically, following the deepest and shallowest path between their respective extremities (Le Troter et al., 2011; Bodin et al., 2021). Note that for the STS, two adjacent gyri are STG and MTG, and for the CS, they are the pre-central gyrus (PreCG) and the post-central gyrus (PoCG). Then, two ROIs corresponding to the adjacent gyri were generated by using two crest gyral lines and the fundus line. The corresponding ROI was defined as the GM/WM mesh vertices located closer to the crest line than the local geodesic distance between the crest line and the fundus line (see Figure 49(b)).

After generating the ROIs, we projected the termination of fibers onto the GM/WM mesh points by minimizing the Euclidean distance. U-fibers were then extracted as streamlines with their two terminations projected on two (identical or different) ROIs (STG and MTG in STS or PreCG and PoCG in CS). The top one percent of the longest U-streamlines in each sulcus were filtered out to remove obvious outliers such as looping streamlines. Then, we selected the short-range U-fibers between 10 and 60mm in length (Shinohara et al., 2020; Bodin et al., 2021). For all the extracted U-fibers, according to the locations where their endpoints terminate, we divided them into three groups as follow:

**CS:**

1. Intra-PreCG U-fiber: both two endpoints of the streamline terminate in the PreCG;
2. Intra-PoCG U-fiber: both two endpoints of the streamline terminate in the PoCG;
3. Inter-PreCG-PoCG U-fiber: one endpoint terminates in the PreCG and the other in the PoCG.

**STS:**

1. Intra-STG U-fiber: both two endpoints of the streamline terminate in the STG;
2. Intra-MTG U-fiber: both two endpoints of the streamline terminate in the MTG;
3. Inter-STG-MTG U-fiber: one endpoint terminates in the STG and the other in the MTG.

### 4.2.3 Density map generation

After U-fibers extraction, the next step is to generate the density maps of U-fibers on the cortical surface. Herein, the density maps are computed as the streamline endpoints along the GM/WM mesh, namely the intersection between the streamlines of U-fibers and the GM/WM mesh. A well-known problem is that most streamlines stop in the middle of the white matter without reaching the grey matter regions (Jbabdi and Johansen-Berg, 2011; Smith et al., 2012a; Girard et al., 2014). An example is shown in Figure 50, most streamlines are below the GM/WM mesh so that we can not generate a robust and convincing density maps (see Figure 51). Moreover, the effects of the well-known *gyral bias* (Reveley et al., 2015) prevent a good localization of the fiber terminations. In order to overcome these limitations, we use the Surface-enhanced tractography (SET) method (St-Onge et al., 2018). Specifically, we generated a smooth version of the surface using the positive constrained mass-stiffness flow (time $t = 5$, step size $s = 3$). Then, we computed the number of U-fibers intersecting each triangle of the the smoothed surface. Finally, we projected the resulting U-fiber density map from the smoothed surface onto the original GM/WM mesh. For each vertex $v_i$ on the GM/WM mesh, fiber density is computed as

$$Dm_i = \frac{\sum_{i=1}^{n_{adj}} N_{fib,i}}{\sum_{i=1}^{n_{adj}} Area_i} \tag{29}$$

where $n_{adj}$ is the number of adjacent triangles around the vertex, $N_{fib,i}$ is the number of fibers intersected with the triangle $i$ and $Area_i$ is the area of triangle $i$. Figure 51 shows an

example to compare the density maps generated with SET or not, clearly the SET method increased the coverage and connectivity of U-fibers compared to the origin maps.

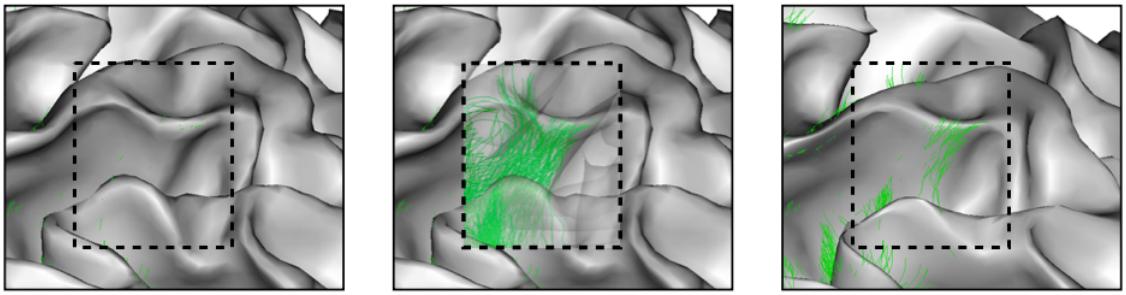


Figure 50: Example of streamlines stop below the GM/WM mesh. (a) Origin GM/WM mesh. (b) Streamlines below the GM/WM mesh. (c) Smoothed GM/WM mesh using the SET. The dotted squares show the extracted streamlines. Few streamlines arrived at the surface of GM/WM mesh in (a), while more streamlines can be seen in the less-convoluted surface from the positive constrained mass-stiffness flow in (c).

### 4.2.4 Crossing-Connectivity map: a new visualization of various U-fibers

After the extraction of different U-fibers (intra-gyral and inter-gyri) and generation of density maps, we obtained three types of U-fibers and the corresponding density maps in both CS and STS. For simplicity, here we take the U-fibers in STS as an example. For each STS, the extracted U-fibers are divided into three categories, including intra-STG, intra-MTG and inter-STG-MTG U-fibers Hence, for each vertex $v_i$, we get a U-fiber density vector

$$Vec_i = (Dm_{intra-STG,i}, Dm_{intra-MTG,i}, Dm_{inter-STG-MTG,i}) \tag{30}$$

where $Dm$ is the density value of specified U-fibers. Here we call them the "U-fiber vector".

Based on the U-fiber vector, we can classify vertices into six categories, as shown in Table 17. Here, the number "1" stands for the presence of fibers. According to the ROIs used in U-fibers extraction, we can not get vectors containing both intra-STG and intra-MTG U-fibers. However, we have vertices with U-fiber vectors showing intra-gyral U-fibers and inter-gyral U-fibers (Category 4 and 5 in Table 17). These correspond to the location of pyramid-shape crossings as defined in (Shinohara et al., 2020).

Except for the region without any types of U-fibers, the remaining categories are named as follow:

1. *intra-STG*, the region has only intra-STG U-fibers.

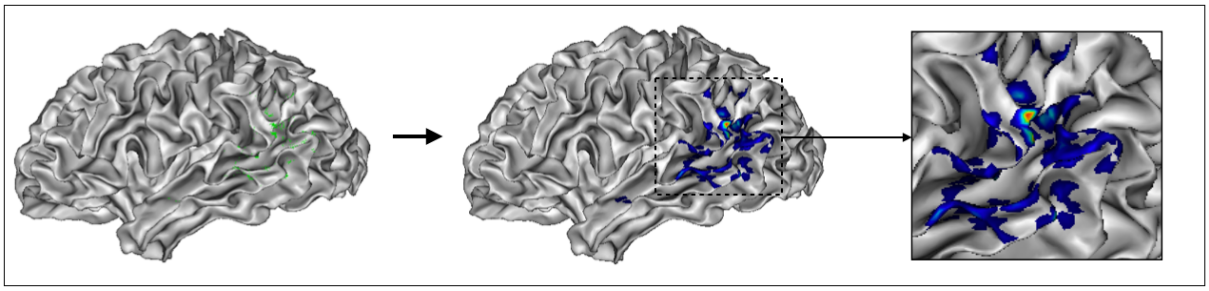

(a) density map without SET

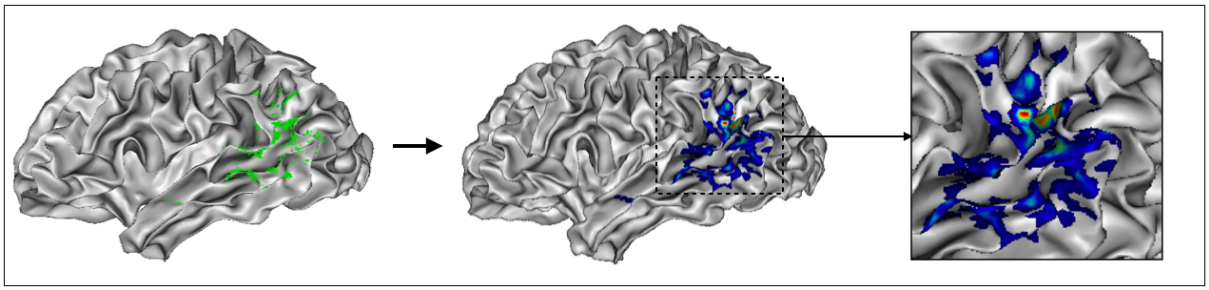

(b) density map with SET

Figure 51: Example of density maps generated with SET or not. (a) show the density map generated using the origin GM/WM mesh. (b) used the smoothing method in SET to generate a less-convoluted surface.

Table 17: Six categories of U-fiber vectors

| Category | intra-STG | intra-MTG | inter-STG-MTG |
|---|---|---|---|
| 0 | 0 | 0 | 0 |
| 1 | 1 | 0 | 0 |
| 2 | 0 | 1 | 0 |
| 3 | 0 | 0 | 1 |
| 4 | 1 | 0 | 1 |
| 5 | 0 | 1 | 1 |

2. *intra-MTG*, the region has only intra-MTG U-fibers.

3. *inter-STG-MTG*(*inter-SM*), the region has only inter-STG-MTG U-fibers.

4. *crossing Fibers STG*(*cross-FS*), the region has both intra-STG and inter-STG-MTG U-fibers.

5. *crossing Fibers MTG*(*cross-FM*), the region has both intra-MTG and inter-STG-MTG U-fibers.

There are many ways to quickly classify the U-fiber vectors into the five groups. For example, we can classify them simply following their definitions (see Figure 52(a)). This strategy is subject to noise since a single streamline can change the category of a vertex. For example, with a U-fiber vector like $(30, 0, 1)$ with one type of fibers largely dominating, we prefer to classify this case in category one when it would actually be classified in category 4. Because of this, such strategy would over-represent categories 4 and 5. Hence, a better solution is to use a clustering method. Figure 52(b) shows a clustering result using k-means (6 clusters, Euclidean distance). Note that the points with no fibers belong to the category 0 and they are not drawn in Figure 52. The result looks like an even split of the samples, a classic drawback of the k-means algorithm. Therefore, we used a kernel method to improve the clustering result. For each element of U-fiber vector $Vec_i$, we compute its logarithmic function

$$Vec'_i = \ln(Vec_i + 1) \tag{31}$$

and then apply the k-means method on the new vectors $Vec'$. The clustering result is shown in Figure 52(c). As we can see, the classification results of single type fibers in (c) are closer to the coordinate axis compared to (b), while the crossing fibers occupies the remaining position, solving the problem existing in (b). After getting the clustering results, we project them onto the GM/WM mesh (see Figure 53). This feature map shows the distribution of short-range U-fiber terminations along the cortical surface.

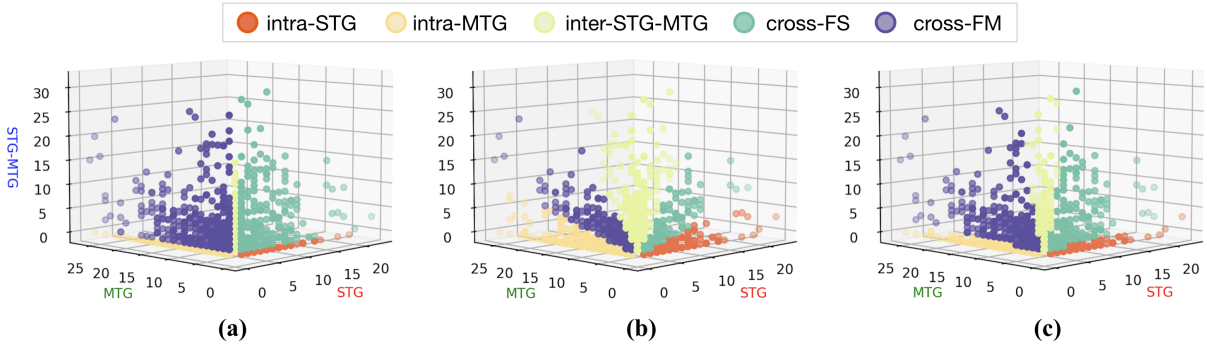


Figure 52: Three different classification results of U-fiber vectors. (a) classification using definition; (b) k-means on $Vec$; (c) k-means on $Vec'$.

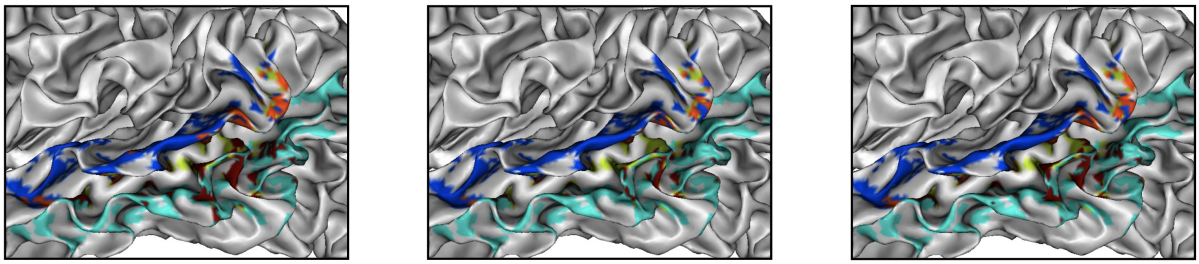


Figure 53: Feature maps generated by three different classification method. (a) classification using definition; (b) k-means on $Vec$; (c) k-means on $Vec'$. These maps are corresponding to the results in Figure 52. The correspondence between colors and regions is as follows, Blue: intra-STG; Cyan: intra-MTG; Yellow: inter-SM; Orange: cross-FS; Dark red: cross-FM.

## 4.3 Experiments and results

### 4.3.1 U-fibers termination maps

We generated the U-fibers termination maps for both hemispheres of all the 100 HCP subjects. Some examples are shown in Figure 54 and 55. As shown in these examples, the intra-STG and intra-MTG regions cover most of the area of STG and MTG respectively, while the inter-SM and cross-ROIs regions are more concentrated in the gyral junctions or wall pinches (WPs).

In order to further quantify and evaluate the relation between U-fibers connectivity and morphology, we used two surface maps *AverSampleDis* (ASD) and *SulciOrGyri* (SOG) (see Figure 34). These two maps can capture the morphological areas of interest, i.e. gyri and WPs. Moreover, the ASD maps have been successfully used in the automatic detection of PPs(Song et al., 2021). Specifically, for the feature value of ASD maps, we have $ASD(v) \in$

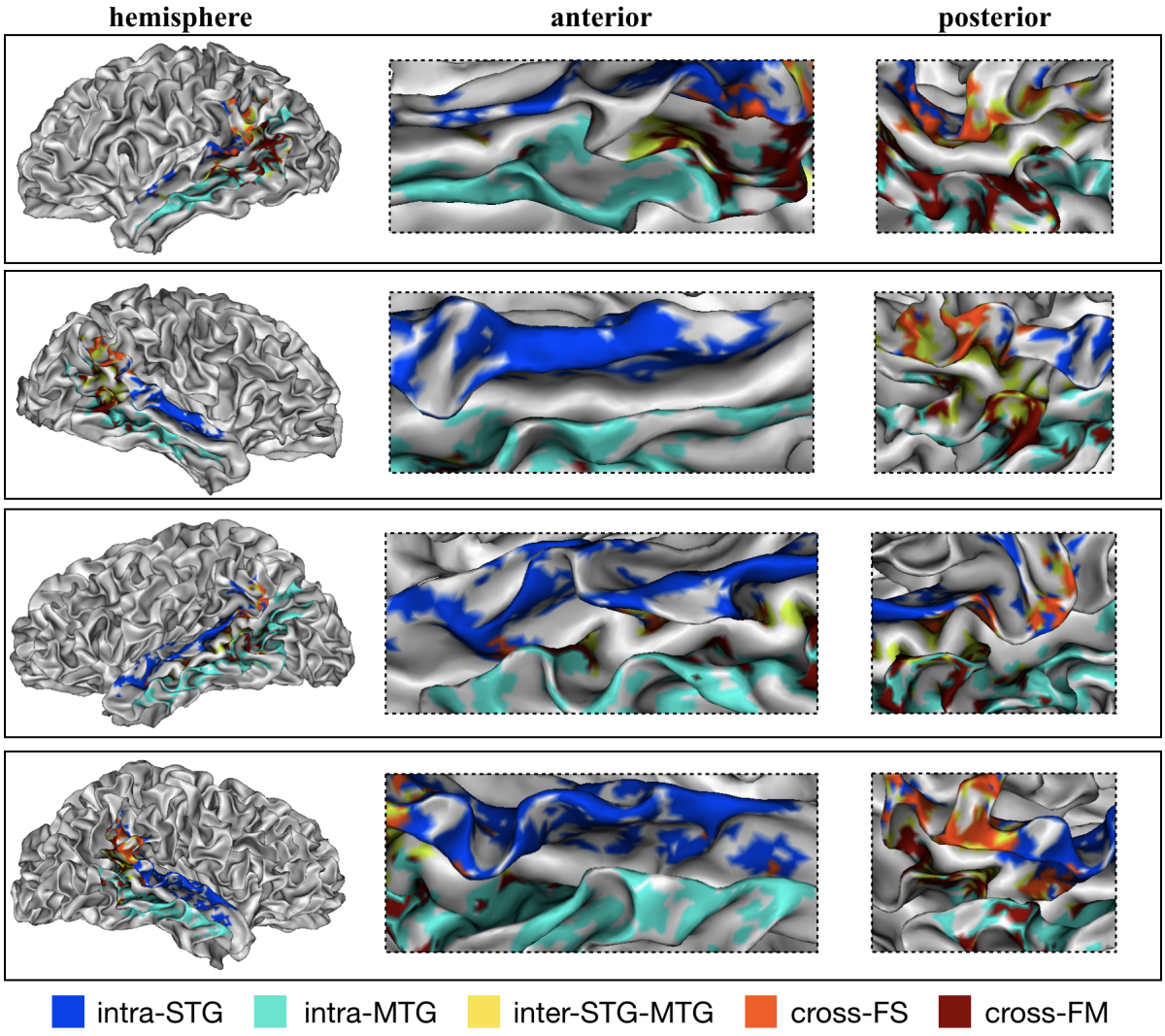


Figure 54: Examples of U-fibers termination maps in STS.

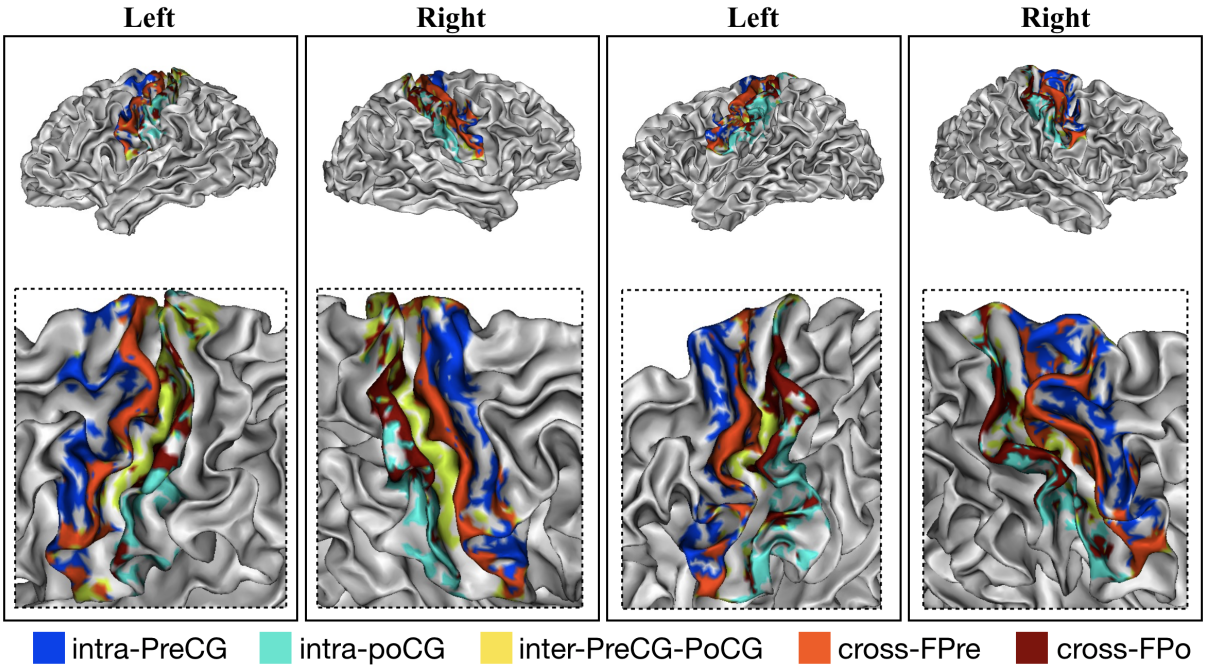


Figure 55: Examples of U-fibers termination maps in CS.

**R**, and the smaller the (negative) value of ASD, the more vertices are located in gyri crests or WPs. For the SOG maps, we have $SOG(v) \in \{0, 1\}$. The larger the value of SOG, the more vertices are located in gyri crests or WPs.

Table 18 - 21 shows the mean feature values of 5 U-fibers regions respectively on 100 subjects using three different classification methods. We also computed the mean feature value of all U-fibers regions as a comparison (the last column in table 18 - 21). The most significant values are bold in the tables. As we can see, the two crossing U-fibers regions have larger feature values than other regions both in CS and STS. In contrast, the regions of only inter-gyral U-fibers (inter-SM in STS and inter-Pre-PoCG in CS) have the lowest significant feature values.

In addition, we can see that the crossing U-fibers regions appears more at the posterior part of the STS than the anterior(see Figure 54), while this case does not exist in the CS.

### 4.3.2 PPs and their underlying U-fibers

In order to understand more about the relationship PPs and their underlying short-range U-fiber connectivity, we used the 100 HCP subjects with manually labelled PPs in the STS. This dataset has been labelled and used in (Bodin et al., 2021). We started by using the same pipeline than the one presented in (Bodin et al., 2021) (see Figure 57) to extract U-fibers associated with PPs, which consists in:

Table 18: *AverSampleDist* of 5 U-fibers regions in STS

| Methods | intra-S | intra-M | inter-SM | cross-FS | cross-FM | All |
|---|---|---|---|---|---|---|
| Default definition | -0.123 | -0.019 | 0.064 | -0.193 | **-0.203** | -0.095 |
| K-means of $Vec$ | -0.139 | -0.056 | 0.003 | -0.144 | **-0.159** | -0.099 |
| K-means of $Vec'$ | -0.132 | -0.034 | 0.034 | -0.175 | **-0.193** | -0.1 |

Table 19: *SulciOrGyri* of 5 U-fibers regions in STS

| Methods | intra-S | intra-M | inter-SM | cross-FS | cross-FM | All |
|---|---|---|---|---|---|---|
| Default definition | 0.586 | 0.484 | 0.394 | 0.654 | **0.669** | 0.557 |
| K-means of $Vec$ | 0.604 | 0.518 | 0.456 | 0.603 | **0.622** | 0.560 |
| K-means of $Vec'$ | 0.596 | 0.498 | 0.425 | 0.636 | **0.657** | 0.562 |

Table 20: *AverSampleDist* of 5 U-fibers regions in CS

| Methods | intra-PreC | intra-PoC | inter-Pre-PoCG | cross-FPreC | cross-FPoC | All |
|---|---|---|---|---|---|---|
| Default definition | -0.007 | -0.044 | 0.117 | **-0.254** | -0.221 | -0.082 |
| K-means of $Vec$ | -0.084 | -0.109 | 0.056 | **-0.235** | -0.220 | -0.118 |
| K-means of $Vec'$ | -0.021 | -0.056 | 0.111 | **-0.262** | -0.230 | -0.091 |

Table 21: *SulciOrGyri* of 5 U-fibers regions in CS

| Methods | intra-PreC | intra-PoC | inter-Pre-PoCG | cross-FPreC | cross-FPoC | All |
|---|---|---|---|---|---|---|
| Default definition | 0.470 | 0.505 | 0.349 | **0.724** | 0.688 | 0.547 |
| K-means of $Vec$ | 0.548 | 0.572 | 0.414 | **0.709** | 0.683 | 0.585 |
| K-means of $Vec'$ | 0.485 | 0.518 | 0.357 | **0.732** | 0.695 | 0.557 |

- manual identification of PPs (see section 3.3.3) as lines joining the MTG and STG gyral crests via WPs.
- at the intersection between each PP and the two gyral crest lines, define two disk like seeds with a given radius. This radius will be varied from 8 to 16mm as a parameter of the process.
- for each PP, extract streamlines from the tractogram that start and end in the associated PP seeds, and whose length is half of the PP length, and less than three times that length.
- count the number of streamlines associated to each PP for a given seed size.

We nevertheless added an additional constraint by selecting the subset of U-fibers that go from STG to MTG, using gyral seeds as defined in the previous section. The reason for such filtering is the fact that using the original algorithm in (Bodin et al., 2021), when PP seeds were large enough to overlap (see Figure 56), some very short streamlines fully included in the seeds intersection are extracted even though they are not joining the two gyri. By

explicitly selecting only fibers going from one gyrus to the other, such short streamlines are filtered out.

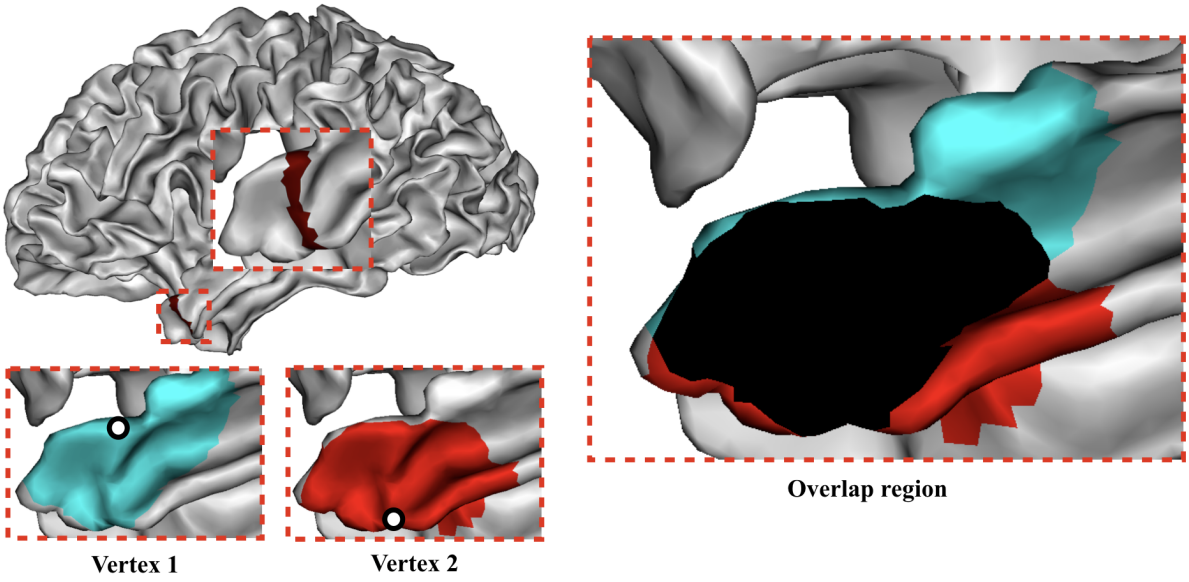


Figure 56: The overlap of two PPs seeds in (Bodin et al., 2021). Seed size = $16mm$.

The results of the quantitative analysis of the U-fiber count underlying PPs are shown in Figure 59. The PPs were classified as "superficial" or "deep" if their DPF was below or above 0.42 respectively (Bodin et al., 2021). We studied U-fibers with length between 10 and $60mm$. As we can see from Figure 59, the proportion of extracted U-fiber streamlines from superficial and deep PPs is similar among all PPs seeds both in left and right hemi-spheres. And the number of U-fibers underlying deep PPs is greater than superficial PPs, which is different from the results in (Bodin et al., 2021). In our observation, this is due to the fact that we filtered out the excess fibers in the intersection between PP seeds, but not joining the gyral seeds. The geometry of the superficial PPS is more likely to let that happen, which might explain the results (see Figure 43). These short fibers that were filtered out are either real or artefactual.

To further investigate the relationship between PP morphology of and underlying U-fibers, we divided the U-fibers into two groups. For each PP line, we selected the three vertices located in the middle and set 3 spheres of radius 3.5mm centered on these vertices (see Fig. 60(a)).We then selected U-fibers that pass through these spheres (Type 1), and those that do not (Type 2). Type 1 fibers are clearly following the entire PP trajectory (from one extremity to the other via the middle points), while Type 2 fibers might be following a different trajectory between their two extremities. Several examples are shown in Figure 60(b) and a quantitative analysis is presented in Fig. 61: we plot each PP (deep

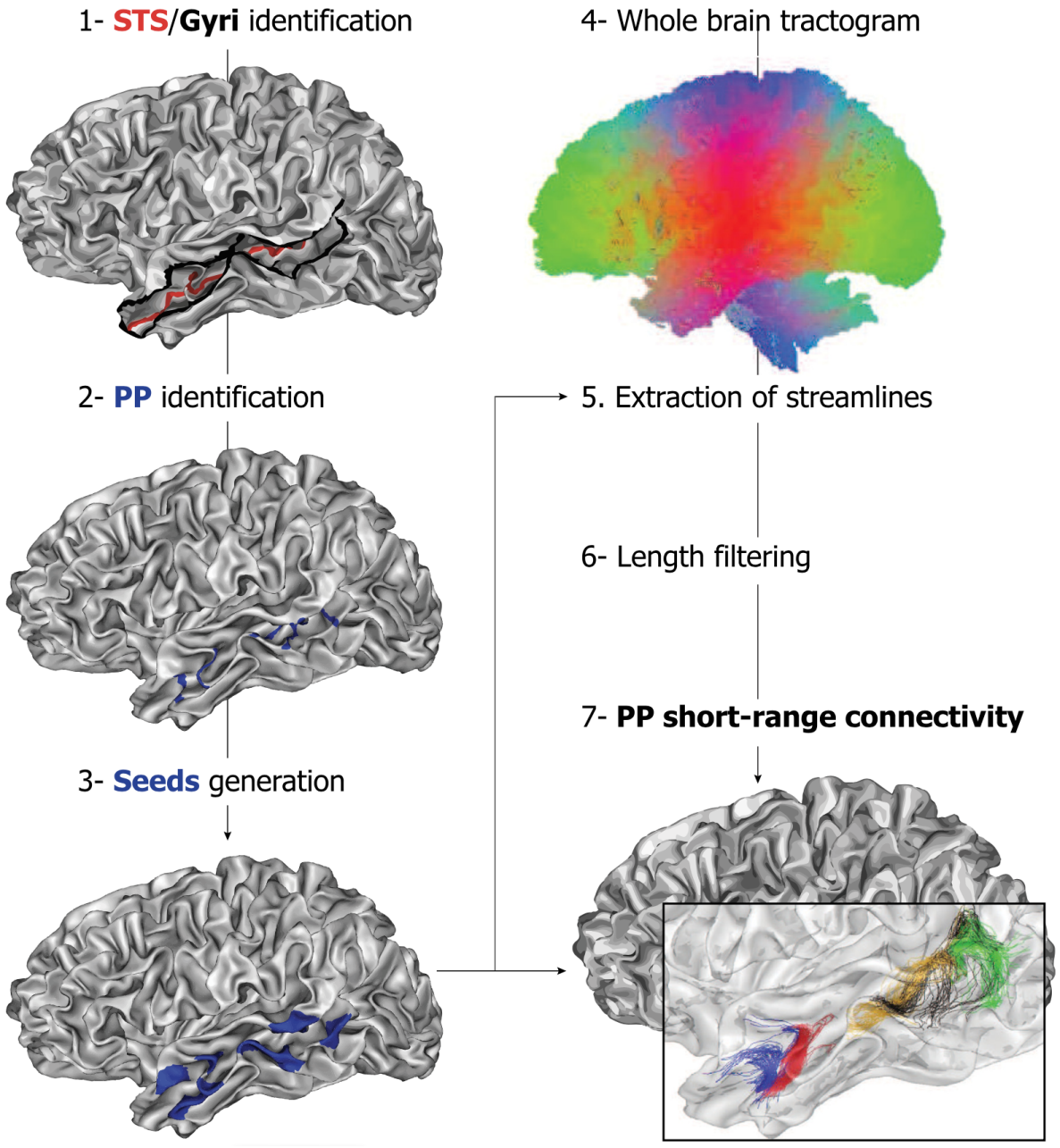


Figure 57: Analysis pipeline for U-shape fibers extraction illustrated for one subject in the left hemisphere. Delimited in length by the STS and in width by the adjacent gyri (1), all PPs are manually identified and drawn (2) on the individual's surface. Their extremities are used as seeds (3) to extract the underlying short-range connectivity (7). Each colored bundle corresponds to the streamlines extracted from one pair of seeds (one PP). Figures adapted from (Bodin et al., 2021).

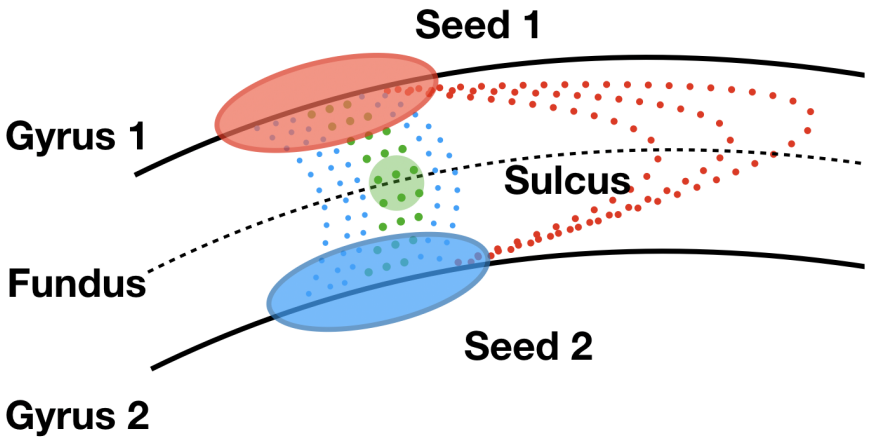


Figure 58: A schematic of various U-fibers extracted using the pipeline in (Bodin et al., 2021). The green circle shows a middle area of the PP line. The green dotted curves are the U-fibers crossing through the middle area of PP. The red dotted curves are the long-range U-fibers extending along the sulcus. The blue dotted curves are the U-fibers near the PPs lines.

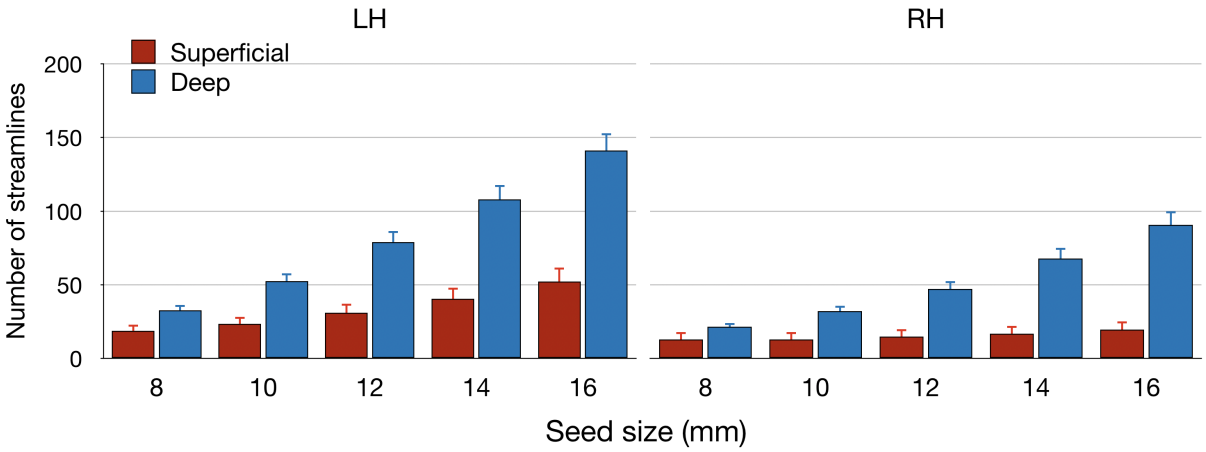


Figure 59: Proportions of U-fiber streamlines found below superficial PPs (red), deep PPs (blue) in the left (LH) and right (RH) hemisphere. X-axis indicates the different surface seed sizes used to extract streamlines (in mm). Errors bars illustrate the standard error of the mean (SEM).

or superficial) with coordinates corresponding to the number of Type 1 and Type 2 fibers.

It is very visible that superficial PPs have more Type 2 fibers than Type 1. It suggests that their associated U-fibers might not all follow the PP trajectory in superficial white matter, or pass deeper in white matter. On the other hand, seep PPs seem to show more fibers following their trajectory in superficial white matter (see illustration in Fig. 60(b)).

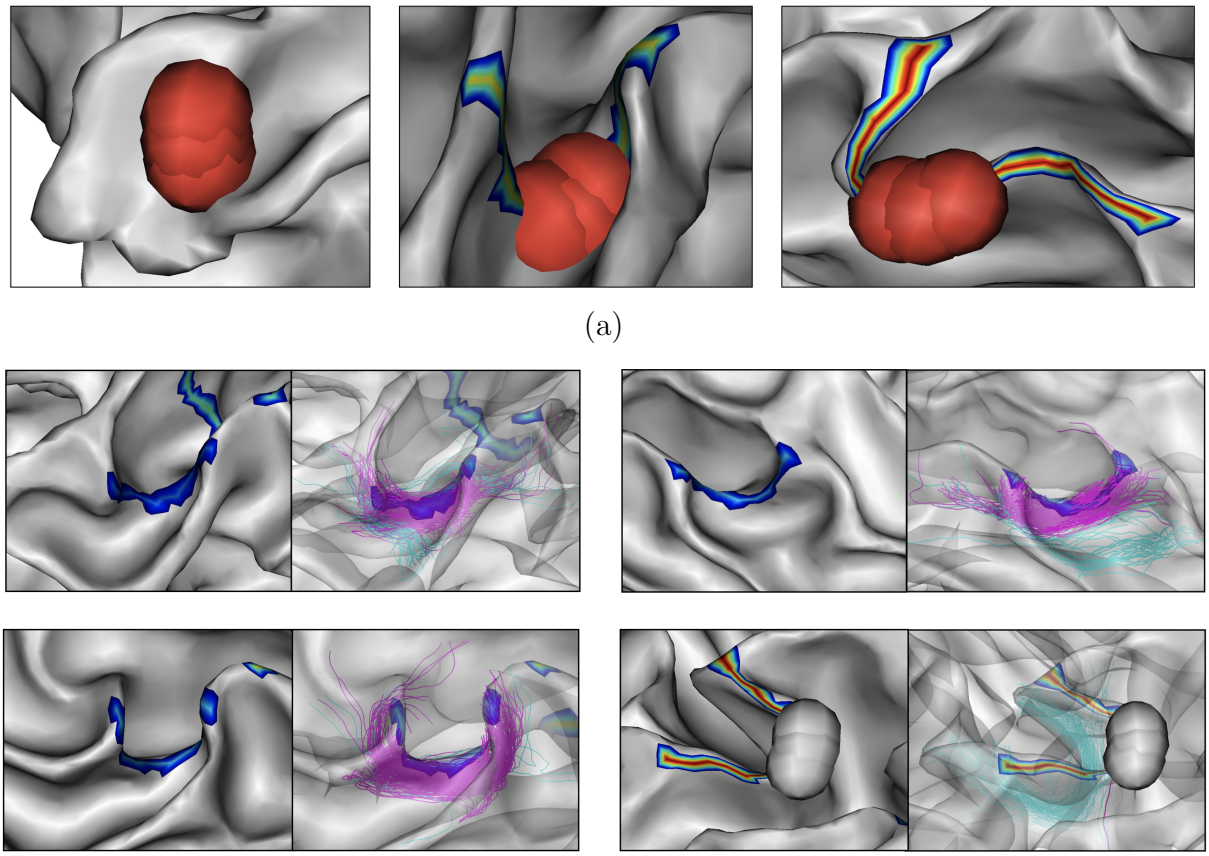

(a)

(b)

Figure 60: Examples of spherical filters and extracted U-fibers. (a) Spherical filters generated using the central three vertices of PPs lines. The radius of each sphere is $3.5mm$. (b) Extracted U-fibers: the pink streamlines are Type 1 and the blue are Type 2.

The above results show that not all extracted U-fibers underlying PPs follow the exact pathway of PPs lines through the sulcal bottom and a lot of them are just terminated near the location of PPs seeds. It should be noted that all underlying PPs U-fibers are the inter-gyral U-fibers, and more U-fibers away from the PPs were extracted when we increased the seed size. Imagine that the area with larger seed size will inevitably cover more flat regions of gyral walls, and these U-fibers outside the PPs are more likely to terminate in these flat regions, which may correspond to the regions with only inter-gyral U-fibers in section 4.3.1. Therefore, although there is a correlation between PPs and their underlying

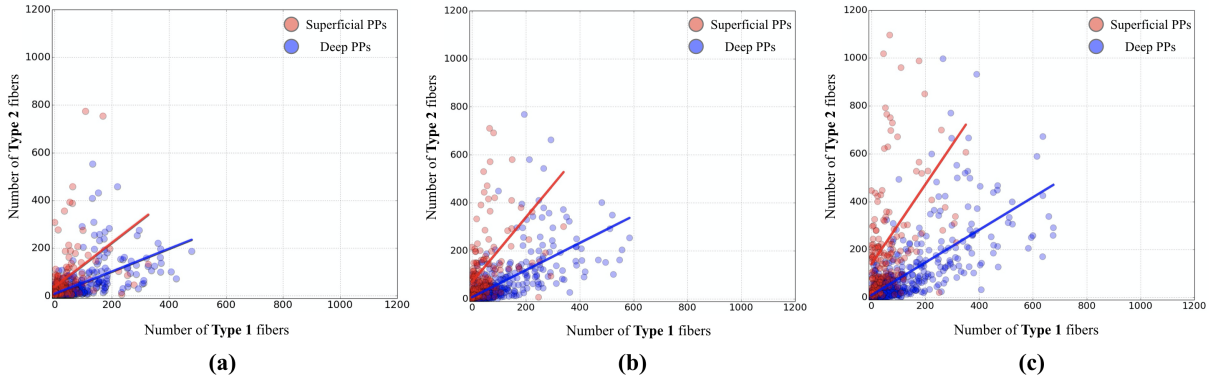


Figure 61: Distribution of extracted U-fibers for all the PPs (Superficial PPs in red, Deep PPs in blue) with different seed size: (a) $12mm$; (b) $14mm$; (c) $16mm$. Each point corresponds to a PP. The linear regressions of these points was computed to show the overall proportion of U-fibers pass through or outside the filter.

inter-gyral U-fibers, the trajectory of these fibers alone is not enough to explain the shape of PPs.

### 4.3.3 PPs: the termination of intercrossing short-range U-fibers

As mentioned in previous sections and literatures (Song et al., 2021; Bodin et al., 2021), the WPs, particularly pairs of WPs in adjacent gyri, have been used as specific morphological characteristics to identify the PPs (see Figure 26, 27, 34). In order to investigate further the relationship between PPs, WPs and short-range U-fiber connectivity, we first extract the WPs using their morphology and divide them into two groups according to whether they contained manually labelled PPs or not. We then propose a quantitative statistical analysis in order to understand the difference between cortical regions with crossing U-fibers and those with only inter-gyral U-fibers.

#### "Wall pinches" extraction

Figure 62 shows the pipeline we used to extract the WPs on the cortical surface using the morphological feature maps. As the WPs are distributed within the STS, we first generate gyral masks for STG and MTG that cover only the inner gyral walls (see Fig. 62(A)). In order to separate the WPs and gyral crests, we dilate the gyral crests lines (to a geodesic distance of 4 mm) on the cortical surface to get the gyral crests regions. Then we substract the gyral crest regions from the gyral masks (Figure 62(B)) in order to get only the inner walls of the sulcus. The intersection of the resulting mask with the SOG feature map is then computed in order to get the location of the WPs on the inner wall of the sulcus (see Fig. 62(E)). At this stage, we get all the vertices in WPs and we need to divide them into

several WPs (Figure 62(E) right). Thus, we use the DBSCAN clustering method to classify the vertices into WPs and remove the anomalous vertices at the same time. The DBSCAN algorithm can be abstracted into the following steps (Schubert et al., 2017):

1. Find the points in the small neighborhood ($\epsilon$) of every point, and identify the core points with more than a specific number of neighbors ($min_{points}$);

2. Find the connected components of core points on the neighbor graph, ignoring all non-core points;

3. Assign each non-core point to a nearby cluster if the cluster is an $\epsilon$ neighbor, otherwise assign it to noise.

For the DBSCAN used in our experiments, we have $\epsilon = 2mm$ and $min_{points} = 4$.

Finally, from the resulting WP regions, we select those that are intersected with the manually labelled PPs lines. As illustrated in Fig. 63, manually labelled PPs correspond to the presences of paired WPs on both adjacent gyral walls (STG and MTG), as defined in (Bodin et al., 2021). It is interesting to note that we extracted more WPs than the number of manual labelled PPs (Mean 20.9 to 5.5). Some PPs are clearly associated with paired WPs (Figure 63-top), while some WPs are located in relatively flat areas with no PPs (Figure 63 bottom).

At this stage we extracted the WPs of the STS that are associated with a PP, and in the following section, we study the nature of these PPs.

### Connectivity and "Wall pinches" location

As we discussed in section 4.3.1, the regions with crossing U-fibers are largely related to the WPs but their relationships with PPs needs further studying. Therefore, our study focuses on the relationship between WPs and crossing U-fibers regions, as opposed to regions with only inter-gyral fibers. In the following, we quantitatively compare WPs and connectivity regions by estimating their overlap. For this, we choose the statistical coefficient *Jaccard index* (Jaccard, 1912) used for gauging the similarity and diversity of sample sets.

Given two finite sample sets $X$ and $Y$, the *Jaccard index* is defined as the size of the intersection divided by the size of the union of the sample sets,

$$J(X,Y) = \frac{|X \cap Y|}{|X \cup Y|} \tag{32}$$

If $X$ and $Y$ are both empty, the Jaccard is equal to 1. Here, the samples of each set are the vertices on the cortical surface, namely the sample set $X = \{v_1, v_2, \ldots, v_m\}$. On

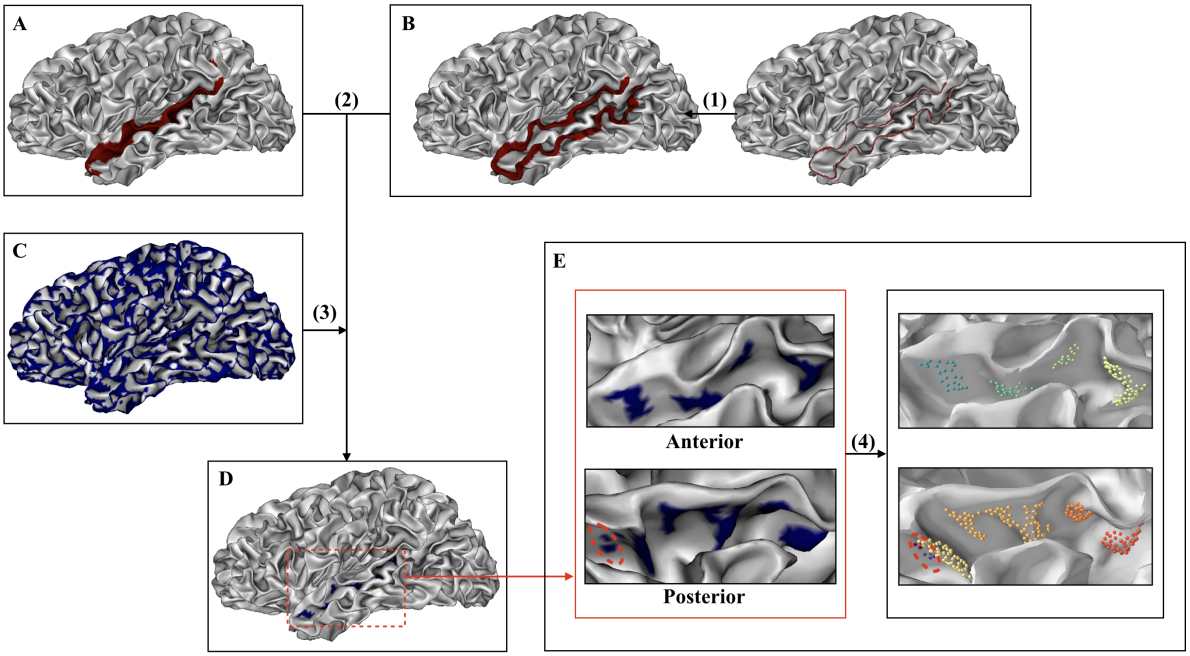


Figure 62: The pipeline of WPs extraction. This figure show an example in STG of the left hemi-sphere. (A) Mask of STG; This mask covers only the inner gyral wall of the STS. (B) Gyral crest regions generated by expansion of gyral creat lines. (C) SOG feature maps. (D) Extracted WPs. (E) Post-processing of WPs from (D). STEP: Here we use the set operations to represent the region operations, where the set name is the image reference $(A, B, C, D)$ (1) Expansion of gyral crest lines, the distance is $4mm$. (2) Discard the gyral crest regions: $A - B$. (3) Extract the WPs: $D = C \cap (A - B)$ (4) Classify and remove the outliers by DBSCAN method. The red dotted circle marks the small noise regions.

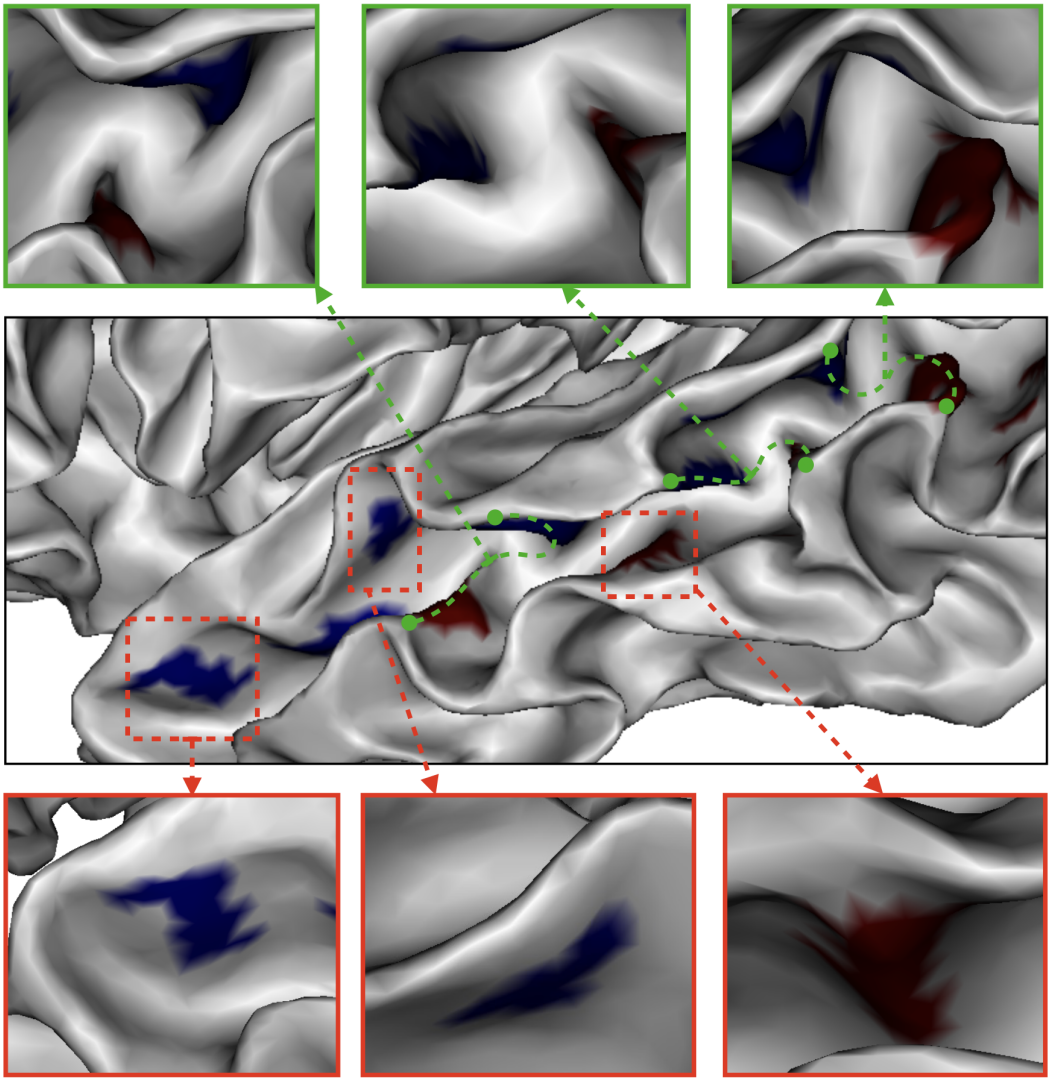

Figure 63: Examples of WPs extracted by our method in STG (blue) and MTG (red). The green dotted curves show the manual labelled PPs lines, and the top figures show the paired WPs on STG and MTG. The red dotted boxes show the WPs without PPs.

top of measuring the overlap between WPs and connectivity-defined regions, we also define the coverage of these regions (*Regs*) as the proportion of WPs that are intersected by a connectivity region, as follows:

$$Coverage(WPs, Regs) = \frac{|WPs \cap Regs|}{|WPs|} \tag{33}$$

where $|WPs|$ is the number of extracted WPs (instead of the number of surface vertices), and $|WPs \cap Regs|$ is the number of WPs intersecting with U-fibers regions.

These coefficients were computed for connectivity regions with crossing-fibers, as well as for regions with inter-gyral fibers only. Coefficients were computed for the subjects, both left- and right-hemispheres. Results are shown in Fig. 64.

For both two coefficients, crossing U-fibers regions get significantly better results ($p < 0.05$; Wilcoxon signed-rank test) than regions with only inter-gyral regions. Mean values are: *Coverage*: $79\% > 65\%$; *Jaccard index*: $0.171 > 0.096$.

This indicates WPs are preferably associated with regions of crossing U-fibers than regions with inter-gyral U-fibers alone. These results are consistent with those of (Shinohara et al., 2020) that presents 3-way gyral junctions (i.e. WPs) as convergence points of intra- AND inter-gyral short range U-fibers. It further supports the hypothesis that PPs are defined with WPs that are regions of high density of intercrossing U-fibers termination.

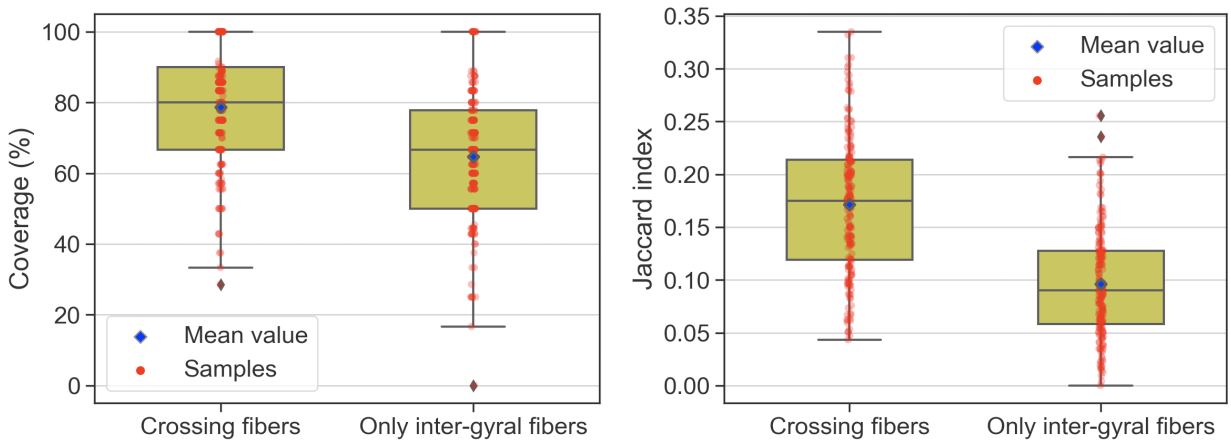


Figure 64: The comparison of crossing U-fibers regions and regions with only inter-gyral fibers. The red points are the coefficients of left- or right-hemispheres.

## 4.4 Automatic detection of PPs using connectivity maps

### 4.4.1 EnsSVM with conectivity maps

In section 4.2 and 4.3, we proposed a method to generate the connectivity maps of different short-range U-fibers and studied their relationships with the PPs. Quantitative and statistic analyses show that the PPs are located preferably in regions of high density of intercrossing U-fibers terminations. Therefore, based on our successful experience of automatic detection of PPs using an EnsSVM on morphological feature maps (section 3.8.1), in this section we train an EnsSVM models using the connectivity maps of U-fibers terminations (Connectivity EnsSVM) using the same HCP dataset. The main steps of training the EnsSVM are as follows: First, we generate the density maps of intercrossing U-fibers. Then, we generate feature images by using cortical surface profiling. Finally, the EnsSVM is trained on these feature images. The performance of EnsSVM using density maps were shown in Table 22 - 24. Here, we used the $10 \times 10$ nested cross-validation to train the models and select the optimal parameters. The Gaussian radial basis function(RBF) was selected as the kernel function for all based SVM classifiers. The results are compared with an EnsSVM models trained on ASD feature maps.

Table 22: The average value of model performance measures

| Feature maps | Recall | G-mean | F-measure | AGF |
|---|---|---|---|---|
| *ASD* | 0.811 | 0.773 | 0.527 | 0.774 |
| *Connectivity* | 0.720 | 0.598 | 0.347 | 0.623 |

Table 23: Prediction results with ASD and Connectivity (%)

| Feature maps | PPs | Non-PPs | Superficial PPs | Deep PPs |
|---|---|---|---|---|
| *ASD* | 81.1 | 73.7 | 92.4 | 79.0 |
| *Connectivity* | 72.0 | 49.7 | 68.2 | 73.4 |

Table 24: The accuracy of PPs in different depth ranges (%)

| Feature maps | $d \in [0, 5]$ | $d \in (5, 10]$ | $d \in (10, 15]$ | $d \in (15, 20]$ | $d \in (20, +\infty]$ |
|---|---|---|---|---|---|
| *ASD* | 91.5 | 82.8 | 80.5 | 79.4 | 78.5 |
| *Connectivity* | 59.1 | 77.4 | 77.0 | 73.0 | 71.5 |

As can be seen from the results, the connectivity maps of crossing fibers performed worse than the ASD maps. In particular, it did not predict well for non-PPs (49.7%), superficial PPs(68.2%) and PPs with depth $\in [0, 5]mm$ (59.1%). The fact that the connectivity EnsSVM perform worse on the non-PPs samples than PPs is understandable: there is little crossing U-fibers regions over flat gyral walls with no WP, leading to feature images containing hardly any information for non-PPs. However, the poor prediction results on the

superficial PPs with depth $\in [0, 5]mm$ attract our attention. It indicates a low density of crossing U-fibers underlying superficial PPs. Moreover, the number of inter-gyral U-fibers underlying superficial PPs is lower than for deep PPs (see Figure 59). In the next section, we investigate the variability of the density of U-fibers in the STS.

### 4.4.2 Connectivity heterogeneity in the STS

To further investigate the location of PPs and the density of fibers, we first generate a region around each PP, with a dilation of the PPs lines (distance = $2.5mm$). Here again, we use the superficial and deep PP lines that were drawn in (Bodin et al., 2021). Each of these PP line has an intersection with the STS fundus, and this fundus is parameterized between 0 (anterior extremity) and 100 (posterior extremity), hence providing a normalized localization (coordinate) of each PP between the two extremities of the sulcus (see (Bodin et al., 2021)). Figure 65 shows their distribution along the STS coordinates, where 0 represented the anterior extremity and 100 the posterior extremity of the STS fundus (Bodin et al., 2018).

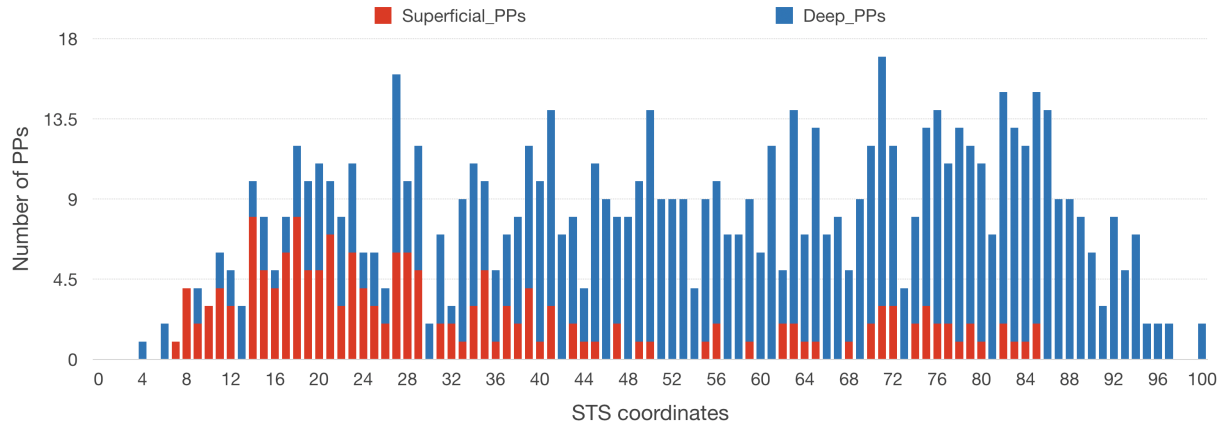


Figure 65: Distribution of PPs along the STS.

As visible, superficial PPs are located preferentially in the anterior part of the STS, while the deep PPs are located more towards the posterior part. This heterogeneity of distribution of the two types along the STS might have some consequences on the quality of the connectivity features associated to both types of PPs.

We then extract and count the U-fibers (intra- and inter-gyri) terminating in these PP regions with length between 10 and 60mm (Figure 66). For each fiber with a termination in a PP area, we find the other termination and we classify the fiber depending on where is that termination: same PP region, elsewhere in the STG, elsewhere in the MTG, or outside the STS. For this classification we used the same ROI that were defined in section 4.2. Figure 67 shows the average number of streamlines associated to PPs at each position along the

STS.

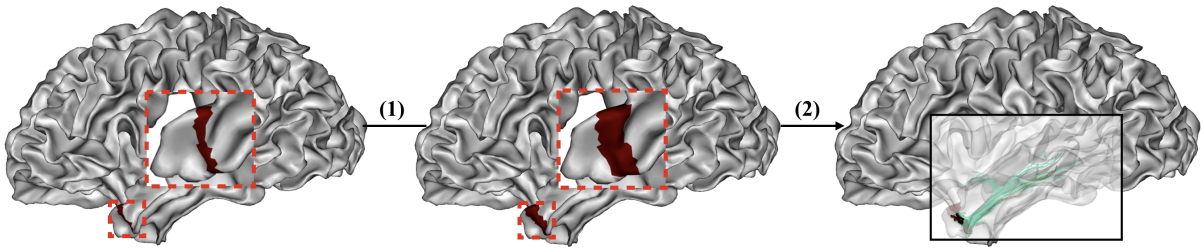


Figure 66: Extraction of the streamlines of fibers in the expanded PPs areas. (1) Generate the expansion area of PPs lines, the distance is $2.5mm$. (2) Extract the fibers with length between 10 and $60mm$. Here, we used the same ROIs as in section 4.2.

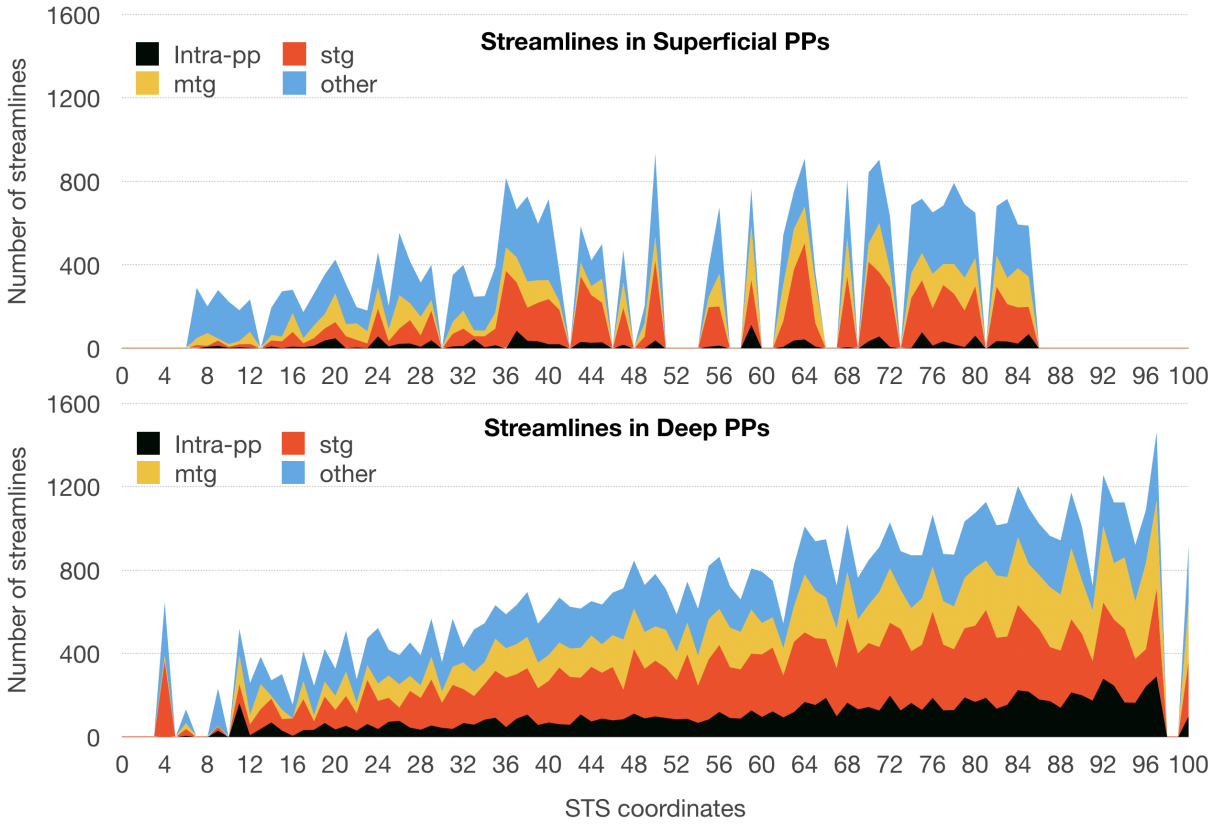


Figure 67: Average number of streamlines along the STS.

It is visible that when going from the anterior (coord. 0) to the posterior (coord. 100) extremities, the number of stremlines increases. This is the case for fibers associated to deep PPs, and one could think that it is related to the lower number of deep Pps in the anterior part of the sulcus, but this is actually also the case for streamlines associated to superficial PPs, despite the fact that these PPs are more numerous in the anterior part. We can conclude that there is a general lower number of intra- and inter-gyral U-fibers

streamlines in the anterior part of the sulcus, increasing as one moves towards the posterior part.

This heterogeneity of connectivity along the STS is probably impairing the performances of the EnsSVM trained on connectivity maps. So, although there is a correlation between PPs and U-fiber connectivity, using connectivity maps alone it is difficult to identify all PPs in the STS. In the next section, we investigate the possibility to use another marker of fiber termination density in order to attempt to overcome the streamline heterogeneity along the STS. We introduce the use of *myelin maps*, computed as the ratio of T1w/T2w image intensities (Glasser and Van Essen, 2011).

## 4.5 Myelin maps

Myelin is a fatty substance that forms a protective layer around axons and enhances axonal conductance (Heath et al., 2018; van der Weijden et al., 2020). A myelin map, actually a proxy of myelin content, can be derived from the MR signal intensity of a T1-weighted (T1w) image normalized (divided) by a T2-weighted (T2w) image registered into the same space. It has been found that spatial distribution of signal intensities from this map co-localise with myelin-stained histology of the cortex (Glasser and Van Essen, 2011). This method of myelin mapping was shown to delineate boundaries of cortical areas in population-average maps as well as individual subjects, albeit with less precision. The benefit of this approach is that the structural images typically acquired in a routine MR exam (i.e. for segmentation, registration, and screening of incidental findings) can also be used to estimate myelin content. It is also possible to get very high resolution images ($\sim 1mm$ cubic) in a reasonable scan time. This may be important for looking at cortical myelination, rather than WM, where higher resolution is necessary to accurately delineate the folded cortical surface. A detailed review of studies investigating correlations of biological features with cortical myelin mapping can be found in (Glasser et al., 2014). Moreover, higher SWM iron concentrations were observed in U-fiber–rich frontal, temporal, and parietal areas, potentially reflecting high fiber density or late myelination in these areas (Kirilina et al., 2020), which means U-fibers are associated with high myelin, and an increase of the density of U-fiber terminations can be expected to increase values in the myelin maps. Therefore, if WPs are linked with a high density of U-fiber terminations, myelin maps should help to localize them.

In this section, we first introduce the method we used to generate myelin maps. Then a statistical analyses of the link between myelin and morphology maps is performed. Finally, we train an EnsSVM using myelin maps and discuss the prediction results.

### 4.5.1 Myelin map generation

On the same HCP dataset that we used for U-fibers extraction, myelin maps are computed as follows for each subject:

1. Preprocessing of T1 and T2 images: the T1 and T2 images are denoised, bias-corrected (N4), and coregistered rigidly using the ANTS software.

2. Division between T1 and T2 images: we use *fslmaths* (https://fsl.fmrib.ox.ac.uk/fsl/fslwiki/FSL) to divide the two images voxel-by-voxel.

3. Project 3D volume T1/T2 images to white matter (WM) mesh for each individuals using the Brainvisa (BV) software (http://brainvisa.info). Note that we exclude the cingular pole in this step.

Figure 68 shows some examples of myelin maps we generated for the HCP subjects of left- and right-hemispheres. As we can see, the WPs seem to have a higher myelin content, which may fit with our prior hypotheses that the myelin maps should help to localize the WPs. Also the gyral crests have a higher myelin content, in order to further investigate the relationships between myelin maps and STS morphological features such as WPs, we computed the Pearson correlation coefficient (PCC) between myelin maps and ASD maps in different regions for all subjects.

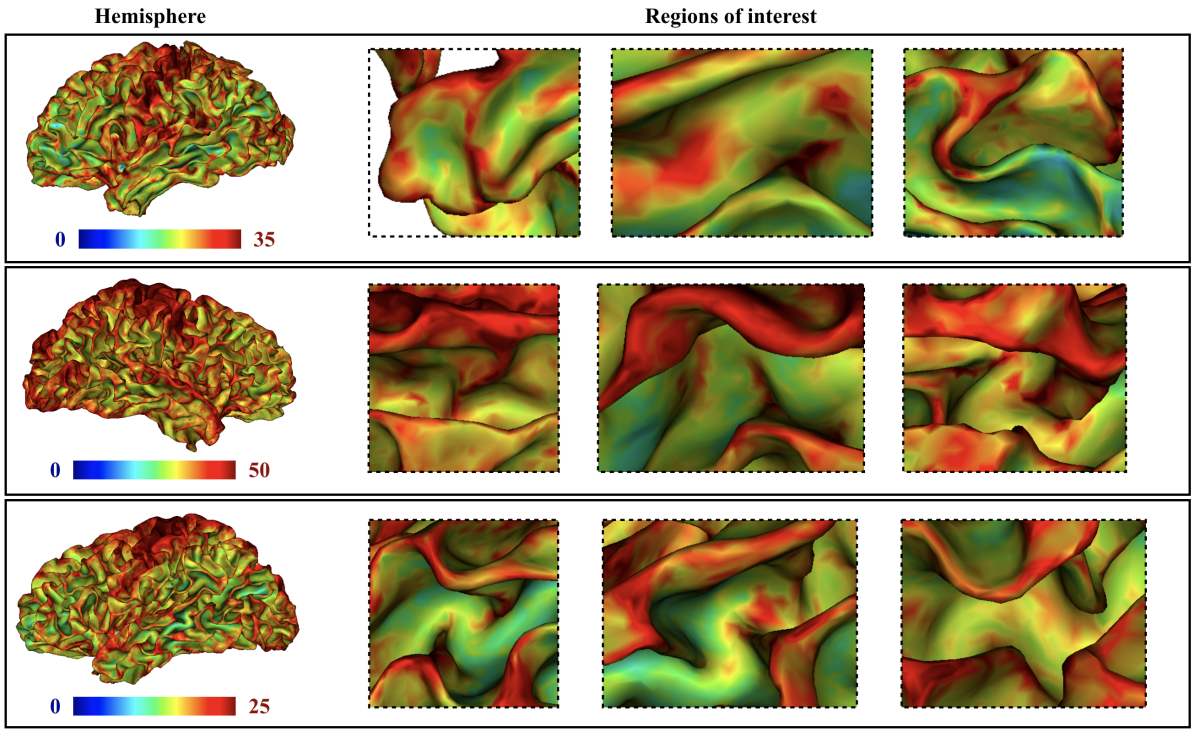


Figure 68: Examples of myelin maps. From blue to red represents an increase in the value of myelin maps.

As shown in Table 25, we selected three regions: the cortical surface (exclude the cingular area); STG and MTG gyral walls in STS; STG and MTG gyral crests regions. Here, the gyral crests regions are the regions in Figure 62 (B). The gyral walls are generated using the inside vertices in STS of gyri masks (shown in Figure 62 (A)) and remove the gyral crest regions (B).

As we can see from the results in Table 25, there is a very significant correlation for the whole cortical surface, which means the link between morphology as depicted by ASD

and mylein content. However, the correlation is low. This is probably due to the fact that myelin content has strong variations depending on regions. For instance as can be seen on Figure 68, the motor cortex (and primary areas in general) has a very high myelin content but the temporal lobe has a rather low myelin values.

For the region of gyral walls, we got a higher and very significant correlation compare to the other two regions. This is consistent with what we observed in Figure 68. Moreover, since the ASD can indicate the presence of WPs (Song et al., 2021), it would mean that variations of myelin indicate the presence of WPs.

Table 25: The PCC of myelin and ASD maps

| Brain areas | Mean PCC |
|---|---|
| Cortical surface (exclude the cingular area) | -0.373 $(*)$ |
| STG, MTG walls | -0.509 $(*)$ |
| STG, MTG gyral crests($4mm$) | -0.432 $(*)$ |

$(*)p < 0.0001$

### 4.5.2 Automatic detection of PPs using myelin maps

In the same way as the connectivity maps, we trained an EnsSVM model with the myelin maps (MYL). Its performance are shown in Table 26 - 28. Here, we used the $10 \times 10$ nested cross-validation to train the models and select the optimal parameters. The Gaussian radial basis function(RBF) was selected as the kernel function for all based SVM classifiers. Also, we take the EnsSVM models using ASD feature maps as a comparison.

As shown in Table 26, the EnsSVM models trained with myelin maps shows slightly worse results than the connectivity maps in terms of performance. Prediction results (Table 27) are also similar for PPs and non PPs. But, it should be noted that the prediction performance is higher for myelin maps than connectivity maps for superficial PPS ($82.8\% > 68.2\%$). On the other hand, for deep PPs it is the opposite ($65.5\% < 71.5\%$). Also, as shown in Table 28, the MYL perform better for the PPs with depth between 0 and $10mm$.

Unfortunately, neither model can accurately predict the non-PPs (49.7% and 41.2%) and they do not compare with ASD-based EnSVM that performs better in almost all categories. It appears to be that the connectivity maps cannot detect superficial PPs and non-PPs, while MYL cannot detect the deep PPs and non-PPs.

Table 26: The average value of model performance measures

| Feature maps | Recall | G-mean | F-measure | AGF |
|---|---|---|---|---|
| *ASD* | 0.811 | 0.773 | 0.527 | 0.774 |
| *Connectivity* | 0.720 | 0.598 | 0.347 | 0.623 |
| *MYL* | 0.712 | 0.542 | 0.314 | 0.580 |

Table 27: Prediction results with ASD, connectivity and myelin maps (%)

| Feature maps | PPs | Non-PPs | Superficial PPs | Deep PPs |
|---|---|---|---|---|
| *ASD* | 81.1 | 73.7 | 92.4 | 79.0 |
| *Connectivity* | 72.0 | 49.7 | 68.2 | 73.4 |
| *MYL* | 71.2 | 41.2 | 82.8 | 65.5 |

Table 28: The accuracy of PPs in different depth ranges (%)

| Feature maps | $d \in [0, 5]$ | $d \in (5, 10]$ | $d \in (10, 15]$ | $d \in (15, 20]$ | $d \in (20, +\infty]$ |
|---|---|---|---|---|---|
| *ASD* | 91.5 | 82.8 | 80.5 | 79.4 | 78.5 |
| *Connectivity* | 59.1 | 77.4 | 77.0 | 73.0 | 71.5 |
| *MYL* | 85.0 | 86.5 | 67.8 | 67.4 | 61.1 |

## 4.6 Discussion

### 4.6.1 Intercrossing fibers, 3-hinged gyri and "wall pinches"

In this chapter, we studied the PPs from the point of view of connectivity, particularly the connectivity of short-range U-fibers. In fact, few studies have correlated the morphology of PPs and U-fibers connectivity (Bodin et al., 2021; Pron et al., 2021). Bodin et al. (2021) proposed that PPs are short-range U-fiber connectivity pathways, and studied the high density of U-fibers underlying PPs in the STS. Pron et al. (2021) found an overlap between a cluster of dense U-fibers and the location of PPFM in CS. Both studies revealed some correlations between PPs and connectivity of U-fibers, while one limit they have in common is that they only extracted the inter-gyral U-fibers that connect the adjacent gyri. In this study, we studied different types of U-fibers (inter-gyral and intra-gyral U-fibers) simultaneously. Our results suggest that the WPs associated with PPs are regions where intercrossing U-fibers terminate, rather than the pathways connecting the adjacent gyri. This is similar to what was suggested in the dissection study presented in (Shinohara et al., 2020).

Actually, similar results have been shown in (Li et al., 2010; Ge et al., 2018; Zhang et al., 2020a,b) where they defined regions named "cortical 3-hinges" or "3-hinge Gyri" based on their morphology. These 3-hinge gyri have a striking similarity with the 3-way junctions defined in (Shinohara et al., 2020), and both type of landmarks seem to correspond to the intersection between gyri and wall pinches (see Figure 48 (b)). A strong structural

connectivity was found in these 3-hinges areas. Both PPs and 3-hinge gyri are defined from the brain morphology. Shinohara et al. (2020) also defined 3-way junctions from morphological observations and found they correspond to the convergence area of intra- and inter-gyral short range fibers, leading to the definition of "pyramid-shape crossings". As mentioned, in fact, it seems that although defined in different nomenclatures, 3-way junctions (Shinohara et al., 2020), 3-hinge gyri (Li et al., 2010), and wall pinches/PPs are actually referring to similar structures and that they have a link with the underlying connectivity.

### 4.6.2 Local connectivity networks underlying the PPs in STS

If we admit that WPs/PPs are the same objects, and that they are the convergence areas of inter- and intra-gyral U-fibers, an interesting hypothesis has been proposed by Shinohara et al. (2020) based on observations during Klingler's dissections. They propose that 3-way junctions are the hubs of local short-range connectivity networks around sulci, with longer fibers coursing deeper within white matter to connect junctions that are further away from each other. This hypothesis is illustrated in 69. For inter-gyral U-fibers, most short U-fibers cross through the STS along the PPs lines, while the longer ones cross through the STS under the short fibers and span over several location of PPs. Intra-gyral U-fibers pave the gyral walls and connect two close location of PPs in the same side.

So if WPs are considered as nodes a local network of structural connectivity based on these nodes could emerge. Detecting WPs/PPs could therefore be a way to have access to these networks and WPs could serve as anchors for superficial structural connectivity inference. Figure 70 show an example of a local network generated using the inter-crossing fiber regions proposed in this study.

Besides, such local networks have been suggested as an explanation for the shift of functional localization, or cortical plasticity, that takes place from the original locus to its peripheral loci with the progression of brain tumors or the progressive stages of ischemic expansion. For instance, Kristo et al. (2015); Saito et al. (2016); Magill et al. (2017) sometimes encounter patients with brain tumors whose function is relatively normal even though the brain tumor is invading a functional brain locus, such as a motor or language area. Also, recent studies using fMRI or intra-operative direct electrical stimulation revealed that the brain function of patients with tumor can shift to another place from an original position (Jang et al., 2002; Kawashima et al., 2013; Hayashi et al., 2014). Other resting-state fMRI studies found that functional connectivity could change according to functional recovery by increasing connections to neighboring gyri via U-shaped fibers or strengthening connections

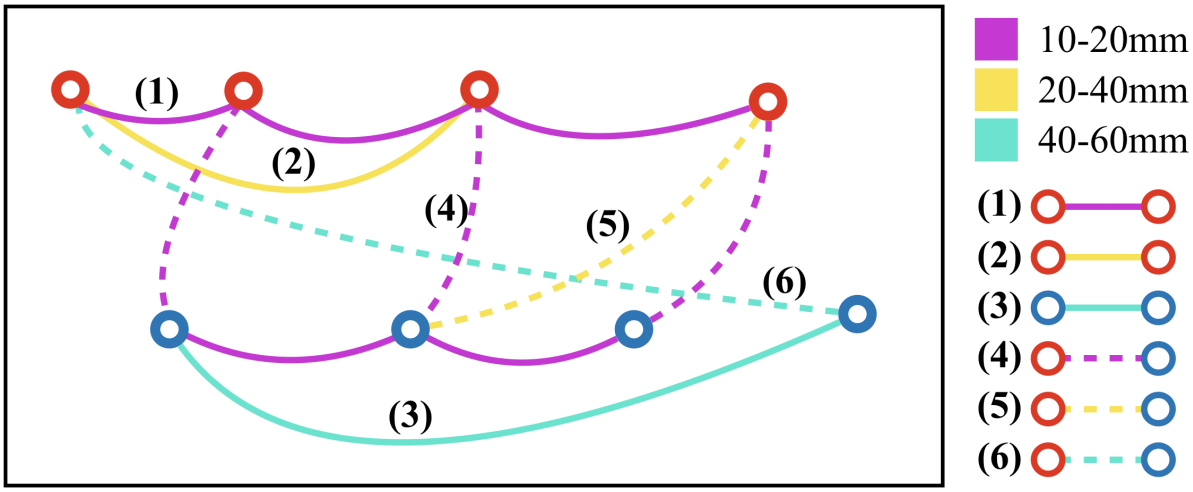


Figure 69: A summary sketch of extracted short-range U-fibers in STS. These fibers form a local structural connectivity network. The red and blue hollow circles represent the intersection of the PPs with the gyri on each side. (1) intra-gyral U-fibers with length $\in (10, 20]mm$, they connect the closest two regions in the same side; (2) intra-gyral U-fibers with length $\in (20, 40]mm$, they connect two regions in the same side; (3) intra-gyral U-fibers with length $\in (40, 60]mm$, they span over several location of PPs; (4) inter-gyral U-fibers with length $\in (10, 20]mm$, the PPs pathways; (5) inter-gyral U-fibers with length $\in (20, 40]mm$; (6) inter-gyral U-fibers with length $\in (40, 60]mm$.

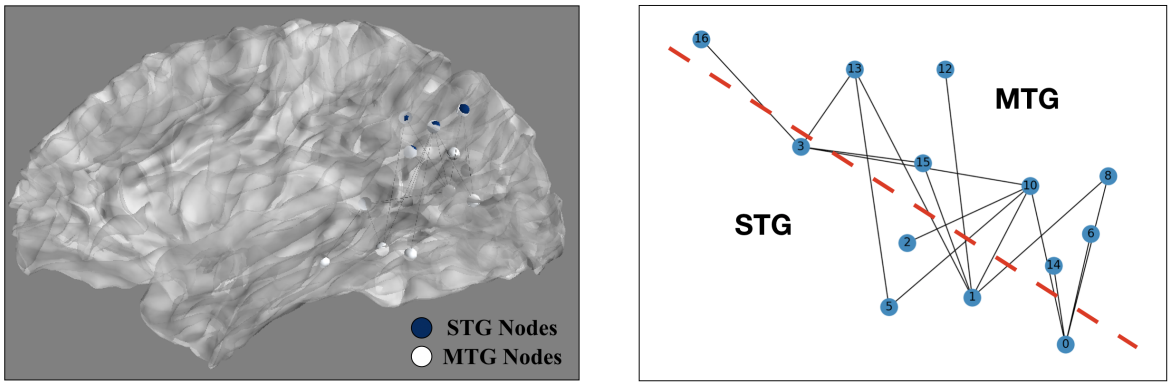


(a) (b)

Figure 70: An example of local connectivity networks. Here we only show a bipartite network, which corresponds to the connection of intral-gyral fibers. (a) the network in 3D brain. This figure was generated using *Mayavi*(https://docs.enthought.com/mayavi/mayavi/). (b) the bipartite graph of the network.

to the contralateral cerebral-hemisphere (Vassal et al., 2017; Bramati et al., 2019).

## 4.7 Conclusion

In this chapter, we first studied the PPs from the point view of connectivity, particularly the short-range U-fibers. Instead of learning using only the inter-gyral fibers as in (Bodin et al., 2021; Pron et al., 2021), we tried learning from both intra-gyral and inter-gyral U-fibers as proposed in (Shinohara et al., 2020).

To meet this requirement, we proposed a new map to visualise the distribution of various U-fibers terminations on the cortical surface. and we segmented this new map into several regions containing different types of U-fibers, and analysed them separately. Based on that, we showed a correlation between regions with crossing fibers and WPs. Therefore, we hypothesize that the PPs are located in the regions where intercrossing U-fibers terminate.

Then, we tried to use the connectivity maps to detect PPs, and an EnsSVM model using density maps of crossing fibers was trained. Although it showed a certain prediction accuracy on deep PPs, the connectivity heterogeneity in the STS made it difficult to distinguish between superficial PPs and non-PPs. In order to avoid the issues in connectivity maps, we proposed to use myelin maps, which have shown correlations with various biological features (Glasser et al., 2014). An EnsSVM using the myelin maps was trained, but unfortunately the results went from one extreme to the other, namely the MYL models perform well on the superficial PPs while unable to distinguish between deep PPs and non-PPs. A limitation of our work is that we applied the same pipeline to train machine learning models with different types of features. Even though the pipeline was successful in predicting PPs using morphology, it did not perform for connectivity and myelin. Clearly, more work needs to be done to exploit both connectivity and myelin maps and further work should attempt to use them in conjunction with morphological feature maps such as ASD.

# General conclusion

In this thesis, we were interested in the "annectant gyri" or "plis de passages" (PPs), which have been regarded as a specific landmark to partly explain the variability of cortical foldings across individuals. The PPs describe transverse gyri that interconnect both sides of a sulcus, are frequently buried in the depth of these sulci, and are sometimes apparent on the cortical surface. Based on this definition, the PPs are classified into two categories, namely the "Superficial PPs" and the "Deep PPs". For the superficial PPs, they always appeared with a clear variation of sulcal depth so that some automated algorithms or pipelines were implemented (Cykowski et al., 2008; Le Guen et al., 2018) but limited to depth based definitions. Also, a strict thresholds of depth is necessary in these method, which led to the difficulty to distinguish the PPs and small fluctuations of fundus, especially the very deep PPs in Ochiai et al. (2004). For the deep PPs, inspired by the description of interlocking gyri (Cunningham, 1890a,b, 1897), a new three-dimensional characteristic, named "wall piniches" (WPs), was proposed by Bodin et al. (2021). This local geometrical clue laid the foundation for the automatic detection of deep PPs.

### Selection of feature maps and machine learning methods

Since the PPs were characterized by two corresponding WPs on the adjacent gyri walls, several criteria were used in Bodin et al. (2021) to facilitate the identification of the WPs in the manual labelling. For a good visualization of the distortion of the cortical sheet, the DPF and curvature were selected. However, the drawbacks of these two maps themselves prevent them to be applied to the automatic detection. For the curvature map, one of the most convoluted area of the cortical surface is the gyri crests, which led to higher curvature values in gyri crests regions compared to the WPs. Thus, most small WPs on the gyri wall cannot be identified as their show too small variations of curvature values in their neighborhood. For the DPF, although it combines depth and curvature information, the DPF used in our study is still mostly representing variations of depth. Since depth represents geodesic distances from sulcal bottom to the gyral crown, it means the main direction of variation of the DPF is orthogonal to the WPs. To overcome this, we implemented the cortical surface profiling method (Li et al., 2010) and generated two feature maps *AverSampleDis* (ASD) and *SulciOrGyri* (SOG). Both the results of experiments and visualisation showed the superiority of new maps in PPs identification compared to the DPF and curvature map.

Besides morphological maps, we tested connectivity maps and myelin maps on our models, but none is better than the ASD maps. For the connectivity map of U-fibers terminations, connectivity heterogeneity in the STS led to the worse prediction results for the

PPs in the anterior part of STS. For the myelin map, it indeed got good results on the superficial PPs. A limitation of our work is that we applied the same pipeline to train machine learning models with different types of features. As the correlation between these two maps and PPs does exist from both observation and quantitative statistical analyses, more study should focus on how to use them. Moreover, a multi-modal machine learning-based detection process can be a further way to ensemble the clues related to PPs mentioned in the literature.

**Use and acquisition of data**

Back to the supervised classification problem of PPs in our study, we divided the data into two categories, namely PPs and non-PPs, according to whether the points on the STS fundus are intersected with manual labelled PPs lines or not. In fact, there are various ways to classify PPs (Ochiai et al., 2004; Bodin et al., 2021). We finally considered the detection of PPs as a binary classification problem for the following reasons: First, the dataset is an imbalanced dataset with a ratio of PPs to non-PPs around $1 : 16$. This typically imbalanced property, with PP as the minority class, leads to difficulties to directly use many machine learning methods. Second, according to the morphological description of the WPs in (Bodin et al., 2021), the WPs can be observed clearly for superficial PPs but also exist for the deepest buried PPs, which means the morphological clues are similar for two types of PPs.

For example, if we divided the PPs into superficial and deep PPs, the problem is converted to a 3-classification problem (superficial PPs, deep PPs and non-PPs). We note that the ratio of superficial PPs to deep PPs in the manually labelled PPs is approximately $2 : 7$, which means the imbalanced ratio among these three categories is much higher than that of the binary problem. Intuitively, this would have an impact on the prediction of both superficial and deep PPs. However, how it affects the model's classification of PPs, especially superficial PPs with ratio of $1 : 72$, still need to be experimented. Taking a different perspective on this 3-classification problem, although the WPs are present both in superficial and deep PPs, there is a slight difference in their local feature images (vectors), i.e. whether the WPs are linked or not. Based on this view, we remove the superficial PPs (with depth less than $10mm$) from the data since they can be easily detected by the variation of sulcal depth, and trained the same pipeline using ASD maps, we truly found an improvement of prediction results on the deep PPs with depth in $10 - 15mm$ ($89.6\% > 80.4\%$) and $15 - 20mm$ ($81.5\% > 79.4\%$). More work has to be done to investigate a better usage of the data.

In addition, how to get more data of PPs is important for the improvement of prediction results. A quick way would be to apply our method to more data, such as the TVA dataset, in order to generate PPs that can be further refined but the biggest challenge is the manual delineation of the STS fundus. Another possible way is to apply our method to other brain regions and sulci. However, the variability between brain regions, such as a general difference in sulcal depth, may affect the prediction results. Of course, other machine learning methods, such as semi-supervised learning, can be a future attempt.

**View of PPs: from morphology to connectivity**

As we introduced in the second chapters, the morphology or geometry of the PPs has been widely studied (e.g. (Cunningham, 1890a; Ochiai et al., 2004; Zlatkina and Petrides, 2010; Bodin et al., 2021)). Bodin et al. (2021) proposed that the PPs are short-range U-fiber connectivity pathways, and found a high density of U-fibers underlying PPs in the STS. By following this work, we designed several experiments to further investigate the relationships between short-range U-fibers and PPs. Different from (Bodin et al., 2021), we studied both intra-gyral and inter-gyral U-fibers in (Shinohara et al., 2020) and proposed a new density map as a visualization tool of various U-fibers terminations. Our results show that PPs are located the regions where intercrossing U-fibers terminate, which is consistent with the fibers dissection results in (Shinohara et al., 2020). Different from the description of PPs as short-range U-fiber connectivity pathways in (Bodin et al., 2021), our results reveal more general patterns of U-fibers passing through the white matter under the STS and terminating in the WPs where they enter the grey matter. Because of the high density of U-fibers termination, the WPs are extruded from the gyral wall. Moreover, we find that the distribution of U-fiber in very superficial PPs is not entirely following the pathways of inter-gyral U-fibers. Most U-fibers have one end point terminating in the bridging gyrus of the superficial PPs and the other end at the adjacent gyrus. It would be interesting to investigate the different patterns of underlying U-fibers distributions between the superficial and deep PPs. Does this differences explain their morphological differences?

Besides, some literature shows similar results in the association between specific gyral patterns and high density of fibers, such as the 3-hinge gyri (Li et al., 2010; Zhang et al., 2020a,b) and the 3-way junctions (Shinohara et al., 2020). From morphological observations of the PPs, we suggest they are actually referring to similar structures with different nomenclatures. At the end of our study, we proposed a local connectivity network based on U-fibers underlying the PPs in STS according to the hypothesis in (Shinohara et al., 2020). As a prototype, more work is still needed to propose a valid model. Since literature

and our work both demonstrated that PPs are located in regions of high-density U-fibers, which means the location of PPs are related to a specific structural connectivity, whether this structural connectivity can be used to explain functional connectivity is an interesting topic. Furthermore, many literatures have shown that superficial PPs in the STS are more developed in the left hemisphere, hinting at a link with the language system (Ochiai et al., 2004; Glasel et al., 2011; Segal and Petrides, 2012; Leroy et al., 2015; Le Guen et al., 2018). A recent result, however, has shown that a superficial PPs in the visual word form area has a positive impact on reading skills (Cachia et al., 2018). Could the U-fibers underlying the bridging gyrus of superficial PPs bring a clue to this functional area? Now that we can get more PPs using our machine learning models, much work can be done in the future.

# Reference


Altman Naomi S. An introduction to kernel and nearest-neighbor nonparametric regression. *The American Statistician*, 46(3):175–185, 1992.

Amunts Katrin, Schlaug Gottfried, Schleicher Axel, Steinmetz Helmuth, Dabringhaus Andreas, Roland Per E, and Zilles Karl. Asymmetry in the human motor cortex and handedness. *Neuroimage*, 4(3):216–222, 1996.

Amunts Katrin, Jäncke Lutz, Mohlberg Hartmut, Steinmetz Helmuth, and Zilles Karl. Interhemispheric asymmetry of the human motor cortex related to handedness and gender. *Neuropsychologia*, 38(3):304–312, 2000.

Assaf Yaniv, Johansen-Berg Heidi, and Thiebaut de Schotten Michel. The role of diffusion mri in neuroscience. *NMR in Biomedicine*, 32(4):e3762, 2019.

Auzias Guillaume, Lefevre Julien, Le Troter Arnaud, Fischer Clara, Perrot Matthieu, Régis Jean, and Coulon Olivier. Model-driven harmonic parameterization of the cortical surface: Hip-hop. *IEEE transactions on medical imaging*, 32(5):873–887, 2013.

Auzias Guillaume, Brun Lucile, Deruelle Christine, and Coulon Olivier. Deep sulcal landmarks: algorithmic and conceptual improvements in the definition and extraction of sulcal pits. *Neuroimage*, 111:12–25, 2015.

Avila Nicole Labra, Lebenberg Jessica, Rivière Denis, Auzias Guillaume, Fischer Clara, Poupon Fabrice, Guevara Pamela, Poupon Cyril, and Mangin Jean-François. Inference of an extended short fiber bundle atlas using sulcus-based constraints for a diffeomorphic inter-subject alignment. In *International Conference on Medical Image Computing and Computer-Assisted Intervention*, pages 323–333. Springer, 2019.

Basser Peter J, Pajevic Sinisa, Pierpaoli Carlo, Duda Jeffrey, and Aldroubi Akram. In vivo fiber tractography using dt-mri data. *Magnetic resonance in medicine*, 44(4):625–632, 2000.

Batista Gustavo EAPA, Prati Ronaldo C, and Monard Maria Carolina. A study of the behavior of several methods for balancing machine learning training data. *ACM SIGKDD explorations newsletter*, 6(1):20–29, 2004.

Bloch Felix. Nuclear induction. *Physical review*, 70(7-8):460, 1946.

Bodin Clémentine, Takerkart Sylvain, Belin Pascal, and Coulon Olivier. Anatomo-functional correspondence in the superior temporal sulcus. *Brain Structure and Function*, 223(1): 221–232, 2018.

Bodin Clémentine, Pron Alexandre, Le Mao Marion, Régis Jean, Belin P, and Coulon Olivier. Plis de passage in the superior temporal sulcus: Morphology and local connectivity. *Neuroimage*, 225:117513, 2021.

Boling Warren, Olivier André, Bittar Richard G, and Reutens David. Localization of hand motor activation in broca's pli de passage moyen. *Journal of neurosurgery*, 91(6):903–910, 1999.

Boling Warren W and Olivier André. Localization of hand sensory function to the pli de passage moyen of broca. *Journal of neurosurgery*, 101(2):278–283, 2004.

Borrell Víctor and Reillo Isabel. Emerging roles of neural stem cells in cerebral cortex development and evolution. *Developmental neurobiology*, 72(7):955–971, 2012.

Boucher Maxime, Whitesides Sue, and Evans Alan. Depth potential function for folding pattern representation, registration and analysis. *Medical image analysis*, 13(2):203–214, 2009.

Bramati Ivanei E, Rodrigues Erika C, Simões Elington L, Melo Bruno, Höfle Sebastian, Moll Jorge, Lent Roberto, and Tovar-Moll Fernanda. Lower limb amputees undergo long-distance plasticity in sensorimotor functional connectivity. *Scientific reports*, 9(1):1–10, 2019.

Breiman Leo. Bagging predictors. *Machine learning*, 24(2):123–140, 1996.

Breiman Leo. Random forests. *Machine learning*, 45(1):5–32, 2001.

Broca P. Description elémentaires des circonvolutions cérébrales de l'homme. *Mémoires d'anthropologie. Reinwald, Paris*, 707:804, 1888.

Cachia Arnaud, Mangin J-F, Riviere Denis, Kherif Ferath, Boddaert Nathalie, Andrade Alexandre, Papadopoulos-Orfanos Dimitri, Poline J-B, Bloch Isabelle, Zilbovicius Monica, et al. A primal sketch of the cortex mean curvature: a morphogenesis based approach to study the variability of the folding patterns. *IEEE transactions on medical imaging*, 22(6):754–765, 2003.

Cachia Arnaud, Roell Margot, Mangin Jean-François, Sun Zhong Yi, Jobert Antoinette, Braga Lucia, Houde Olivier, Dehaene Stanislas, and Borst Grégoire. How interindividual differences in brain anatomy shape reading accuracy. *Brain Structure and Function*, 223 (2):701–712, 2018.

Catani Marco. A little man of some importance. *Brain*, 140(11):3055–3061, 2017.

Catani Marco, Howard Robert J, Pajevic Sinisa, and Jones Derek K. Virtual in vivo interactive dissection of white matter fasciculi in the human brain. *Neuroimage*, 17(1):77–94, 2002.

Catani Marco, Dell'Acqua Flavio, Vergani Francesco, Malik Farah, Hodge Harry, Roy Prasun, Valabregue Romain, and De Schotten Michel Thiebaut. Short frontal lobe connections of the human brain. *cortex*, 48(2):273–291, 2012.

Cawley Gavin C and Talbot Nicola LC. On over-fitting in model selection and subsequent selection bias in performance evaluation. *The Journal of Machine Learning Research*, 11: 2079–2107, 2010.

Chan Philip K and Stolfo Salvatore J. Learning with non-uniform class and cost distributions: Effects and a distributed multi-classifier approach. In *In Workshop Notes KDD-98 Workshop on Distributed Data Mining*. Citeseer, 1998.

Chang Chih-Chung and Lin Chih-Jen. Libsvm: a library for support vector machines. *ACM transactions on intelligent systems and technology (TIST)*, 2(3):1–27, 2011.

Chawla Nitesh V. C4. 5 and imbalanced data sets: investigating the effect of sampling method, probabilistic estimate, and decision tree structure. In *Proceedings of the ICML*, volume 3, page 66, 2003.

Chawla Nitesh V. Data mining for imbalanced datasets: An overview. *Data mining and knowledge discovery handbook*, pages 875–886, 2009.

Chawla Nitesh V, Bowyer Kevin W, Hall Lawrence O, and Kegelmeyer W Philip. Smote: synthetic minority over-sampling technique. *Journal of artificial intelligence research*, 16: 321–357, 2002.

Chawla Nitesh V, Lazarevic Aleksandar, Hall Lawrence O, and Bowyer Kevin W. Smoteboost: Improving prediction of the minority class in boosting. In *European conference on principles of data mining and knowledge discovery*, pages 107–119. Springer, 2003.

Chawla Nitesh V, Japkowicz Nathalie, and Kotcz Aleksander. Special issue on learning from imbalanced data sets. *ACM SIGKDD explorations newsletter*, 6(1):1–6, 2004.

Chen Chao, Liaw Andy, Breiman Leo, et al. Using random forest to learn imbalanced data. *University of California, Berkeley*, 110(1-12):24, 2004.

Chen Hanbo, Li Yujie, Ge Fangfei, Li Gang, Shen Dinggang, and Liu Tianming. Gyral net: A new representation of cortical folding organization. *Medical image analysis*, 42:14–25, 2017.

Chen Weimin, Ma Chaoqun, and Ma Lin. Mining the customer credit using hybrid support vector machine technique. *Expert systems with applications*, 36(4):7611–7616, 2009.

Clouchoux Cédric, Rivière Denis, Mangin J-F, Operto Grégory, Régis Jean, and Coulon Olivier. Model-driven parameterization of the cortical surface for localization and inter-subject matching. *Neuroimage*, 50(2):552–566, 2010.

Conturo Thomas E, Lori Nicolas F, Cull Thomas S, Akbudak Erbil, Snyder Abraham Z, Shimony Joshua S, McKinstry Robert C, Burton Harold, and Raichle Marcus E. Tracking neuronal fiber pathways in the living human brain. *Proceedings of the National Academy of Sciences*, 96(18):10422–10427, 1999.

Cortes Corinna and Vapnik Vladimir. Support-vector networks. *Machine learning*, 20(3): 273–297, 1995.

Coulon O, Clouchoux C, Operato G, Dauchot K, Sirigu A, and Anton JL. Cortical localization via surface parameterization: a sulcus-based approach. *Neuroimage*, 31(Suppl 1): 29–185, 2006.

Coulon Olivier, Pizzagalli Fabrizio, Operto Grégory, Auzias Guillaume, Delon-Martin Chantal, and Dojat Michel. Two new stable anatomical landmarks on the central sulcus: definition, automatic detection, and their relationship with primary motor functions of the hand. In *2011 Annual International Conference of the IEEE Engineering in Medicine and Biology Society*, pages 7795–7798. IEEE, 2011.

Coupé Pierrick, Manjón José V, Fonov Vladimir, Pruessner Jens, Robles Montserrat, and Collins D Louis. Patch-based segmentation using expert priors: Application to hippocampus and ventricle segmentation. *NeuroImage*, 54(2):940–954, 2011.

Cox Simon R, Ritchie Stuart J, Tucker-Drob Elliot M, Liewald David C, Hagenaars Saskia P, Davies Gail, Wardlaw Joanna M, Gale Catharine R, Bastin Mark E, and Deary Ian J.

Ageing and brain white matter structure in 3,513 uk biobank participants. *Nature communications*, 7(1):1–13, 2016.

Cunningham Daniel John. The complete fissures of the human cerebrum, and their significance in connection with the growth of the hemisphere and the appearance of the occipital lobe. *Journal of anatomy and physiology*, 24(Pt 3):309, 1890a.

Cunningham Daniel John. The fissure of rolando. *Journal of anatomy and physiology*, 25 (Pt 1):1, 1890b.

Cunningham Daniel John. *Contribution to the surface anatomy of the cerebral hemispheres*. Number 7. Academy House, 1892.

Cunningham Daniel John. The rolandic and calcarine fissures—a study of the growing cortex of the cerebrum. *Journal of anatomy and physiology*, 31(Pt 4):586, 1897.

Cykowski Matthew D, Coulon Olivier, Kochunov Peter V, Amunts Katrin, Lancaster Jack L, Laird Angela R, Glahn David C, and Fox Peter T. The central sulcus: an observer-independent characterization of sulcal landmarks and depth asymmetry. *Cerebral cortex*, 18(9):1999–2009, 2008.

Daducci Alessandro, Dal Palu Alessandro, Lemkaddem Alia, and Thiran Jean-Philippe. A convex optimization framework for global tractography. In *2013 IEEE 10th International Symposium on Biomedical Imaging*, pages 524–527. IEEE, 2013.

Daducci Alessandro, Dal Palù Alessandro, Lemkaddem Alia, and Thiran Jean-Philippe. Commit: Convex optimization modeling for microstructure informed tractography. *IEEE transactions on medical imaging*, 34(1):246–257, 2014.

Davatzikos Christos and Bryan R Nick. Morphometric analysis of cortical sulci using parametric ribbons: a study of the central sulcus. *Journal of computer assisted tomography*, 26(2):298–307, 2002.

De Schotten Michel Thiebaut, Bizzi Alberto, Dell'Acqua Flavio, Allin Matthew, Walshe Muriel, Murray Robin, Williams Steven C, Murphy Declan GM, Catani Marco, et al. Atlasing location, asymmetry and inter-subject variability of white matter tracts in the human brain with mr diffusion tractography. *Neuroimage*, 54(1):49–59, 2011.

Dejerine Jules, Dejerine Jules, and Dejerine Augusta. *Anatomie des centres nerveux*, volume 1. Rueff, 1895.

Drummond Chris, Holte Robert C, et al. C4. 5, class imbalance, and cost sensitivity: why under-sampling beats over-sampling. In *Workshop on learning from imbalanced datasets II*, volume 11, pages 1–8. Citeseer, 2003.

Dubois Jessica, Dehaene-Lambertz Ghislaine, Kulikova Sofya, Poupon Cyril, Hüppi Petra S, and Hertz-Pannier Lucie. The early development of brain white matter: a review of imaging studies in fetuses, newborns and infants. *Neuroscience*, 276:48–71, 2014.

Dumais Susan, Platt John, Heckerman David, and Sahami Mehran. Inductive learning algorithms and representations for text categorization. In *Proceedings of the seventh international conference on Information and knowledge management*, pages 148–155, 1998.

Efron Bradley and Tibshirani Robert J. *An introduction to the bootstrap*. CRC press, 1994.

Ertekin Seyda, Huang Jian, Bottou Leon, and Giles Lee. Learning on the border: active learning in imbalanced data classification. In *Proceedings of the sixteenth ACM conference on Conference on information and knowledge management*, pages 127–136, 2007.

Everitt Brian S, Landau Sabine, Leese Morven, and Stahl Daniel. Miscellaneous clustering methods. *Cluster analysis*, pages 215–255, 2011.

Fan Rong-En, Chang Kai-Wei, Hsieh Cho-Jui, Wang Xiang-Rui, and Lin Chih-Jen. Liblinear: A library for large linear classification. *the Journal of machine Learning research*, 9: 1871–1874, 2008.

Fawcett Tom and Provost Foster. Adaptive fraud detection. *Data mining and knowledge discovery*, 1(3):291–316, 1997.

Fischl Bruce and Dale Anders M. Measuring the thickness of the human cerebral cortex from magnetic resonance images. *Proceedings of the National Academy of Sciences*, 97 (20):11050–11055, 2000.

Fix Evelyn and Hodges Joseph Lawson. Discriminatory analysis. nonparametric discrimination: Consistency properties. *International Statistical Review/Revue Internationale de Statistique*, 57(3):238–247, 1989.

Forkel Stephanie J, Mahmood Sajedha, Vergani Francesco, and Catani Marco. The white matter of the human cerebrum: part i the occipital lobe by heinrich sachs. *Cortex*, 62: 182–202, 2015.

Garcia Kara, Wang Xiaojie, and Kroenke Christopher. A model of tension-induced fiber growth predicts white matter organization during brain folding. 2020.

Ge Fangfei, Li Xiao, Razavi Mir Jalil, Chen Hanbo, Zhang Tuo, Zhang Shu, Guo Lei, Hu Xiaoping, Wang Xianqiao, and Liu Tianming. Denser growing fiber connections induce 3-hinge gyral folding. *Cerebral Cortex*, 28(3):1064–1075, 2018.

Geng Guangqiang, Johnston Leigh A, Yan Edwin, Britto Joanne M, Smith David W, Walker David W, and Egan Gary F. Biomechanisms for modelling cerebral cortical folding. *Medical image analysis*, 13(6):920–930, 2009.

Germann Jürgen, Robbins Steve, Halsband Ulrike, and Petrides Michael. Precentral sulcal complex of the human brain: morphology and statistical probability maps. *Journal of Comparative Neurology*, 493(3):334–356, 2005.

Geurts Pierre, Ernst Damien, and Wehenkel Louis. Extremely randomized trees. *Machine learning*, 63(1):3–42, 2006.

Girard Gabriel, Whittingstall Kevin, Deriche Rachid, and Descoteaux Maxime. Towards quantitative connectivity analysis: reducing tractography biases. *Neuroimage*, 98:266–278, 2014.

Glasel H, Leroy François, Dubois Jessica, Hertz-Pannier Lucie, Mangin Jean-François, and Dehaene-Lambertz Ghislaine. A robust cerebral asymmetry in the infant brain: the rightward superior temporal sulcus. *Neuroimage*, 58(3):716–723, 2011.

Glasser Matthew F and Van Essen David C. Mapping human cortical areas in vivo based on myelin content as revealed by t1-and t2-weighted mri. *Journal of Neuroscience*, 31 (32):11597–11616, 2011.

Glasser Matthew F, Sotiropoulos Stamatios N, Wilson J Anthony, Coalson Timothy S, Fischl Bruce, Andersson Jesper L, Xu Junqian, Jbabdi Saad, Webster Matthew, Polimeni Jonathan R, et al. The minimal preprocessing pipelines for the human connectome project. *Neuroimage*, 80:105–124, 2013.

Glasser Matthew F, Goyal Manu S, Preuss Todd M, Raichle Marcus E, and Van Essen David C. Trends and properties of human cerebral cortex: correlations with cortical myelin content. *Neuroimage*, 93:165–175, 2014.

Gratiolet Louis Pierre. *Mémoire sur les Plis cérébraux de l'Homme et des Primatès: Mit Einem Atlas (4 pp. XIV pl.) in fol. 33i.* A. Bertrand, 1854.

Grebenkov Denis S. Partially reflected brownian motion: a stochastic approach to transport phenomena. *Focus on probability theory*, pages 135–169, 2006.

Griffa Alessandra, Baumann Philipp S, Thiran Jean-Philippe, and Hagmann Patric. Structural connectomics in brain diseases. *Neuroimage*, 80:515–526, 2013.

Guevara Miguel, Román Claudio, Houenou Josselin, Duclap Delphine, Poupon Cyril, Mangin Jean François, and Guevara Pamela. Reproducibility of superficial white matter tracts using diffusion-weighted imaging tractography. *Neuroimage*, 147:703–725, 2017.

Guo Hongyu and Viktor Herna L. Learning from imbalanced data sets with boosting and data generation: the databoost-im approach. *ACM Sigkdd Explorations Newsletter*, 6(1): 30–39, 2004.

Hau Janice, Aljawad Saba, Baggett Nicole, Fishman Inna, Carper Ruth A, and Müller Ralph-Axel. The cingulum and cingulate u-fibers in children and adolescents with autism spectrum disorders. *Human brain mapping*, 40(11):3153–3164, 2019.

Hayashi Yutaka, Nakada Mitsutoshi, Kinoshita Masashi, and Hamada Jun-ichiro. Functional reorganization in the patient with progressing glioma of the pure primary motor cortex: a case report with special reference to the topographic central sulcus defined by somatosensory-evoked potential. *World neurosurgery*, 82(3-4):536–e1, 2014.

Heath Florence, Hurley Samuel A, Johansen-Berg Heidi, and Sampaio-Baptista Cassandra. Advances in noninvasive myelin imaging. *Developmental Neurobiology*, 78(2):136–151, 2018.

Hopkins William D, Coulon Olivier, and Mangin J-F. Observer-independent characterization of sulcal landmarks and depth asymmetry in the central sulcus of the chimpanzee brain. *Neuroscience*, 171(2):544–551, 2010.

Hopkins William D, Meguerditchian Adrien, Coulon Olivier, Bogart Stephanie, Mangin Jean-François, Sherwood Chet C, Grabowski Mark W, Bennett Allyson J, Pierre Peter J, Fears Scott, et al. Evolution of the central sulcus morphology in primates. *Brain, behavior and evolution*, 84(1):19–30, 2014.

Huntgeburth Sonja C and Petrides Michael. Morphological patterns of the collateral sulcus in the human brain. *European Journal of Neuroscience*, 35(8):1295–1311, 2012.

Im Kiho and Grant P Ellen. Sulcal pits and patterns in developing human brains. *Neuroimage*, 185:881–890, 2019.

Im Kiho, Jo Hang Joon, Mangin Jean-François, Evans Alan C, Kim Sun I, and Lee Jong-Min. Spatial distribution of deep sulcal landmarks and hemispherical asymmetry on the cortical surface. *Cerebral cortex*, 20(3):602–611, 2010.

Im Kiho, Lee Jong-Min, Jeon Seun, Kim Jong-Heon, Seo Sang Won, Na Duk L, and Grant P Ellen. Reliable identification of deep sulcal pits: the effects of scan session, scanner, and surface extraction tool. *PLoS One*, 8(1):e53678, 2013.

Jaccard Paul. The distribution of the flora in the alpine zone. 1. *New phytologist*, 11(2): 37–50, 1912.

Jakob C. Nueva contribución á la fisiopatología de los lóbulos frontales. *La Semana Médica*, 13(50):1325–1329, 1906.

Jang Sung Ho, Han Bong Soo, Chang Yongmin, Byun Woo Mok, Lee Jun, and Ahn Sang Ho. Functional mri evidence for motor cortex reorganization adjacent to a lesion in a primary motor cortex. *American journal of physical medicine & rehabilitation*, 81(11):844–847, 2002.

Japkowicz Nathalie. The class imbalance problem: Significance and strategies. In *Proc. of the Int'l Conf. on Artificial Intelligence*, volume 56. Citeseer, 2000.

Jbabdi Saad and Johansen-Berg Heidi. Tractography: where do we go from here? *Brain connectivity*, 1(3):169–183, 2011.

Jenkinson Mark, Beckmann Christian F, Behrens Timothy EJ, Woolrich Mark W, and Smith Stephen M. Fsl. *Neuroimage*, 62(2):782–790, 2012.

Jeurissen Ben, Tournier Jacques-Donald, Dhollander Thijs, Connelly Alan, and Sijbers Jan. Multi-tissue constrained spherical deconvolution for improved analysis of multi-shell diffusion mri data. *NeuroImage*, 103:411–426, 2014.

Jo Taeho and Japkowicz Nathalie. Class imbalances versus small disjuncts. *ACM Sigkdd Explorations Newsletter*, 6(1):40–49, 2004.

Johansen-Berg Heidi and Behrens Timothy EJ. *Diffusion MRI: from quantitative measurement to in vivo neuroanatomy*. Academic Press, 2013.

Jones Derek K and Cercignani Mara. Twenty-five pitfalls in the analysis of diffusion mri data. *NMR in Biomedicine*, 23(7):803–820, 2010.

Jones Derek K, Knösche Thomas R, and Turner Robert. White matter integrity, fiber count, and other fallacies: the do's and don'ts of diffusion mri. *Neuroimage*, 73:239–254, 2013.

Kawashima Akitsugu, Krieg Sandro M, Faust Katharina, Schneider Heike, Vajkoczy Peter, and Picht Thomas. Plastic reshaping of cortical language areas evaluated by navigated transcranial magnetic stimulation in a surgical case of glioblastoma multiforme. 2013.

Kirilina Evgeniya, Helbling Saskia, Morawski Markus, Pine Kerrin, Reimann Katja, Jankuhn Steffen, Dinse Juliane, Deistung Andreas, Reichenbach Jürgen R, Trampel Robert, et al. Superficial white matter imaging: Contrast mechanisms and whole-brain in vivo mapping. *Science advances*, 6(41):eaaz9281, 2020.

Kristo Gert, Raemaekers Mathijs, Rutten Geert-Jan, de Gelder Beatrice, and Ramsey Nick F. Inter-hemispheric language functional reorganization in low-grade glioma patients after tumour surgery. *Cortex*, 64:235–248, 2015.

Kubat Miroslav, Matwin Stan, et al. Addressing the curse of imbalanced training sets: one-sided selection. In *Icml*, volume 97, pages 179–186. Citeseer, 1997.

Kubat Miroslav, Holte Robert C, and Matwin Stan. Machine learning for the detection of oil spills in satellite radar images. *Machine learning*, 30(2):195–215, 1998.

Lauterbur Paul C. Image formation by induced local interactions: examples employing nuclear magnetic resonance. *nature*, 242(5394):190–191, 1973.

Le Bihan Denis and Breton E. Imagerie de diffusion in vivo par résonance magnétique nucléaire. *Comptes rendus de l'Académie des sciences. Série 2, Mécanique, Physique, Chimie, Sciences de l'univers, Sciences de la Terre*, 301(15):1109–1112, 1985.

Le Guen Yann, Leroy François, Auzias Guillaume, Riviere Denis, Grigis Antoine, Mangin Jean-François, Coulon Olivier, Dehaene-Lambertz Ghislaine, and Frouin Vincent. The chaotic morphology of the left superior temporal sulcus is genetically constrained. *Neuroimage*, 174:297–307, 2018.

Le Troter Arnaud, Riviere D, and Coulon O. An interactive sulcal fundi editor in brainvisa. In *17th International Conference on Human Brain Mapping, Organization for Human Brain Mapping*, 2011.

Lebel Catherine, Treit Sarah, and Beaulieu Christian. A review of diffusion mri of typical white matter development from early childhood to young adulthood. *NMR in Biomedicine*, 32(4):e3778, 2019.

Lefèvre Julien and Mangin Jean-François. A reaction-diffusion model of human brain development. *PLoS computational biology*, 6(4):e1000749, 2010.

Lemaître Guillaume, Nogueira Fernando, and Aridas Christos K. Imbalanced-learn: A python toolbox to tackle the curse of imbalanced datasets in machine learning. *Journal of Machine Learning Research*, 18(17):1–5, 2017. URL http://jmlr.org/papers/v18/16-365.html.

Leroy François, Cai Qing, Bogart Stephanie L, Dubois Jessica, Coulon Olivier, Monzalvo Karla, Fischer Clara, Glasel Hervé, Van der Haegen Lise, Bénézit Audrey, et al. New human-specific brain landmark: the depth asymmetry of superior temporal sulcus. *Proceedings of the National Academy of Sciences*, 112(4):1208–1213, 2015.

Li Kaiming, Guo Lei, Li Gang, Nie Jingxin, Faraco Carlos, Cui Guangbin, Zhao Qun, Miller L Stephen, and Liu Tianming. Gyral folding pattern analysis via surface profiling. *NeuroImage*, 52(4):1202–1214, 2010.

Liao T Warren. Classification of weld flaws with imbalanced class data. *Expert Systems with Applications*, 35(3):1041–1052, 2008.

Ling Charles X and Li Chenghui. Data mining for direct marketing: Problems and solutions. In *Kdd*, volume 98, pages 73–79, 1998.

Liu Tian-Yu. Easyensemble and feature selection for imbalance data sets. In *2009 international joint conference on bioinformatics, systems biology and intelligent computing*, pages 517–520. IEEE, 2009.

Liu Yang, Yu Xiaohui, Huang Jimmy Xiangji, and An Aijun. Combining integrated sampling with svm ensembles for learning from imbalanced datasets. *Information Processing & Management*, 47(4):617–631, 2011.

Llinares-Benadero Cristina and Borrell Víctor. Deconstructing cortical folding: genetic, cellular and mechanical determinants. *Nature Reviews Neuroscience*, 20(3):161–176, 2019.

Lohmann Gabriele, Von Cramon D Yves, and Steinmetz Helmuth. Sulcal variability of twins. *Cerebral Cortex*, 9(7):754–763, 1999.

Lohmann Gabriele, Von Cramon D Yves, and Colchester Alan CF. Deep sulcal landmarks provide an organizing framework for human cortical folding. *Cerebral Cortex*, 18(6):1415–1420, 2008.

Love Seth. Demyelinating diseases. *Journal of clinical pathology*, 59(11):1151–1159, 2006.

Magill Stephen T, Han Seunggu J, Li Jing, and Berger Mitchel S. Resection of primary motor cortex tumors: feasibility and surgical outcomes. *Journal of neurosurgery*, 129(4): 961–972, 2017.

Mai Jürgen K, Majtanik Milan, and Paxinos George. *Atlas of the human brain*. Academic Press, 2015.

Malandain Grégoire, Bertrand Gilles, and Ayache Nicholas. Topological segmentation of discrete surfaces. *International journal of computer vision*, 10(2):183–197, 1993.

Maloof Marcus A. Learning when data sets are imbalanced and when costs are unequal and unknown. In *ICML-2003 workshop on learning from imbalanced data sets II*, volume 2, pages 2–1, 2003.

Mangin J-F, Riviere Denis, Cachia Arnaud, Duchesnay Edouard, Cointepas Yann, Papadopoulos-Orfanos Dimitri, Collins D Louis, Evans Alan C, and Régis Jean. Object-based morphometry of the cerebral cortex. *IEEE transactions on medical imaging*, 23(8): 968–982, 2004a.

Mangin J-F, Riviere Denis, Cachia Arnaud, Duchesnay Edouard, Cointepas Yves, Papadopoulos-Orfanos Dimitri, Scifo Paola, Ochiai T, Brunelle Francis, and Régis Jean. A framework to study the cortical folding patterns. *Neuroimage*, 23:S129–S138, 2004b.

Mangin Jean-François, Frouin Vincent, Bloch Isabelle, Régis Jean, and López-Krahe Jaime. From 3d magnetic resonance images to structural representations of the cortex topography using topology preserving deformations. *Journal of Mathematical imaging and Vision*, 5 (4):297–318, 1995.

Mangin Jean-François, Auzias Guillaume, Coulon Olivier, Sun Zhong Yi, Rivière Denis, and Régis Jean. Sulci as landmarks. *Brain mapping: an encyclopedic reference*, 2(2015): 45–52, 2015.

Mangin Jean-François, Le Guen Yann, Labra Nicole, Grigis Antoine, Frouin Vincent, Guevara Miguel, Fischer Clara, Rivière Denis, Hopkins William D, Régis Jean, et al. "plis de passage" deserve a role in models of the cortical folding process. *Brain topography*, 32(6): 1035–1048, 2019.

Mangin JF, Régis J, Poupon C, Pachot-Clouart M, Belin P, Bihan DL, and Frouin V. The duality between sulcal roots and u-fiber bundles investigated via tensor diffusion imaging. *NeuroImage*, 7:P–0700, 1998.

Mansfield Peter and Grannell Peter K. Nmr'diffraction'in solids? *Journal of Physics C: solid state physics*, 6(22):L422, 1973.

Maratea Antonio, Petrosino Alfredo, and Manzo Mario. Adjusted f-measure and kernel scaling for imbalanced data learning. *Information Sciences*, 257:331–341, 2014.

Matthews Paul M and Jezzard Peter. Functional magnetic resonance imaging. *Journal of Neurology, Neurosurgery & Psychiatry*, 75(1):6–12, 2004.

McKay D Reese, Kochunov Peter, Cykowski Matthew D, Kent Jack W, Laird Angela R, Lancaster Jack L, Blangero John, Glahn David C, and Fox Peter T. Sulcal depth-position profile is a genetically mediated neuroscientific trait: description and characterization in the central sulcus. *Journal of Neuroscience*, 33(39):15618–15625, 2013.

Meng Yu, Li Gang, Lin Weili, Gilmore John H, and Shen Dinggang. Spatial distribution and longitudinal development of deep cortical sulcal landmarks in infants. *Neuroimage*, 100:206–218, 2014.

Merboldt Klaus-Dietmar, Hanicke Wolfgang, and Frahm Jens. Self-diffusion nmr imaging using stimulated echoes. *Journal of Magnetic Resonance (1969)*, 64(3):479–486, 1985.

Meynert Theodor. *Psychiatry; a clinical treatise on diseases of the fore-brain based upon a study of its structure, functions, and nutrition*. GP Putnam's Sons, 1885.

Moran Paul R. A flow velocity zeugmatographic interlace for nmr imaging in humans. *Magnetic resonance imaging*, 1(4):197–203, 1982.

Mosconi Lisa, Brys Miroslaw, Glodzik-Sobanska Lidia, De Santi Susan, Rusinek Henry, and De Leon Mony J. Early detection of alzheimer's disease using neuroimaging. *Experimental gerontology*, 42(1-2):129–138, 2007.

Novikov Dmitry S, Fieremans Els, Jespersen Sune N, and Kiselev Valerij G. Quantifying brain microstructure with diffusion mri: Theory and parameter estimation. *NMR in Biomedicine*, 32(4):e3998, 2019.

Ochiai Taku, Grimault Stephan, Scavarda Didier, Roch Giorgi, Hori Tomokatsu, Rivière Denis, Mangin Jean François, and Régis Jean. Sulcal pattern and morphology of the superior temporal sulcus. *Neuroimage*, 22(2):706–719, 2004.

Oishi Kenichi, Zilles Karl, Amunts Katrin, Faria Andreia, Jiang Hangyi, Li Xin, Akhter Kazi, Hua Kegang, Woods Roger, Toga Arthur W, et al. Human brain white matter atlas: identification and assignment of common anatomical structures in superficial white matter. *Neuroimage*, 43(3):447–457, 2008.

Ono Michio, Kubik Stefan, and Abernathey Chad D. *Atlas of the cerebral sulci*. Thieme Medical Publishers, 1990.

Opitz David and Maclin Richard. Popular ensemble methods: An empirical study. *Journal of artificial intelligence research*, 11:169–198, 1999.

O'Halloran Rafael, Feldman Rebecca, Marcuse Lara, Fields Madeline, Delman Bradley, Frangou Sophia, and Balchandani Priti. A method for u-fiber quantification from 7t diffusion-weighted mri data tested in subjects with non-lesional focal epilepsy. *Neuroreport*, 28(8):457, 2017.

Panagiotaki Eleftheria, Schneider Torben, Siow Bernard, Hall Matt G, Lythgoe Mark F, and Alexander Daniel C. Compartment models of the diffusion mr signal in brain white matter: a taxonomy and comparison. *Neuroimage*, 59(3):2241–2254, 2012.

Pedregosa F., Varoquaux G., Gramfort A., Michel V., Thirion B., Grisel O., Blondel M., Prettenhofer P., Weiss R., Dubourg V., Vanderplas J., Passos A., Cournapeau D., Brucher M., Perrot M., and Duchesnay E. Scikit-learn: Machine learning in Python. *Journal of Machine Learning Research*, 12:2825–2830, 2011.

Perrot Matthieu, Rivière Denis, and Mangin Jean-François. Cortical sulci recognition and spatial normalization. *Medical image analysis*, 15(4):529–550, 2011.

Phua Clifton, Alahakoon Damminda, and Lee Vincent. Minority report in fraud detection: classification of skewed data. *Acm sigkdd explorations newsletter*, 6(1):50–59, 2004.

Polikar Robi. Ensemble learning. In *Ensemble machine learning*, pages 1–34. Springer, 2012.

Posse Stefan, Cuenod Charles A, and Le Bihan D. Human brain: proton diffusion mr spectroscopy. *Radiology*, 188(3):719–725, 1993.

Pron Alexandre, Deruelle Christine, and Coulon Olivier. U-shape short-range extrinsic connectivity organisation around the human central sulcus. *Brain Structure and Function*, 226(1):179–193, 2021.

Purcell Edward M, Torrey Henry Cutler, and Pound Robert V. Resonance absorption by nuclear magnetic moments in a solid. *Physical review*, 69(1-2):37, 1946.

Rakic Pasko. Specification of cerebral cortical areas. *Science*, 241(4862):170–176, 1988.

Rakic Pasko. A small step for the cell, a giant leap for mankind: a hypothesis of neocortical expansion during evolution. *Trends in neurosciences*, 18(9):383–388, 1995.

Régis J, Mangin J-Fr, Frouin V, Sastre F, Peragut JC, and Samson Y. Generic model for the localization of the cerebral cortex and preoperative multimodal integration in epilepsy surgery. *Stereotactic and Functional Neurosurgery*, 65(1-4):72–80, 1995.

Regis Jean. Deep sulcal anatomy and functional mapping of the cerebral cortex (in french), 1994.

Regis Jean, Mangin Jean-François, Ochiai Taku, Frouin Vincent, Rivière Denis, Cachia Arnaud, Tamura Manabu, and Samson Yves. "sulcal root" generic model: a hypothesis to overcome the variability of the human cortex folding patterns. *Neurologia medico-chirurgica*, 45(1):1–17, 2005.

Rettmann Maryam E, Han Xiao, Xu Chenyang, and Prince Jerry L. Automated sulcal segmentation using watersheds on the cortical surface. *NeuroImage*, 15(2):329–344, 2002.

Reveley Colin, Seth Anil K, Pierpaoli Carlo, Silva Afonso C, Yu David, Saunders Richard C, Leopold David A, and Frank Q Ye. Superficial white matter fiber systems impede detection of long-range cortical connections in diffusion mr tractography. *Proceedings of the National Academy of Sciences*, 112(21):E2820–E2828, 2015.

Riley KJ, O'Neill DP, and Kralik SF. Subcortical u-fibers: signposts to the diagnosis of white matter disease. *Neurographics*, 8(4):234–243, 2018.

Ritchie Stuart J, Cox Simon R, Shen Xueyi, Lombardo Michael V, Reus Lianne M, Alloza Clara, Harris Mathew A, Alderson Helen L, Hunter Stuart, Neilson Emma, et al. Sex differences in the adult human brain: evidence from 5216 uk biobank participants. *Cerebral cortex*, 28(8):2959–2975, 2018.

Rokach Lior. Ensemble-based classifiers. *Artificial intelligence review*, 33(1):1–39, 2010.

Rokach Lior and Maimon Oded Z. *Data mining with decision trees: theory and applications*, volume 69. World scientific, 2007.

Román Claudio, Guevara Miguel, Valenzuela Ronald, Figueroa Miguel, Houenou Josselin, Duclap Delphine, Poupon Cyril, Mangin Jean-François, and Guevara Pamela. Clustering of whole-brain white matter short association bundles using hardi data. *Frontiers in neuroinformatics*, 11:73, 2017.

Rosett Joshua. *Intercortical systems of the human cerebrum*. Columbia University Press, 1933.

Rousseau Françcois, Habas Piotr A, and Studholme Colin. A supervised patch-based approach for human brain labeling. *IEEE transactions on medical imaging*, 30(10):1852–1862, 2011.

Sachs H. Das hemisphärenmark des menschlichen grosshirns. *Dmw-Deutsche Medizinische Wochenschrift*, 19(27):651–652, 1893.

Sadek Rowayda A. An improved mri segmentation for atrophy assessment. *International Journal of Computer Science Issues (IJCSI)*, 9(3):569, 2012.

Saito Taiichi, Muragaki Yoshihiro, Maruyama Takashi, Tamura Manabu, Nitta Masayuki, Tsuzuki Shunsuke, Konishi Yoshiyuki, Kamata Kotoe, Kinno Ryuta, Sakai Kuniyoshi L, et al. Difficulty in identification of the frontal language area in patients with dominant frontal gliomas that involve the pars triangularis. *Journal of neurosurgery*, 125(4):803–811, 2016.

Saygin Zeynep M, Osher David E, Koldewyn Kami, Reynolds Gretchen, Gabrieli John DE, and Saxe Rebecca R. Anatomical connectivity patterns predict face selectivity in the fusiform gyrus. *Nature neuroscience*, 15(2):321–327, 2012.

Schmahmann Jeremy D, Schmahmann Jeremy, and Pandya Deepak. *Fiber pathways of the brain*. OUP USA, 2009.

Schubert Erich, Sander Jörg, Ester Martin, Kriegel Hans Peter, and Xu Xiaowei. Dbscan revisited, revisited: why and how you should (still) use dbscan. *ACM Transactions on Database Systems (TODS)*, 42(3):1–21, 2017.

Schüz Almut and Braitenberg Valentino. The human cortical white matter: quantitative aspects of cortico-cortical long-range connectivity. In *Cortical Areas*, pages 389–398. CRC Press, 2002.

Segal Emily and Petrides Michael. The morphology and variability of the caudal rami of the superior temporal sulcus. *European Journal of Neuroscience*, 36(1):2035–2053, 2012.

Shah Abhidha, Goel Aimee, Jhawar Sukhdeep Singh, Patil Abhinandan, Rangnekar Ranjit, and Goel Atul. Neural circuitry: architecture and function—a fiber dissection study. *World neurosurgery*, 125:e620–e638, 2019.

Shattuck David W, Joshi Anand A, Pantazis Dimitrios, Kan Eric, Dutton Rebecca A, Sowell Elizabeth R, Thompson Paul M, Toga Arthur W, and Leahy Richard M. Semi-automated method for delineation of landmarks on models of the cerebral cortex. *Journal of neuroscience methods*, 178(2):385–392, 2009.

Shinohara Harumichi, Liu Xiaoliang, Nakajima Riho, Kinoshita Masashi, Ozaki Noriyuki, Hori Osamu, and Nakada Mitsutoshi. Pyramid-shape crossings and intercrossing fibers are key elements for construction of the neural network in the superficial white matter of the human cerebrum. *Cerebral Cortex*, 30(10):5218–5228, 2020.

Smith RE, Tournier JD, Calamante F, and Connelly A. Structurallyinformed tractography: improved diffusion mri streamlines tractography using anatomical information. In *International Symposium on, Magnetic Resonance in Medicine (ISMRM'12)*, page 1907, 2012a.

Smith Robert E, Tournier Jacques-Donald, Calamante Fernando, and Connelly Alan. Anatomically-constrained tractography: improved diffusion mri streamlines tractography through effective use of anatomical information. *Neuroimage*, 62(3):1924–1938, 2012b.

Solberg AH Schistad and Solberg Rune. A large-scale evaluation of features for automatic detection of oil spills in ers sar images. In *IGARSS'96. 1996 International Geoscience and Remote Sensing Symposium*, volume 3, pages 1484–1486. IEEE, 1996.

Song Tianqi, Bodin Clémentine, and Coulon Olivier. Automatic detection of plis de passage in the superior temporal sulcus using surface profiling and ensemble svm. In *2021 IEEE 18th International Symposium on Biomedical Imaging (ISBI)*, pages 850–853. IEEE, 2021.

Sporns Olaf. Brain connectivity. *Scholarpedia*, 2(10):4695, 2007.

Sporns Olaf, Tononi Giulio, and Kötter Rolf. The human connectome: a structural description of the human brain. *PLoS computational biology*, 1(4):e42, 2005.

Sprung-Much Trisanna and Petrides Michael. Morphological patterns and spatial probability maps of two defining sulci of the posterior ventrolateral frontal cortex of the human brain: the sulcus diagonalis and the anterior ascending ramus of the lateral fissure. *Brain Structure and Function*, 223(9):4125–4152, 2018.

St-Onge Etienne, Daducci Alessandro, Girard Gabriel, and Descoteaux Maxime. Surface-enhanced tractography (set). *NeuroImage*, 169:524–539, 2018.

Stamatatos Efstathios. Author identification: Using text sampling to handle the class imbalance problem. *Information Processing & Management*, 44(2):790–799, 2008.

Steele Christopher J and Zatorre Robert J. Practice makes plasticity. *Nature neuroscience*, 21(12):1645–1646, 2018.

Sun Aixin, Lim Ee-Peng, and Liu Ying. On strategies for imbalanced text classification using svm: A comparative study. *Decision Support Systems*, 48(1):191–201, 2009.

Swets John A. Measuring the accuracy of diagnostic systems. *Science*, 240(4857):1285–1293, 1988.

Symms M, Jäger HR, Schmierer K, and Yousry TA. A review of structural magnetic resonance neuroimaging. *Journal of Neurology, Neurosurgery & Psychiatry*, 75(9):1235–1244, 2004.

Takahashi Emi, Folkerth Rebecca D, Galaburda Albert M, and Grant Patricia E. Emerging cerebral connectivity in the human fetal brain: an mr tractography study. *Cerebral cortex*, 22(2):455–464, 2012.

Tao Xiaodong, Prince Jerry L, and Davatzikos Christos. Using a statistical shape model to extract sulcal curves on the outer cortex of the human brain. *IEEE Transactions on Medical Imaging*, 21(5):513–524, 2002.

Taylor DG and Bushell MC. The spatial mapping of translational diffusion coefficients by the nmr imaging technique. *Physics in medicine & biology*, 30(4):345, 1985.

Theodoridou Zoe D and Triarhou Lazaros C. Challenging the supremacy of the frontal lobe: Early views (1906–1909) of christfried jakob on the human cerebral cortex. *Cortex*, 48(1): 15–25, 2012.

Thompson Abigail, Murphy Declan, Dell'Acqua Flavio, Ecker Christine, McAlonan Grainne, Howells Henrietta, Baron-Cohen Simon, Lai Meng-Chuan, Lombardo Michael V, Catani Marco, et al. Impaired communication between the motor and somatosensory homunculus is associated with poor manual dexterity in autism spectrum disorder. *Biological psychiatry*, 81(3):211–219, 2017.

Toro Roberto and Burnod Yves. A morphogenetic model for the development of cortical convolutions. *Cerebral cortex*, 15(12):1900–1913, 2005.

Toro Roberto, Perron Michel, Pike Bruce, Richer Louis, Veillette Suzanne, Pausova Zdenka, and Paus Tomáš. Brain size and folding of the human cerebral cortex. *Cerebral cortex*, 18(10):2352–2357, 2008.

Tournier J Donald, Calamante Fernando, Connelly Alan, et al. Improved probabilistic streamlines tractography by 2nd order integration over fibre orientation distributions. In *Proceedings of the international society for magnetic resonance in medicine*, volume 1670. John Wiley & Sons, Inc. New Jersey, USA, 2010.

Tournier J-Donald, Smith Robert, Raffelt David, Tabbara Rami, Dhollander Thijs, Pietsch Maximilian, Christiaens Daan, Jeurissen Ben, Yeh Chun-Hung, and Connelly Alan. Mrtrix3: A fast, flexible and open software framework for medical image processing and visualisation. *Neuroimage*, 202:116137, 2019.

Tustison Nicholas J, Avants Brian B, Cook Philip A, Zheng Yuanjie, Egan Alexander, Yushkevich Paul A, and Gee James C. N4itk: improved n3 bias correction. *IEEE transactions on medical imaging*, 29(6):1310–1320, 2010.

Uddin Lucina Q. Complex relationships between structural and functional brain connectivity. *Trends in cognitive sciences*, 17(12):600–602, 2013.

van der Walt Stéfan, Schönberger Johannes L., Nunez-Iglesias Juan, Boulogne François, Warner Joshua D., Yager Neil, Gouillart Emmanuelle, Yu Tony, and the scikit-image contributors. scikit-image: image processing in Python. *PeerJ*, 2:e453, 6 2014. ISSN 2167-8359. doi: 10.7717/peerj.453. URL https://doi.org/10.7717/peerj.453.

van der Weijden Chris WJ, García David Vállez, Borra Ronald JH, Thurner Patrick, Meilof Jan F, van Laar Peter-Jan, Dierckx Rudi AJO, Gutmann Ingomar W, and de Vries Erik FJ. Myelin quantification with mri: A systematic review of accuracy and reproducibility. *NeuroImage*, page 117561, 2020.

Van Essen David C. A tension-based theory of morphogenesis and compact wiring in the central nervous system. *Nature*, 385(6614):313–318, 1997.

Van Essen David C. A 2020 view of tension-based cortical morphogenesis. *Proceedings of the National Academy of Sciences*, 117(52):32868–32879, 2020.

Vassal Matthieu, Charroud Céline, Deverdun Jérémy, Le Bars Emmanuelle, Molino François, Bonnetblanc Francois, Boyer Anthony, Dutta Anirban, Herbet Guillaume, Moritz-Gasser Sylvie, et al. Recovery of functional connectivity of the sensorimotor network

after surgery for diffuse low-grade gliomas involving the supplementary motor area. *Journal of neurosurgery*, 126(4):1181–1190, 2017.

Velly Lionel, Perlbarg Vincent, Boulier Thomas, Adam Nicolas, Delphine Sebastien, Luyt Charles-Edouard, Battisti Valentine, Torkomian Gregory, Arbelot Charlotte, Chabanne Russell, et al. Use of brain diffusion tensor imaging for the prediction of long-term neurological outcomes in patients after cardiac arrest: a multicentre, international, prospective, observational, cohort study. *The Lancet Neurology*, 17(4):317–326, 2018.

Vlaardingerbroek Marinus T and Boer Jacques A. *Magnetic resonance imaging: theory and practice*. Springer Science & Business Media, 2013.

Wang Zhou, Bovik Alan C, Sheikh Hamid R, Simoncelli Eero P, et al. Image quality assessment: from error visibility to structural similarity. *IEEE transactions on image processing*, 13(4):600–612, 2004.

Waterston David. Complete bilateral interruption of the fissure of rolando. *Journal of anatomy and physiology*, 41(Pt 2):143, 1907.

Welker Wally. Why does cerebral cortex fissure and fold? In *Cerebral cortex*, pages 3–136. Springer, 1990.

Wendelken Carter, Ferrer Emilio, Ghetti Simona, Bailey Stephen K, Cutting Laurie, and Bunge Silvia A. Frontoparietal structural connectivity in childhood predicts development of functional connectivity and reasoning ability: A large-scale longitudinal investigation. *Journal of Neuroscience*, 37(35):8549–8558, 2017.

Wilson D Randall and Martinez Tony R. Reduction techniques for instance-based learning algorithms. *Machine learning*, 38(3):257–286, 2000.

Yeh Fang-Cheng, Panesar Sandip, Fernandes David, Meola Antonio, Yoshino Masanori, Fernandez-Miranda Juan C, Vettel Jean M, and Verstynen Timothy. Population-averaged atlas of the macroscale human structural connectome and its network topology. *Neuroimage*, 178:57–68, 2018.

Yousry Tarek A, Schmid UD, Alkadhi Hatem, Schmidt D, Peraud Aurelia, Buettner Andreas, and Winkler P. Localization of the motor hand area to a knob on the precentral gyrus. a new landmark. *Brain: a journal of neurology*, 120(1):141–157, 1997.

Yu Peng, Grant P Ellen, Qi Yuan, Han Xiao, Ségonne Florent, Pienaar Rudolph, Busa Evelina, Pacheco Jenni, Makris Nikos, Buckner Randy L, et al. Cortical surface

shape analysis based on spherical wavelets. *IEEE transactions on medical imaging*, 26(4): 582–597, 2007.

Zhang Fan, Wu Ye, Norton Isaiah, Rigolo Laura, Rathi Yogesh, Makris Nikos, and O'Donnell Lauren J. An anatomically curated fiber clustering white matter atlas for consistent white matter tract parcellation across the lifespan. *NeuroImage*, 179:429–447, 2018.

Zhang Tuo, Chen Hanbo, Guo Lei, Li Kaiming, Li Longchuan, Zhang Shu, Shen Dinggang, Hu Xiaoping, and Liu Tianming. Characterization of u-shape streamline fibers: methods and applications. *Medical image analysis*, 18(5):795–807, 2014.

Zhang Tuo, Huang Ying, Zhao Lin, He Zhibin, Jiang Xi, Guo Lei, Hu Xiaoping, and Liu Tianming. Identifying cross-individual correspondences of 3-hinge gyri. *Medical image analysis*, 63:101700, 2020a.

Zhang Tuo, Li Xiao, Jiang Xi, Ge Fangfei, Zhang Shu, Zhao Lin, Liu Huan, Huang Ying, Wang Xianqiao, Yang Jian, et al. Cortical 3-hinges could serve as hubs in cortico-cortical connective network. *Brain imaging and behavior*, pages 1–18, 2020b.

Zhou Zhi-Hua. *Ensemble methods: foundations and algorithms*. Chapman and Hall/CRC, 2019.

Zilles Karl, Armstrong Este, Schleicher Axel, and Kretschmann Hans-Joachim. The human pattern of gyrification in the cerebral cortex. *Anatomy and embryology*, 179(2):173–179, 1988.

Zlatkina Veronika and Petrides Michael. Morphological patterns of the postcentral sulcus in the human brain. *Journal of Comparative Neurology*, 518(18):3701–3724, 2010.

Zlatkina Veronika, Amiez Céline, and Petrides Michael. The postcentral sulcal complex and the transverse postcentral sulcus and their relation to sensorimotor functional organization. *European Journal of Neuroscience*, 43(10):1268–1283, 2016.